
STRONG-FIELD-INDUCED BREAKUP OF DIATOMIC MOLECULES

LUN YUE
PHD DISSERTATION
JANUARY 2016



AARHUS
UNIVERSITY

DEPARTMENT OF PHYSICS AND ASTRONOMY

ENGLISH SUMMARY

The rapid development of laser technology has made it possible to produce very intense laser pulses with laser frequencies ranging from the terahertz to the X-ray regimes. When a diatomic molecule is irradiated by such intense laser pulses, it can break apart in a number of different ways: it can ionize into an ion plus one or more free electrons; it can dissociate without ionization into two fragments; or it can ionize while undergoing dissociation, separating into three or more fragments. The characterization and understanding of such strong-field processes is of fundamental interest. The current dissertation is concerned with the theoretical investigation of these breakup processes for a diatomic molecule in different laser-pulse regimes. This is achieved by solving the time-dependent Schrödinger equation for the simplest molecule, the molecular hydrogen ion, which can be considered a benchmark molecular system. A method for efficient numerical extraction of continuum observables is proposed. New physical processes are discovered both in the infrared and the extreme-ultraviolet regimes, and qualitative and analytical models are proposed that explains these observations. In addition, the multi-electron effects in molecular-orientation-dependent tunneling ionization are investigated for some multi-electron molecular systems. These effects are explained by combining a multi-electron method with an accurate analytical tunneling theory.

DANSK RESUMÉ

Den hurtige udvikling af laserteknologi har gjort det muligt at fremstille meget intense laserpulser med laserfrekvenser lige fra terahertz til X-ray regimer. Når et diatomart molekyle bestråles med sådanne intense laserpulser, kan det fragmentere på en række forskellige måder: det kan ionisere til en ion samt en eller flere frie elektroner; det kan dissociere uden ionisation til to fragmenter; eller det kan ionisere samtidig med at det dissocierer, hvilket kan resultere i tre eller flere fragmenter. Beskrivelsen og forståelsen af sådanne stærkfeltsprocesser er interessant ud fra et grundlæggende forståelsesmæssigt synspunkt. Denne afhandling handler om den teoretiske undersøgelse af disse løsrivelsesprocesser for et diatomart molekyle i forskellige laserpulsregimer. Dette opnås ved at løse den tidsafhængige Schrödingerligning for det mest simple molekyle, den molekulære brint-ion, som ofte kan betragtes som en standard sammenligningsmodel for molekulære systemer. Der foreslås nye numerisk effektive metoder til at udregne kvantemekaniske kontinuumsobservabler. Nye fysiske fænomener opdages fra disse udregninger både i det infrarøde og ekstrem-ultraviolette frekvensområder, og kvalitative og analytiske modeller er udviklet der kan forklare observationerne. Desuden er multielektronseffekter i molekulært orienteringafhængige tunneleringsionisation undersøgt for forskellige multielektronmolekyler. Disse resultater er opnået ved at kombinere en multielektronmetode med en nøjagtig analytisk tunneleringssteori.

CONTENTS

Preface	vi
Notation	vi
Acknowledgements	vi
List of abbreviations	vii
List of publications	ix
1 Introduction	1
1.1 Outline of the thesis	6
2 Diatomic molecules in intense laser fields	8
2.1 Time-dependent Schrödinger equation for diatomics	8
2.2 Pure dissociation dynamics: The surface model	14
2.3 Dissociation and dissociative ionization: 1D H_2^+	15
2.4 Electron-electron correlations: The TD-GASCI scheme	16
3 Numerical solutions of the TDSE	23
3.1 Generic numerical concepts	23
3.2 Numerical solution of the surface model	29
3.3 Numerical solution of 1D H_2^+	30
3.4 Numerical solution of the TD-GASCI method	30
4 Extraction of spectra from the TDSE	34
4.1 Differential spectra for 1D H_2^+	35
4.2 Continuum observables in many-electron systems	47
5 Molecular dynamic interference in the intense XUV regime	56
5.1 Numerical results	56
5.2 Analysis of the JES	60
5.3 Conclusion	67

6	Molecular breakup in the very intense XUV regime	69
6.1	TDSE results	69
6.2	High-frequency Floquet theory	71
6.3	Physical model based on HFFT	75
6.4	Control of the wave packet	77
6.5	Probing the dissociative WP	79
6.6	On the generality of the model	80
6.7	Conclusion	81
7	Inter- and intracycle interference effects in dissociative ionization	82
7.1	Motivation	82
7.2	TDSE results	83
7.3	Strong-field approximation	84
7.4	Time-resolved JES	90
7.5	CEP effects	91
7.6	Nuclear motion effects	92
7.7	Conclusion	94
8	Molecular Tunneling ionization with electron-electron correlation	95
8.1	Tunneling ionization overview	95
8.2	The weak-field asymptotic theory	97
8.3	Dyson orbital in TD-GASCI	103
8.4	Structure factor	106
8.5	Conclusion	115
9	Summary and outlook	118
A	Gaussian quadratures and the finite-element discrete variable representation	121
A.1	Gaussian quadrature	121
A.2	Discrete variable representation	123
A.3	Finite-element discrete variable representation	125
B	Field-free continuum eigenstates	126
C	Dressed BO curve of a diatomic molecule for small α_0	128
C.1	Neglect of the term involving P_2	131
D	Coordinate transformations	135
D.1	Coordinate systems	135

D.2 Coordinate transformations 136

References **139**

PREFACE

This dissertation contains a summary of some of the work I have done during my PhD studies at the Department of Physics and Astronomy, Aarhus University, Denmark, under the supervision of Lars Bojer Madsen.

Notation

Atomic units (a.u.) are used in this thesis, unless stated otherwise. In atomic units, the electron mass m , the elementary charge e , the reduced Planck's constant \hbar , and the Bohr radius a_0 , are equal to unity.

Acknowledgements

I would like to thank my PhD supervisor Lars Bojer Madsen for the opportunity to pursue my PhD in his group at Aarhus University. I am grateful for all his excellent guidance, support and enthusiasm during the four years, and the fact that he can always manage to squeeze the necessary time from his busy schedule for discussions. I thank Haruhide Miyagi for his help on the numerical aspects of my project in the beginning of my PhD when I knew nothing. I thank Sebastian Bauch for his help on the TD-GASCI code and our fruitful discussions on the WFAT project. I thank Jens Egebjerg Bækhøj for a cool collaboration on the ATAS project. I thank Chuan Yu, Jens Svensmark, and all group members for our discussions. I thank my office mates Christian K. Andersen and Andrew C. J. Wade for our fun and fruitless discussions where we always end up agreeing to disagree. A special thanks to Camille Lévêque for proofreading a big part of the thesis, and to Christian K. Andersen for proofreading the summaries. Lastly, I would like to thank my parents and my friends for all their support during my PhD.

List of abbreviations

ADK	Ammosov-Delone-Krainov
as	attosecond(s)
ATD	above-threshold dissociation
ATI	above-threshold ionization
a.u.	atomic unit(s)
BO	Born-Oppenheimer
CAP	complex absorbing potential
CEP	carrier-envelope phase
CI	configuration interaction
CIS	configuration interaction singles
COLTRIMS	cold-target recoil ion momentum spectroscopy
DI	dissociative ionization
DVR	discrete variable representation
FE-DVR	finite element DVR
FNA	fixed-nuclei approximation
fs	femtosecond(s)
FEL	free-electron laser
FWHM	full width at half maximum
HF	Hartree-Fock
HFFT	high-frequency Floquet theory
HHG	high-harmonic generation
HOMO	highest occupied molecular orbital
IP	ionization potential
ITP	imaginary time propagation
JES	joint-energy spectrum
KH	Kramers-Henneberger
LG	length gauge
MCTDHF	multi-configurational time-dependent Hartree-Fock
NIR	near-infrared
NKER	nuclear kinetic energy release
PAD	photoelectron angular distribution
PES	photoelectron energy spectrum
PMS	photoelectron momentum spectrum
ps	picosecond(s)

SAEA	single-active electron approximation
SFA	strong-field approximation
SIA	short-iterative Arnoldi
SIL	short-iterative Lanczos
SO-FFT	split-operator fast Fourier transform
SS	Siegert state
TD	time-dependent
TDSE	time-dependent Schrödinger equation
TD-RASCI	time-dependent restricted-active-space configuration-interaction
TD-GASCI	time-dependent generalized-active-space configuration-interaction
TEO	time evolution operator
TISE	time-independent Schrödinger equation
tSURFF	time-dependent surface flux
VG	velocity gauge
WFAT	weak-field asymptotic theory
WP	wave packet
XUV	extreme ultraviolet

LIST OF PUBLICATIONS

- [1] L. Yue and L. B. Madsen, *Dissociation and dissociative ionization of H_2^+ using the time-dependent surface flux method*. Phys. Rev. A, **88**, 063420 (2013).
- [2] L. Yue and L. B. Madsen, *Dissociative ionization of H_2^+ using intense femtosecond xuv laser pulses*. Phys. Rev. A, **90**, 063408 (2014).
- [3] J. E. Bækhøj, L. Yue, and L. B. Madsen, *Nuclear-motion effects in attosecond transient-absorption spectroscopy of molecules*. Phys. Rev. A, **91**, 043408 (2015).
- [4] L. Yue and L. B. Madsen, *Characterization of molecular breakup by very intense femtosecond xuv laser pulses*. Phys. Rev. Lett., **115**, 033001 (2015).
- [5] L. Yue and L. B. Madsen, *Interference effects in strong-field dissociative ionization*. arXiv:1512.01428 (2015).
- [6] L. Yue, S. Bauch, and L. B. Madsen, *Electron correlation effects in orientation-dependent tunneling ionization of molecules* (in preparation).

CHAPTER 1

INTRODUCTION

The foundation of our understanding of light-matter interactions has its roots in discoveries made at the turn of the twentieth century. The major experimental discoveries include the observation of the Balmer series in the spectral line emissions of hydrogen in 1885 by Johann Balmer, and the observation of the photoelectric effect in 1887 by Heinrich Hertz. These discoveries stimulated the introduction of the concept of light-quantas by Albert Einstein in 1905, known today as photons, and the introduction of the atomic quantum model by Niels Bohr in 1913, which laid the foundation of modern quantum mechanics. In 1917, Einstein predicted the process of stimulated emission of electromagnetic radiation, which in 1960 led to one of the most important inventions of the twentieth century: the laser.

Since the initial inception of the laser, a rapid development in laser technology has ensued, with the production of increasingly more intense and shorter laser pulses. Standard commercial table-top lasers can now produce pulses with intensities in the range $10^{13} - 10^{15}$ W/cm², pulse durations in the picosecond (1 ps = 10^{-12} s) to femtosecond (1 fs = 10^{-15} s) regimes, and a central wavelength around the near-infrared (NIR) 800 nm. These lasers are so intense that when irradiated on an atomic or molecular system, the force exerted on the charged constituents of the system is comparable or greater in strength than the binding forces of the system. In addition to adding new knowledge to our understanding of light-matter interactions, these technological advances have also opened up whole new areas of research. For example, since the vibrational motion of molecules occurs on the femtosecond time scale, the advent of femtosecond lasers has led to the birth of *femtochemistry*, where laser pulses are used to control and probe chemical reactions [7]. Typically, to obtain time-resolved information, pump-probe schemes have been used, where a pump pulse first induces dynamics in the system under investigation and a subsequent probe pulse is applied after a fixed time-delay to extract time information. The intense light sources have also

led to the area of research known as *strong-field physics*, where a system is so strongly driven by the intense laser pulse that highly nonlinear phenomena can occur. Famous strong-field nonlinear phenomena for atoms and molecules with NIR and visible lasers include

- **multiphoton ionization** [8], where several photons are absorbed during the laser pulse to reach the ionization threshold;
- **above-threshold ionization (ATI)** [9], where the system absorbs more photons than the minimum required number to ionize, with the corresponding photoelectron energy spectrum (PES) featuring peaks separated by the photon energy;
- **multiple ionization**, where more than one electron is ionized;
- **high-harmonic generation (HHG)** [10], where a gas-sample irradiated by an intense pulse generates photons with energies that are a high multiple of the incident photon energy;
- **intracycle interference**, [11, 12] where electronic wave packets (WPs) created during the same optical cycle interfere, leading to interference patterns in the photoelectron momentum spectrum (PMS) and PES. When a few-cycle NIR pulse is used, two released wave packets (of the same electron) are released separated by an attosecond time-interval, causing people to refer to the measurement as an “attosecond double-slit experiment”.

In molecules, the nuclear degrees of freedom can lead to molecular specific breakup processes. One distinguishes between (pure) dissociation, where molecules breaks apart without ionization, (pure) ionization, where ionization occurs without dissociation, and dissociative ionization (DI) where ionization and dissociation occur simultaneously. Coulomb explosion, where the positively charged nuclei strongly breaks apart following multiple ionization, is a special case of DI. Molecular-specific strong-field processes induced by NIR and visible lasers include

- **charge-resonance-enhanced ionization** [13, 14], where a molecule shows very high ionization rate at internuclear distances much greater than the equilibrium internuclear distance;
- **bond softening** [15, 16], where the molecular bond is weakened by the laser pulse and induces dissociation;
- **bond hardening** [15, 17], where a molecular bond is strengthened and prevents dissociation;

- **above-threshold dissociation (ATD)** [17, 18], where the molecule absorbs more photons than the minimum required number to dissociate;
- **above-threshold Coulomb explosion** [19], where the molecule absorbs more photons than the minimum required number to Coulomb explode;
- **electron-nuclei energy-sharing in DI** [20–22], where instead of the typical ATI peaks, the electron and nuclei share the photon energies between them.

In the last two decades, with the help of the HHG process, the generation of extreme-ultraviolet (XUV) pulses with attosecond ($1 \text{ as} = 10^{-18} \text{ s}$) duration has become a reality [23–25]. Since the electronic motion is on the attosecond time scale, the generation of attosecond pulses has opened up the new research area known as *attoscience* [26], with the ultimate goal of controlling and probing electrons on their natural time scale. Attosecond probing schemes include attosecond streaking spectroscopy [27–29], attosecond interferometry [30, 31], and attosecond transient absorption spectroscopy [32, 33].

Another important recent development in source technology is the production of intense few-cycle midinfrared laser pulses [34–36]. Due to the wavelength-squared scaling of the cutoff in a HHG spectrum, such intense, midinfrared pulses are able to produce ultrahigh harmonics, with a HHG spectrum that spans from the ultraviolet to the X-ray regime [34]. These pulses are of importance for the potential sub-attosecond pulse generation [37, 38], strong-field holography [39, 40] and laser-induced electron diffraction [36, 41].

Aside from table-top lasers, there has also been rapid developments in free-electron lasers (FELs). In a FEL, relativistic electron beams are accelerated and decelerated to convert kinetic energy into coherent radiation. FELs can generate radiation from the terahertz regime to the X-ray regime, with higher intensities than table-top lasers. For example, in the terahertz regime, intensities up to $2 \times 10^{22} \text{ W/cm}^2$ have been achieved [42], while for XUV the intensities greater than $4 \times 10^{17} \text{ W/cm}^2$ have been documented [43]. Such intense XUV pulses were applied on rare gases to study sequential versus non-sequential multiple ionization [44, 45], and creation of positive charge states up to 21 in xenon [46]. Many interesting atomic effects have been theoretically predicted in the very intense XUV regime, but eluded detection. These include:

- **dynamic interference effect** [47, 48], where ionized electronic WPs with equal continuum energies created during the rising and falling edges of the laser pulse interfere, given rise to interference structures in the PES;

- **atomic stabilization** [49, 50], where the ionization rate does not increase, or even decreases with increasing laser intensity. The effect requires the photon energy to be larger than the ionization potential, and experimental evidence for the effect has been spotted in Rydberg atoms.

It is of high interest to study similar effects in molecules.

In addition to pulse generation, new experimental detection techniques are now available like the cold-target recoil ion momentum spectroscopy (COLTRIMS) [51], where three-dimensional momentum distributions of multiple charged particles can be measured in coincidence.

The theory of strong-field physics has been evolved along with the experimental progress. Due to the strong laser-matter interactions, perturbative approaches often fails, prompting the development of other approaches to strong-field problems. The Keldysh parameter, first introduced by Leonid Keldysh in 1964 [52], reads

$$\gamma = \sqrt{\frac{I_p}{2U_p}} \quad (1.1)$$

with I_p the ionization potential of the considered system, and

$$U_p = \frac{I}{4\omega^2} \quad (1.2)$$

the ponderomotive potential corresponding to the cycle-averaged kinetic energy of a classical electron in a sinusoidal electric field oscillating at intensity I and angular frequency ω . The Keldysh parameter gives a rough estimate of the adiabaticity of the photo-ionization process, as it can be interpreted as the ratio between the characteristic time it takes for the electron to tunnel through the effective barrier formed by the electric field and the static Coulomb potential $t_{\text{tunnel}} \sim \sqrt{I_p/(2I)}$, and the characteristic time of the laser oscillation $t_{\text{laser}} \sim 1/(2\omega)$. In the regime of high-intensity and low-frequency fields, $\gamma \ll 1$, the electron would have sufficient time to tunnel through the barrier and the ionization is said to occur in the *quasi-static* regime. For fields with low intensity and high frequency, the field changes sign so quickly that the electron has no time to tunnel and ionization is said to be happening in the *multi-photon regime*. In the quasi-static regime, one distinguishes between *tunneling ionization* where the electron can tunnel through the effective barrier, and *over-the-barrier ionization* where the field-free binding energy is above the barrier. For atomic hydrogen, the over-the-barrier intensity is $I_B \equiv I_p^2/4 = 1.4 \times 10^{14} \text{ W/cm}^2$.

Many of the mentioned strong-field processes can be qualitatively understood by the semiclassical three-step model [53]. An electron is ionized (step one),

whereafter it moves in the presence of the strong laser field (step two). Depending on the moment of ionization, the electron can do the following (step three): reach the detector directly with a maximal energy of $2U_p$, resulting in ATI; elastically scatter of the ion and produce electrons with energies up to $10U_p$; inelastically scatter off the ion which can dislodge a second electron, leading to the process known as nonsequential double ionization; recombine with the ion, producing a high-energy photon with a maximal energy corresponding to the maximal return energy of the electron plus the ionization potential $3.14U_p + I_p$, explaining the process of HHG. The quantum version of the semiclassical model is the strong-field approximation (SFA) [52, 54, 55], where the ionization process is described as a transition from a field-free initial state to a final Volkov state, ignoring the Coulomb interaction of the ionized electron with the remaining ion. The description of HHG in the SFA framework is known as the Lewenstein model [56] where the recombination with the field-free initial state is included. In the low-frequency pulse regimes with $\gamma \ll 1$, static tunneling theories can be used to model the first ionization step. Many such theories exist, such as the Ammosov-Delone-Krainov (ADK) theory [57, 58], and the weak-field asymptotic theory (WFAT) [59, 60]. In the high-frequency regimes, to predict the stabilization phenomenon, a theory known as high-frequency Floquet theory (HFFT) [49] was proposed, which proceeds iteratively by successively approximating the time-dependent Schrödinger equation (TDSE) to higher orders in ω^{-1} .

In addition to qualitative models, direct simulation of the quantum dynamics by solving the TDSE can be performed. When all relevant degrees of freedom are included, such calculations can be regarded as numerical experiments. Indeed, many of the mentioned strong-field molecular processes were first predicted by numerical solutions of the TDSE, with experimental verifications following later. These processes include bond softening, bond hardening, ATD, and electron-nuclei energy sharing in DI. It is thus of crucial importance to accurately solve the TDSE. Due to the scaling of the computational effort with the number of degrees of freedom, accurate solutions to the TDSE involving an external field is nowadays only possible for the case of small systems such as the helium atom [61]. In addition, in contrast to quantum chemistry calculations where the desired observables are the bound state energies, strong-field simulations require a much larger simulation volume in order to correctly describe the continua for the ejected fragments. These numerical difficulties have led to the usage of different approximation schemes in solving the TDSE. Popular approximations include the single-active-electron approximation (SAEA) with a single electron coupled to the field, and the fixed-nuclei approximation (FNA) for molecules with the vibrations and rotations neglected. Often, the neglect of certain degrees of free-

dom gives a highly inaccurate description of the physics, and much effort has recently been put in the development of theories that can efficiently solve the multi-electron TDSE without making the SAEA. Such methods include the time-dependent Hartree Fock [62], TD density functional theory [63], TD configuration interaction singles [64], multi-configurational TD Hartree-Fock (MCTDHF) [65], TD restricted-active-space self-consistent-field theory [66], TD restricted-active-space configuration-interaction (TD-RASCI) [67] and TD generalized-active-space configuration-interaction (TD-GASCI) [68]. Some of these methods, such as the MCTDHF, can be generalized to treat diatomic molecules including nuclear motion [69].

In addition to the difficulties in solving the TDSE, efficient extraction of continuum observables such as the PES provides a great challenge. The most straightforward way to obtain the PES is to project the wave function on scattering states after the laser interaction. However, due to the large distance traversed by the electron during the laser, a huge simulation volume is required for the solution of the TDSE, making the calculation highly unfeasible. Another issue is the difficulty in obtaining scattering states. Different methods has been proposed to circumvent these difficulties. One can propagate the TDSE with the time-scaled coordinate method [70], where a scaled coordinate is introduced to treat the ionized WP, with no extra computational cost, or one can employ flux methods [71–73], where the spectra are calculated by monitoring the flux going through a surface during the time-propagation.

1.1 Outline of the thesis

This thesis deals with the theoretical investigation of strong-field-induced breakup processes in diatomic molecules. By solving the TDSE, the dissociation and DI of the molecular hydrogen ion is studied, with laser frequencies ranging from the infrared to the XUV regimes. Efficient methods for the extraction of differential spectra from the TDSE calculations are proposed. With these tools, some previously undetected processes are observed, and qualitative models are introduced to understand these processes. In addition, the electron-electron correlation effects in the static tunneling ionization of molecules are studied.

- **Chapter 2** introduces the TDSE for a diatomic molecule, and discusses different approximations and models for the TDSE that can be used to investigate different breakup dynamics.
- **Chapter 3** discusses the general numerical concepts and methods that are

used to solve the TDSE, including propagation methods, basis sets, and calculation strategies.

- **Chapter 4** discusses the efficient extraction of continuum observables from the TDSE calculations. The observables include the joint-energy spectrum (JES) for DI showing the continuum-energy sharing between the electron and nuclei; the nuclear kinetic energy release (NKER) spectrum for dissociation; and the PES for single-ionization in multielectron systems.
- **Chapter 5** investigates the dynamic interference effects for dissociative ionization in molecules. Two models are proposed to analyze the interference effects.
- **Chapter 6** investigates the molecular breakup processes in the very intense, femtosecond XUV pulse regime. It is revealed that stabilization w.r.t. ionization can occur, but with surprising, non-resonant dissociation dominating the dynamics. A molecular HFFT model is presented to explain the dynamics.
- **Chapter 7** presents evidence for inter- and intracycle effects in DI. An SFA model with inclusion of the nuclear energy is used to explain the results, and analytical formulas for a flat-top pulse are derived.
- **Chapter 8** presents a scheme to study static orientation-dependent tunneling ionization rates for molecules, by combining the multi-electron TD-GASCI method with the analytical WFAT. Results for H_2 and LiH are presented and discussed.
- **Chapter 9** summarizes the results of the thesis and gives a brief outlook.

CHAPTER 2

DIATOMIC MOLECULES IN INTENSE LASER FIELDS

When a diatomic molecule is exposed to an intense laser field, it can fragment by ionization, dissociation, or DI. In this chapter, the theoretical foundations for the investigation of such processes are discussed. The TDSE for a diatomic molecule is first introduced, followed by some relevant approximations to the TDSE suited for our investigations.

2.1 Time-dependent Schrödinger equation for diatomics

The TDSE provides the starting point for the modelling of non-relativistic quantum processes. In this section, we introduce the relevant Hamiltonians for a diatomic molecule.

2.1.1 The field-free Hamiltonian

The Hamiltonian for a N -electron diatomic molecule in the laboratory-fixed frame reads (the electron mass $m = 1$ is explicitly written)

$$\begin{aligned} H_0 = & \sum_i \frac{\mathbf{p}_{e,i}^2}{2m} + \frac{\mathbf{P}_A^2}{2M_A} + \frac{\mathbf{P}_B^2}{2M_B} \\ & - \sum_i \left(\frac{Z_A}{|\mathbf{r}_{e,i} - \mathbf{R}_A|} + \frac{Z_B}{|\mathbf{r}_{e,i} - \mathbf{R}_B|} \right) \\ & + \sum_{i < j} \frac{1}{|\mathbf{r}_{e,i} - \mathbf{r}_{e,j}|} + \frac{Z_A Z_B}{|\mathbf{R}_A - \mathbf{R}_B|}, \end{aligned} \tag{2.1}$$

with M_A and M_B the nuclear masses, Z_A and Z_B the nuclear charges, \mathbf{R}_A and \mathbf{R}_B the nuclear coordinates, $\mathbf{P}_A = -i\nabla_{\mathbf{R}_A}$ and $\mathbf{P}_B = -i\nabla_{\mathbf{R}_B}$ the nuclear momenta, and $\mathbf{r}_{e,i}$ and $\mathbf{p}_{e,i} = -i\nabla_{\mathbf{r}_{e,i}}$ the position and momentum of the i 'th electron, respectively. The sums in Eq. (2.1) run up to the number of electrons N .

2.1.2 The external field

In strong-field physics, the external electromagnetic field is treated classically in terms of a vector potential $\mathbf{A}(\mathbf{r}, t)$ and a scalar potential $\phi(\mathbf{r}, t)$. The electric field $\mathbf{F}(\mathbf{r}, t)$ and the magnetic field $\mathbf{B}(\mathbf{r}, t)$ are given by [74]

$$\begin{aligned}\mathbf{F}(\mathbf{r}, t) &= -\nabla\phi(\mathbf{r}, t) - \frac{\partial}{\partial t}\mathbf{A}(\mathbf{r}, t) \\ \mathbf{B}(\mathbf{r}, t) &= \nabla \times \mathbf{A}(\mathbf{r}, t).\end{aligned}\tag{2.2}$$

There is a gauge freedom in the choice of \mathbf{A} and ϕ that reproduces the physically measurable fields \mathbf{F} and \mathbf{B} :

$$\begin{aligned}\mathbf{A}(\mathbf{r}, t) &\rightarrow \mathbf{A}(\mathbf{r}, t) + \nabla f(\mathbf{r}, t) \\ \phi(\mathbf{r}, t) &\rightarrow \phi(\mathbf{r}, t) - \frac{\partial}{\partial t}f(\mathbf{r}, t),\end{aligned}\tag{2.3}$$

with f an arbitrary function. We choose to work in the Coulomb gauge $\nabla \cdot \mathbf{A} = 0$, and assume no sources such that $\phi = 0$. For electrons moving at non-relativistic speeds, the effect of electric field dominates over magnetic field, and in this thesis we set $\mathbf{B} \equiv 0$.

The fields considered in this thesis have spatial variations that are negligible on length scales comparable to the molecular dimensions. This allows the use of the dipole approximation

$$\begin{aligned}\mathbf{A}(\mathbf{r}, t) &\approx \mathbf{A}(\mathbf{R}_{CM}, t) \equiv \mathbf{A}(t), \\ \mathbf{F}(\mathbf{r}, t) &\approx \mathbf{F}(\mathbf{R}_{CM}, t) \equiv \mathbf{F}(t),\end{aligned}\tag{2.4}$$

with \mathbf{R}_{CM} the center of mass. In this thesis, we will employ the dipole approximation, and only consider linearly polarized pulses,

$$\begin{aligned}\mathbf{A}(t) &= A(t)\hat{\mathbf{z}}, \\ \mathbf{F}(t) &= F(t)\hat{\mathbf{z}}.\end{aligned}\tag{2.5}$$

In our calculations, we specify either the electric field or the vector potential on the form,

$$\begin{aligned}A(t) &= A_0g(t) \cos[\omega(t - T_{\text{mid}}) + \varphi_{\text{CEP}}], \\ F(t) &= F_0g(t) \cos[\omega(t - T_{\text{mid}}) + \varphi_{\text{CEP}}].\end{aligned}\tag{2.6}$$

Owing the knowledge of one of these quantities, the second is obtained through the relation $F(t) = -(d/dt)A(t)$. In Eq. (2.6), F_0 is the peak field strength, ω the angular carrier frequency, T_{mid} the time corresponding to the maximum of the pulse envelope $g(t)$, φ_{CEP} the carrier-envelope phase (CEP), and $A_0 \equiv F_0/\omega$. The peak intensity is $I = F_0^2$. The pulse envelope is chosen either to be of Gaussian form or sine-squared form.

$$g(t) = \begin{cases} e^{-4\ln 2 \frac{t^2}{\tau^2}}, & \tau = 2\sqrt{\ln 2} N_c T_c, \quad t \in [-\infty, \infty], \quad (\text{Gauss}), \quad (2.7a) \\ \sin^2(\pi t/\tau), & \tau = N_c T_c, \quad t \in [0, \tau], \quad (\text{sinesq}), \quad (2.7b) \end{cases}$$

with the period $T_c = 2\pi/\omega$.

2.1.3 The time-dependent Hamiltonian

For time-dependent processes, the external field is included in the Hamiltonian by replacing the canonical momenta with the kinematic momenta [74], resulting in the Hamiltonian:

$$\begin{aligned} H_{\text{tot}}(t) = & \sum_i \frac{[\mathbf{p}_{e,i} + \mathbf{A}(t)]^2}{2m} + \frac{[\mathbf{P}_A - Z_A \mathbf{A}(t)]^2}{2M_A} + \frac{[\mathbf{P}_B - Z_B \mathbf{A}(t)]^2}{2M_B} \\ & - \sum_i \left(\frac{Z_A}{|\mathbf{r}_{e,i} - \mathbf{R}_A|} + \frac{Z_B}{|\mathbf{r}_{e,i} - \mathbf{R}_B|} \right) + \sum_{i < j} \frac{1}{|\mathbf{r}_{e,i} - \mathbf{r}_{e,j}|} + \frac{Z_A Z_B}{|\mathbf{R}_A - \mathbf{R}_B|} \end{aligned} \quad (2.8)$$

It is convenient to transform the Hamiltonian to the relative coordinates

$$\begin{aligned} \mathbf{R}_{CM} &= \frac{M_A \mathbf{R}_A + M_B \mathbf{R}_B + m \sum_i \mathbf{r}_{e,i}}{M_{\text{tot}}} \\ \mathbf{R} &= \mathbf{R}_A - \mathbf{R}_B \\ \mathbf{r}_i &= \mathbf{r}_{e,i} - \frac{M_A \mathbf{R}_A + M_B \mathbf{R}_B}{M_A + M_B}, \end{aligned} \quad (2.9)$$

with $M_{\text{tot}} = M_A + M_B + Nm$ the total mass, \mathbf{R}_{CM} the center of mass, \mathbf{R} the internuclear distance vector, and \mathbf{r}_i the relative coordinate of the i 'th electron with respect to the center of mass of the nuclei. The laboratory-fixed and the relative coordinates are shown in Fig. 2.1.

After some algebra, the Hamiltonian in the new coordinates reads

$$H_{\text{tot}}(t) = H_{CM}(t) + T_e + T_N + V_{ee} + V_{eN} + V_N + V_L(t) + V_{mp} \quad (2.10)$$

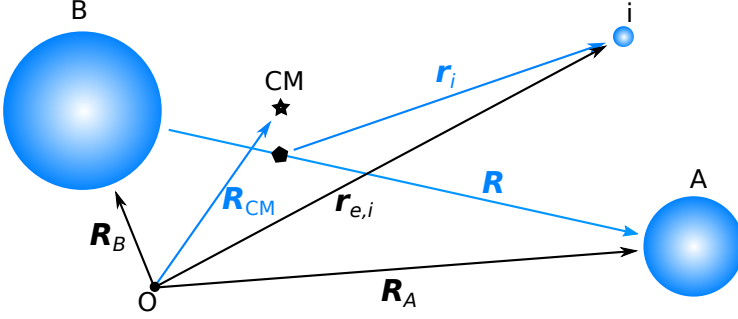


Figure 2.1: A sketch of the laboratory-fixed coordinates (black arrows) and relative coordinates (blue arrows) for an N -electron diatomic molecule. For illustration purposes, only a single electron is drawn. In the figure, O is the origin of the laboratory-fixed frame, A and B are the two nuclei, i is the i 'th electron, the star is the center of mass of the total system, and the pentagon is the center of mass of the nuclei.

with

$$\begin{aligned}
 H_{CM}(t) &= \frac{\mathbf{P}_{CM}^2}{2M_{\text{tot}}} + \beta_{CM} \mathbf{P}_{CM} \cdot \mathbf{A}(t), \\
 T_e &= \sum_i \frac{\mathbf{p}_i^2}{2\mu}, \quad T_N = \frac{\mathbf{P}_N^2}{2M_N}, \\
 V_{ee} &= \sum_{i < j} \frac{1}{|\mathbf{r}_i - \mathbf{r}_j|}, \\
 V_{eN} &= - \sum_i \left(\frac{Z_A}{|\mathbf{r}_i - \rho_A \mathbf{R}|} + \frac{Z_B}{|\mathbf{r}_i - \rho_B \mathbf{R}|} \right), \\
 V_N &= \frac{Z_A Z_B}{R}, \quad V_{mp} = \sum_{i \neq j} \frac{\mathbf{p}_i \mathbf{p}_j}{2(M_A + M_B)}, \\
 V_L(t) &= \left[\beta_N \mathbf{P}_N + \beta \sum_i \mathbf{p}_i \right] \cdot \mathbf{A}(t) + \beta_F \frac{A^2(t)}{2}
 \end{aligned} \tag{2.11}$$

and

$$\begin{aligned}
 \mathbf{P}_{CM} &= -i \nabla_{\mathbf{R}_{CM}}, \quad \beta_{CM} = \frac{N - Z_A - Z_B}{M_{\text{tot}}}, \\
 \mathbf{P}_N &= -i \nabla_{\mathbf{R}}, \quad M_N = \frac{M_A M_B}{M_A + M_B}, \quad \beta_N = \frac{-Z_A M_B + Z_B M_A}{M_A M_B}, \\
 \mathbf{p}_i &= -i \nabla_{\mathbf{r}_i}, \quad \mu = \frac{M_A + M_B}{M_{\text{tot}}}, \quad \beta = \frac{M_A + M_B + (Z_A + Z_B)m}{M_A + M_B}, \\
 \rho_A &= \frac{M_B}{M_A + M_B}, \quad \rho_B = \frac{M_A}{M_A + M_B}, \quad \beta_F = \frac{N}{m} + \frac{Z_A^2}{M_A} + \frac{Z_B^2}{M_B}.
 \end{aligned} \tag{2.12}$$

The mass polarization term V_{mp} in Eq. (2.11) is small and is neglected throughout this thesis. The Hamiltonian H_{CM} in Eqs. (2.10) and (2.11) is only dependent on the center of mass coordinates and thus can be separated in the total Hamiltonian. The center of mass motion corresponds to a free charged particle moving in a laser field, which is described in the following.

2.1.4 A charged particle in a laser field

The TDSE for the motion of a free charged particle with mass m and charge q in a laser field has the general form

$$i\frac{\partial}{\partial t}\psi(\mathbf{r}, t) = \left[\frac{\mathbf{p}^2}{2m} - \frac{q}{m}\mathbf{p} \cdot \mathbf{A}(t) \right] \psi(\mathbf{r}, t), \quad (2.13)$$

with \mathbf{p} the momentum operator. The general solution to Eq. (2.14) are Volkov waves

$$\psi_{\mathbf{k}}^V(\mathbf{r}, t) = (2\pi)^{-3/2} \exp \{ i\mathbf{k} \cdot [\mathbf{r} - \boldsymbol{\alpha}(t)] - iEt \}, \quad (2.14)$$

with

$$\boldsymbol{\alpha}(t) = -\frac{q}{m} \int^t \mathbf{A}(t') dt' \quad (2.15)$$

the quiver motion describing the position of a classical charged particle in the presence of an electric field $\mathbf{F}(t)$ and $E = k^2/2m$ the kinetic energy of the particle.

2.1.5 The Hamiltonian for relative motion

After separating out the center of mass motion from H_{tot} in Eq. (2.10), the TDSE describing the relative motion for the diatomic reads

$$i\frac{\partial}{\partial t}\Psi(t) = H(t)\Psi(t) \quad (2.16)$$

with the Hamiltonian

$$H(t) = T_e + T_N + V_{ee} + V_{eN} + V_N + V_L(t), \quad (2.17)$$

and the expression for the individual terms given by Eq. (2.11).

Under the unitary transformation

$$\Psi'(t) = U^\dagger(t)\Psi(t), \quad (2.18)$$

with $U(t)$ and $\Psi(t)$ functions of the coordinates \mathbf{r}_i and \mathbf{R} , the TDSE in Eq. (2.16) can be rewritten as

$$i\frac{\partial}{\partial t}\Psi'(t) = H'(t)\Psi'(t), \quad (2.19)$$

with

$$H'(t) = U^\dagger(t)H(t)U(t) - iU^\dagger(t)\frac{\partial U(t)}{\partial t}. \quad (2.20)$$

2.1.6 Velocity gauge Hamiltonian

By choosing the unitary transformation

$$U^{\text{VG}}(t) = \exp\left(-\frac{i\beta_F}{2} \int^t A^2(t') dt'\right) \quad (2.21)$$

for H in Eq. (2.20), we obtain the transformed Hamiltonian in the velocity gauge (VG)

$$H^{\text{VG}}(t) = T_e + T_N + V_{ee} + V_{eN} + V_N + V_L^{\text{VG}}(t), \quad (2.22)$$

with

$$V_L^{\text{VG}}(t) = \left[\beta_N \mathbf{P}_N + \beta \sum_i \mathbf{p}_i \right] \cdot \mathbf{A}(t), \quad (2.23)$$

where we have transformed away the term containing $A^2(t)$.

2.1.7 Length gauge Hamiltonian

Starting from the total Hamiltonian H_{tot} in Eq. (2.1), using the transformation

$$U^{\text{LG}}(t) = \exp\left[-i\mathbf{A}(t) \cdot \left(\sum_i \mathbf{x}_i - Z_A \mathbf{R}_A - Z_B \mathbf{R}_B\right)\right], \quad (2.24)$$

separating out the center of mass motion, and neglecting V_{mp} , we obtain the Hamiltonian for relative motion in length gauge (LG):

$$H(t) = T_e + T_N + V_{ee} + V_{eN} + V_N + V_L^{\text{LG}}(t), \quad (2.25)$$

with

$$V_L^{\text{LG}}(t) = \left(\beta_N^{\text{LG}} \mathbf{R} + \beta^{\text{LG}} \sum_i \mathbf{r}_i \right) \cdot \mathbf{F}(t) \quad (2.26)$$

and

$$\beta_N^{\text{LG}} = \frac{-Z_A M_B + Z_B M_A}{M_A + M_B}, \quad \beta^{\text{LG}} = 1 + \frac{(Z_A + Z_B - N)m}{M_{\text{tot}}}. \quad (2.27)$$

2.1.8 Approximations to the TDSE

Currently, due to the non-perturbative nature of the strong laser field, a direct numerical solution to the TDSE with the Hamiltonian in Eq. (2.22) or Eq. (2.25) is only possible for two-electron atomic systems. Even for these small systems, a small simulation volume must be employed to make the calculations feasible. To

simulate the strong-field ionization dynamics, one usually has to resort to making approximations and employ model molecules. The approximations and physical models should be chosen such that it best describes the physics at hand. In the next section, we will discuss the different approximations and model molecules employed in this thesis.

2.2 Pure dissociation dynamics: The surface model

In situations where the dominant breakup process is the dissociation of the neutral diatomic, and the population into the electronic continua are negligible, we can reduce the TDSE to a form where the electronic continua are neglected entirely.

First, we make the axial recoil approximation. Since the rotational time-scale is in the near-picosecond to picosecond regime, and the laser pulses considered in this work have up to tens of femtoseconds (fs) duration, the molecules are assumed to be rotationally frozen, with the breakup along the internuclear axis. The momentum operator \mathbf{P}_N is then

$$\mathbf{P}_N = -i\hat{\mathbf{R}}\frac{\partial}{\partial R}. \quad (2.28)$$

and the kinetic energy operator in Eq. (2.11) reduces to

$$T_N = -\frac{1}{2M_N}\frac{\partial^2}{\partial R^2}. \quad (2.29)$$

This approximation is employed throughout the thesis.

The adiabatic BO basis states $|\phi_{el,i}(R)\rangle$ are obtained as solutions to the electronic time-independent Schrödinger equation (TISE) with parametric dependence on R :

$$\left(T_e + V_{eN} + V_N + V_{ee}\right) |\phi_{el,i}(R)\rangle = E_{el,i}(R) |\phi_{el,i}(R)\rangle, \quad (2.30)$$

where $E_{el,i}(R)$ is the i 'th electronic potential energy surface in the BO approximation. Assume now that only the N_{BO} lowest bound electronic states are involved in the dynamics. By inserting the ansatz

$$|\Psi(R, t)\rangle = \sum_i^{N_{BO}} G_i(R, t) |\phi_{el,i}(R)\rangle \quad (2.31)$$

into the TDSE, and projecting onto the BO basis states, the TDSE can be rewritten as:

$$i\frac{\partial}{\partial t}\mathbf{G}(R, t) = \left[\mathbf{H}^{(1)}(t) + \mathbf{H}^{(2)}(t) + \mathbf{H}^{(3)}\right]\mathbf{G}(R, t), \quad (2.32)$$

with $\mathbf{G}(R, t) = [G_1(R, t), \dots, G_N(R, t)]^T$, $\mathbf{H}^{(1)}$ a diagonal matrix

$$[\mathbf{H}^{(1)}(t)]_{ij} = [T_N + E_{el,i}(R) + V_{I,N}(R, t)] \delta_{i,j}, \quad (2.33)$$

$\mathbf{H}^{(2)}$ an off-diagonal matrix containing the electron-laser coupling, and $\mathbf{H}^{(3)}$ a matrix containing the non-adiabatic coupling terms. The three matrices have dimensions $N_{BO} \times N_{BO}$. In Eq. (2.33), to account for ionization out of the system and absorption at the grid boundaries, an extra term can be added

$$[\mathbf{H}^{(1)}(t)]_{ij} \rightarrow [\mathbf{H}^{(1)}(t)]_{ij} - i \left[\frac{\Gamma_i(R)}{2} + V_{CAP}(R) \right] \delta_{i,j}, \quad (2.34)$$

containing the R -dependent ionization rates Γ_i and a complex absorbing potential V_{CAP} (see Section 3.1). We will work in the LG, so that

$$\begin{aligned} V_{I,N}(R, t) &= \beta_N^{LG} R F(t) \cos \theta_N \\ [\mathbf{H}^{(2)}(t)]_{ij} &= \beta^{LG} [\mathbf{D}(R)]_{ij} F(t), \end{aligned} \quad (2.35)$$

with θ_N the angle between $\mathbf{F}(t)$ and \mathbf{R} , and $[\mathbf{D}(R)]_{ij} = \langle \phi_{el,i}(R) | \sum_k z_k | \phi_{el,j}(R) \rangle$. The bra-ket notation $\langle \cdot | \cdot \rangle$ is used here to denote integration over the electronic coordinates. The non-adiabatic terms,

$$\begin{aligned} [\mathbf{H}^{(3)}(t)]_{ij} &= -\frac{1}{2M_N} \left[\langle \phi_{el,i}(R) | \frac{\partial^2}{\partial R^2} | \phi_{el,j}(R) \rangle \right. \\ &\quad \left. + 2 \langle \phi_{el,i}(R) | \frac{\partial}{\partial R} | \phi_{el,j}(R) \rangle \frac{\partial}{\partial R} \right], \end{aligned} \quad (2.36)$$

are neglected throughout this thesis, due to the small factor $1/M_N$ and the fact that we do not consider physics near avoided crossings.

2.3 Dissociation and dissociative ionization: 1D H_2^+

In situations where we want to study the electron-nuclear correlation effects in breakup processes, we will consider the simplest molecule, H_2^+ . This molecule was used to discover many processes that were later observed in more complex molecules, including charge-resonance-enhanced ionization [13, 14], bond-softening [15, 16], bond-hardening [15, 17], and above-threshold Comlumb explosion [19]. To capture the essential physics while keeping the computational effort manageable, we consider a colinear model that includes only the dimension that is aligned with the linearly polarized pulse, shown in Fig. 2.1. Since there

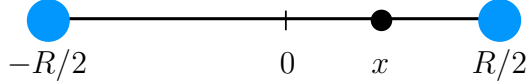


Figure 2.2: One dimensional colinear model of H_2^+ with electronic coordinate x and internuclear distance R , both along the polarization direction of the laser pulse.

is only one dimension, we choose it to be the x -axis. This choice will be used throughout the thesis for 1D H_2^+ .

The Hamiltonian reduces to

$$H = T_e + T_N + V_{eN} + V_N + V_L(t) \quad (2.37)$$

with

$$\begin{aligned} T_e &= -\frac{1}{2\mu} \frac{d^2}{dx^2}, & T_N &= -\frac{1}{m_p} \frac{d^2}{dR^2}, & V_N &= \frac{1}{R} \\ V_{eN} &= -\frac{1}{\sqrt{(x - \frac{R}{2})^2 + a(R)}} - \frac{1}{\sqrt{(x + \frac{R}{2})^2 + a(R)}}, & & & & (2.38) \\ V_L(t) &= \begin{cases} -i\beta A(t) \frac{\partial}{\partial x}, & \text{(VG)} \\ \beta^{\text{LG}} E(t)x, & \text{(LG)} \end{cases} \end{aligned}$$

where $m_p = 1836$ is the proton mass, $\beta = (m_p + 1)/m_p$, $\beta^{\text{LG}} = 1 + 1/(2m_p + 1)$, and the softening parameter $a(R)$ for the Coulomb singularity is chosen to produce the exact three-dimensional ground state BO potential energy curve [75], such that the dynamics in this model is as close to the real three-dimensional case as possible. The H_2^+ molecule allows us to study dissociation and DI.

2.4 Electron-electron correlations: The TD-GASCI scheme

In situations where one wants to study electron-electron correlation effects in strong-field breakup of diatomics, multi-electron methods should be employed. One of such methods is the TD-GASCI method [67, 68], which can consistently include correlation effects. We here give a brief overview of the method.

2.4.1 Fixed-nuclei Hamiltonian

Since the masses of the nuclei are much greater the electron mass, one often assumes the limit $M_A, M_B \rightarrow \infty$, and the Hamiltonian reduces to

$$H(t) = \sum_{i=1}^N h_i(\mathbf{r}, t) + \frac{1}{2} \sum_{i \neq j} \frac{1}{|\mathbf{r}_i - \mathbf{r}_j|} + \frac{Z_A Z_B}{R}, \quad (2.39)$$

where

$$h_i(\mathbf{r}, t) = \frac{\mathbf{p}_i^2}{2} - \frac{Z_A}{|\mathbf{r}_i - \mathbf{R}_A|} - \frac{Z_B}{|\mathbf{r}_i - \mathbf{R}_B|} + v_L(\mathbf{r}_i, t) \quad (2.40)$$

with $v_L(\mathbf{r}_i, t)$ equal to $-i\mathbf{A}(t)\nabla_{\mathbf{r}_i}$ in VG and $\mathbf{E}(t)\mathbf{r}_i$ in LG. This FNA is assumed in the TD-GASCI method.

2.4.2 Second quantization

When dealing with multiple identical particles, the second quantized formulation of quantum mechanics is preferred [76]. Instead of representing the physical states with functions, there are expressed by operator strings in second quantization. The antisymmetry requirement for the electronic wave function follows directly from the commutation relations of these operators, and evaluation of matrix elements reduces to algebraic operator manipulations.

The Slater determinants provide an antisymmetrized basis for the total wave function. Consider a single-particle basis given in terms of $2N_b$ spin orbitals $\{\bar{\phi}_{\bar{i}}\}_{\bar{i}=1}^{2N_b}$ where a bar in the index is to indicate a spin-orbital index consisting of a spatial-orbital index and a spin projection quantum number. The spin orbitals are chosen on the spin-restricted form

$$\bar{\phi}_{\bar{i}}(\mathbf{r}, \sigma) = \phi_i(\mathbf{r})\chi_{m_s}(\sigma) = \phi_i(\mathbf{r})\delta_{m_s\sigma}, \quad (2.41)$$

where the same set of spatial orbitals are chosen for $m_s = -1/2$ and $m_s = 1/2$. \bar{i} and i are related by $\bar{i}/2 = i$ for even \bar{i} , and $(\bar{i} + 1)/2 = i$ for odd \bar{i} . If the N electrons occupy the spin orbitals $\bar{\phi}_{\bar{i}_1}, \dots, \bar{\phi}_{\bar{i}_N}$, one can denote the determinant in terms of the occupied orbital indices $I \equiv (\bar{i}_1, \dots, \bar{i}_N)$,

$$|I\rangle = |\bar{i}_1, \dots, \bar{i}_N\rangle. \quad (2.42)$$

We will refer to this representation as the *Slater representation*. Alternatively, one can write the determinant in the *occupation-number representation* in terms of the occupation number vectors $|\mathbf{n}\rangle$,

$$|\mathbf{n}\rangle = |n_1, \dots, n_{2N_b}\rangle, \quad (2.43)$$

with $n_{\bar{k}}$ (equal to 0 or 1) denoting the occupation number in the spin orbital $\phi_{\bar{k}}$, with

$$N = \sum_{\bar{k}=1}^{2N_b} n_{\bar{k}}. \quad (2.44)$$

They satisfy the orthonormality condition

$$\langle \mathbf{m} | \mathbf{n} \rangle = \prod_{\bar{i}=1}^{2N_b} \delta_{m_{\bar{i}}, n_{\bar{i}}}. \quad (2.45)$$

In second quantization, a creation operator $\hat{a}_{\bar{p}}^\dagger$ and an annihilation operator $\hat{a}_{\bar{p}}$ can be defined in terms of their action on a Slater determinant

$$\hat{a}_{\bar{p}}^\dagger |n_1, \dots, n_{\bar{p}}, \dots, n_{2N_b}\rangle = \delta_{n_{\bar{p}}, 0} \Gamma_{\bar{p}}^{\mathbf{n}} |n_1, \dots, 1_{\bar{p}}, \dots, n_{2N_b}\rangle \quad (2.46)$$

$$\hat{a}_{\bar{p}} |n_1, \dots, n_{\bar{p}}, \dots, n_{2N_b}\rangle = \delta_{n_{\bar{p}}, 1} \Gamma_{\bar{p}}^{\mathbf{n}} |n_1, \dots, 0_{\bar{p}}, \dots, n_{2N_b}\rangle, \quad (2.47)$$

with the phase factor

$$\Gamma_{\bar{p}}^{\mathbf{n}} = \prod_{\bar{q}=1}^{\bar{p}-1} (-1)^{n_{\bar{q}}}. \quad (2.48)$$

The operator $\hat{a}_{\bar{p}}^\dagger$ thus “creates” a particle in the spin orbital $\bar{\phi}_{\bar{p}}$ if it is initially unoccupied, and returns zero if it is occupied, while $\hat{a}_{\bar{p}}^\dagger$ “annihilates” a particle in the spin orbital $\bar{\phi}_{\bar{p}}$ if it is initially occupied, and returns zero if it is unoccupied. Using Eqs. (2.46) and (2.47), one arrives at the anticommutation relations

$$\{\hat{a}_{\bar{p}}^\dagger, \hat{a}_{\bar{q}}^\dagger\} = \{\hat{a}_{\bar{p}}, \hat{a}_{\bar{q}}\} = 0 \quad (2.49a)$$

$$\{\hat{a}_{\bar{p}}, \hat{a}_{\bar{q}}^\dagger\} = \delta_{\bar{p}, \bar{q}}, \quad (2.49b)$$

with the curly brackets denoting the anticommutator $\{A, B\} \equiv AB + BA$. A Slater determinant can be written in terms of the creation operators

$$|I\rangle = \prod_{\bar{p}=1}^{2N_b} (\hat{a}_{\bar{p}}^\dagger)^{n_{\bar{p}}} |0\rangle, \quad (2.50)$$

with the vacuum state $|0\rangle = |0_1, \dots, 0_{2N_b}\rangle$ satisfying $\langle 0|0\rangle = 1$.

The molecular electronic Hamiltonian in second quantization is given by

$$H(t) = \sum_{pq} h_{pq}(t) \sum_{\sigma} \hat{a}_{p\sigma}^\dagger \hat{a}_{q\sigma} + \frac{1}{2} \sum_{pqrs} g_{pqrs} \sum_{\tau\sigma} \hat{a}_{p\sigma}^\dagger \hat{a}_{r\tau}^\dagger \hat{a}_{s\tau} \hat{a}_{q\sigma}, \quad (2.51)$$

with the one-electron matrix elements

$$h_{pq}(t) = \int \phi_p^*(\mathbf{r}) h(\mathbf{r}, t) \phi_q(\mathbf{r}) d\mathbf{r}, \quad (2.52)$$

and the two-electron integrals

$$g_{pqrs} = \int \int \phi_p^*(\mathbf{r}) \phi_q(\mathbf{r}) \frac{1}{|\mathbf{r} - \mathbf{r}'|} \phi_r^*(\mathbf{r}') \phi_s(\mathbf{r}') d\mathbf{r} d\mathbf{r}'. \quad (2.53)$$

Using the properties above, the Slater-Condon rules used to evaluate matrix elements can be derived [76].

2.4.3 Hartree-Fock approximation

The first step in most advanced quantum chemistry methods is to find an optimal Slater determinant $|\mathbf{n}\rangle$ that attains the lowest expectation energy. Such a determinant can be determined by the Hartree-Fock (HF) method. Here, we assume that the number of electrons N is even, with each spatial orbital doubly occupied (closed shell).

The spatial orbitals are expanded in an orthonormal basis $\{f_j\}_{j=1}^{N_b}$,

$$|\phi_i\rangle = \sum_{j=1}^{N_b} c_{ji} |f_j\rangle, \quad (2.54)$$

with the expansion coefficients c_{ji} to be determined by minimizing the Lagrangian under the orthonormality constraint $\langle \phi_i | \phi_j \rangle = \delta_{ij}$

$$\mathcal{L}(\{c_{ji}\}, \{\mu_{ij}\}) = E_0(\{c_{ji}\}) - \sum_{ij} \mu_{ij} (\langle \phi_i | \phi_j \rangle - \delta_{ij}), \quad (2.55)$$

with the Lagrange multipliers μ_{ij} , and the HF energy

$$E_0(\{c_{ji}\}) = \langle \mathbf{n} | H_0 | \mathbf{n} \rangle = 2 \sum_p^{N/2} h_{pp} + \sum_{pq}^{N/2} (2g_{ppqq} - g_{pqqp}), \quad (2.56)$$

where H_0 is the Hamiltonian in Eq. (2.51) without the laser-matter interaction. Carrying out the minimization $\delta\mathcal{L} = 0$, one arrives at the HF eigenvalue equations

$$\mathbf{F}\mathbf{c} = \mathbf{c}\boldsymbol{\epsilon}, \quad (2.57)$$

where $\boldsymbol{\epsilon}$ is a diagonal matrix containing the orbital energies, and \mathbf{F} is the Fock matrix with elements

$$F_{ij} = h_{ij} + \sum_{kl}^{N/2} D_{kl} \left(g_{ijkl} - \frac{1}{2} g_{ilkj} \right), \quad (2.58)$$

and D_{kl} is

$$D_{kl} = 2 \sum_i^{N/2} c_{ki} c_{li}. \quad (2.59)$$

Since the Fock matrix \mathbf{F} depends on the solution \mathbf{c} in the HF equation (2.57), HF is a self-consistent-field theory that must be solved iteratively. The initial guess of \mathbf{c} to start the iteration is often taken as the solution to Eq. (2.57) without electronic correlation ($V_{ee} = 0$). The $N/2$ HF spatial orbitals with the smallest orbital energies are the *occupied orbitals*, while the higher-energy orbitals are *virtual orbitals*. Henceforth, we will refer to the orthonormal basis $\{f_j\}_{j=1}^{N_b}$ as the *primitive* basis.

2.4.4 Configuration interaction

The HF theory is a mean-field theory that approximates the exact wave function with a single optimal Slater determinant. To obtain the most accurate ground state $|\Psi_0\rangle$ in a given primitive basis, one can employ a full configuration interaction (FCI) ansatz, where the wave function is expanded in terms of a linear combination of all possible Slater determinants (configurations):

$$|\Psi_0\rangle = \sum_{I \in \Omega_{\text{FCI}}} C_I |I\rangle. \quad (2.60)$$

In Slater representation, the FCI index space is

$$\Omega_{\text{FCI}} = \{(\bar{i}_1, \dots, \bar{i}_N) | 1 \leq \bar{i}_1 < \dots < \bar{i}_N \leq 2N_b\}. \quad (2.61)$$

While being the most accurate method, the number of possible configurations in FCI scales as

$$n_{\text{conf}}^{\text{FCI}} = \binom{2N_b}{N} = \frac{(2N_b)!}{N!(2N_b - N)!}, \quad (2.62)$$

which restricts the feasibility of the FCI method to small systems and small primitive basis sets. In time-dependent breakup simulations, a large primitive basis is especially required in order to correctly describe the continua.

For computational feasibility, the configuration space can be truncated. A host of such truncated CI methods exist, such as CI-singles (CIS), where all single-excited configurations from the HF state are added to the CI ansatz, and CI singles and doubles, where single- and double-excited configurations are included. The CI method with the most flexibility is the generalized-active-space CI method, where the single-particle spin-orbital space is divided into P partitions

[67]

$$\begin{aligned}\mathcal{B} &= \{|\bar{\phi}_1\rangle, \dots, |\bar{\phi}_{2N_b}\rangle\} \equiv \mathcal{B}_1 \cup \dots \cup \mathcal{B}_P, \\ \mathcal{B}_i &= \{|\bar{\phi}_{p_{(i-1)}}\rangle, \dots, |\bar{\phi}_{p_i-1}\rangle\}.\end{aligned}\tag{2.63}$$

The allowed number of electrons N_i in each partition i is then specified by restricting the minimum and maximum particle numbers $N_{\min,i} < N_i < N_{\max,i}$. As a result, in the GASCI, the configuration index space in the Slater representation is

$$\Omega_{\text{GAS}} = \{(\bar{i}_1, \dots, \bar{i}_N) \in \Omega_{\text{FCI}} | \forall j \in \{1, \dots, P\} : N_{\min,j} \leq N_j \leq N_{\max,j}\}, \tag{2.64}$$

with the dimension of the corresponding configuration space

$$n_{\text{conf}}^{\text{GAS}} = \sum_{\substack{N_{\min,j} \leq N_j \leq N_{\max,j} \\ \sum_j N_j = N}} \binom{N_{b,1}}{N_1} \dots \binom{N_{b,P}}{N_P}, \tag{2.65}$$

where $N_{b,j}$ is the number of spin orbitals in the j th partition \mathcal{B}_j .

The required input for a GASCI partition is thus the number of partitions P , the numbers $\{p_0 = 1, p_1 \dots, p_{P-1}, p_P = 2N_b\}$, and the minimum and maximum particles in each partition. For example, CIS corresponds to $P = 2$, $p_1 = N + 1$, $(N_{\min,1}, N_{\max,1}) = (N - 1, N)$, and $(N_{\min,2}, N_{\max,2}) = (0, 1)$. The FCI result is obtained when $(N_{\min,i}, N_{\max,i}) = (0, N)$ for all i .

In the FCI, a unitary transformation of the virtual HF orbital space leaves the FCI solution invariant (with different expansion coefficients), while in the truncated CI methods, this is not the case. A good choice of the virtual orbitals is thus important for the convergence of a truncated CI method.

2.4.5 Time-dependent GASCI

In the time-dependent GASCI (TD-GASCI) treatment of time-dependent problems [67, 68], the expansion coefficients in the GASCI expansion is taken to be time dependent,

$$|\Psi(t)\rangle = \sum_{I \in \Omega_{\text{GAS}}} C_I(t) |I\rangle. \tag{2.66}$$

After insertion into the TDSE and projection onto the determinant $\langle J|$, one arrives at the TDSE in matrix form for the CI-coefficients,

$$i\dot{C}_I(t) = \sum_{J \in \Omega_{\text{GAS}}} H_{IJ}(t) C_J(t), \tag{2.67}$$

with the CI matrix elements $H_{IJ}(t) = \langle I| H(t) |J\rangle$. As mentioned, the continuum should be well-represented in time-dependent breakup phenomena, requiring a

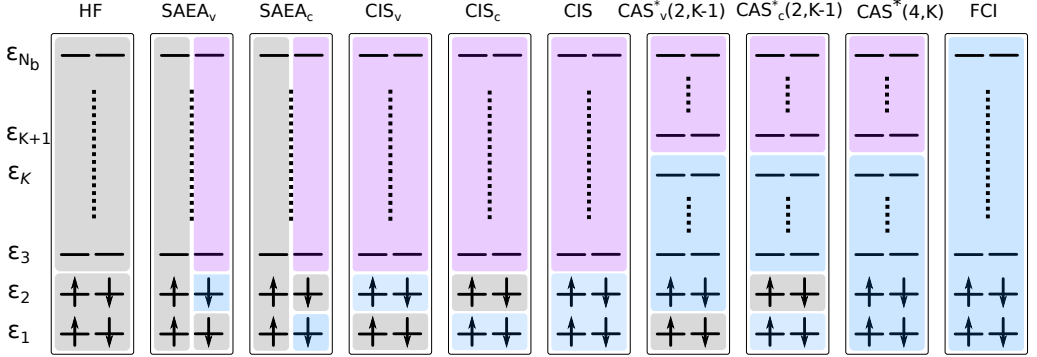


Figure 2.3: A hierarchy of TD-GASCI methods for a 4-electron system. Different spin-orbital subspaces are marked by different colors: the orbitals inside a gray subspace are frozen; all possible orbital excitations are allowed inside a blue subspace; and a purple orbital space only allows single-excitation from a blue subspace. The subscript “v” in the method notations stands for “valence excitation”, while “c” stands for “core excitation”. HF, CIS_v, and CAS_v^{*} methods will be used in this work.

larger simulation volume compared to time-independent problems. This, together with the the scaling of the configuration-space dimension, allows only one electron in the continuum. A hierarchy of GAS-partitions for a 4-electron system is illustrated in Fig. 2.3. In the GAS-partition denoted by CAS_v^{*}(N_{act} , K), the star refers to the possibility of occupation of a single spin orbital in \mathcal{B}_P (possibility of single-ionization), N_{act} denotes the number of active electrons that can be excited in \mathcal{B}_{P-1} , and K denotes the number of orbitals in \mathcal{B}_{P-1} . CAS stands for “complete-active-space”. With the GAS-methods, electron-electron correlation effects can be included, as well as the possibility of single ionization into the continuum. In this thesis, we will use the HF, CIS_v, and CAS_v^{*}(2, K) methods. For notational simplicity, we will denote CIS_v by CIS, and CAS_v^{*}(2, K) by CAS^{*}(2, K).

CHAPTER 3

NUMERICAL SOLUTIONS OF THE TDSE

This chapter is concerned with the numerical solutions of the TDSE. Some general numerical concepts are first introduced, followed by a discussion on the solutions of the model systems presented in Chapter 2.

3.1 Generic numerical concepts

To solve the TDSE, the time-evolution operator (TEO) is usually employed. Assuming the initial state of the system at time t_0 is known, the TEO predicts the state at a later time t :

$$|\Psi(t)\rangle = \mathcal{U}(t, t_0) |\Psi(t_0)\rangle. \quad (3.1)$$

The TEO must satisfy the TDSE and the following properties:

$$\begin{aligned} \lim_{t \rightarrow t_0} \mathcal{U}(t, t_0) &= 1 \\ \mathcal{U}^\dagger(t, t_0) \mathcal{U}(t, t_0) &= 1 \\ \mathcal{U}(t_2, t_1) \mathcal{U}(t_1, t_0) &= \mathcal{U}(t_2, t_0). \end{aligned} \quad (3.2)$$

For time-independent Hamiltonians H , the TEO reads

$$\mathcal{U}(t, t_0) = \exp[-iH(t - t_0)], \quad (3.3)$$

while for time-dependent Hamiltonians $H(t)$, the general expression for the TEO is

$$\mathcal{U}(t, t_0) = \mathcal{T} \exp \left[-i \int_{t_0}^t H(t') dt' \right], \quad (3.4)$$

with \mathcal{T} the time-ordering operator.

The closed form in Eq. (3.4) is of little practical use in the present context of solving the TDSE numerically. Instead, we approximate the time-dependent

Hamiltonian as a series of piecewise time-independent Hamiltonians, and approximate the TEO between t and $t + \Delta t$ as

$$\mathcal{U}(t + \Delta t, t) = \exp[-iH(t)\Delta t]. \quad (3.5)$$

We will refer to the TEO between t and $t + \Delta t$ in Eq. (3.5) as *the short-time propagator*.

3.1.1 The initial state

To solve the TDSE, an initial state must be specified. In many cases, this is chosen as the ground state $|\Psi_0\rangle$ of the system, corresponding to the smallest eigenvalue solution to the TISE. If a numerical propagator for the TDSE is implemented, the same propagator can be used to obtain the ground state by propagating in imaginary time.

In the ITP method, the t is rewritten in terms of an imaginary time variable, $t = -i\tau$, with τ real, and substituted into the TEO:

$$\mathcal{U}(\tau, 0) = \exp(-H_0\tau), \quad (3.6)$$

with H_0 the time-independent Hamiltonian. Action of this operator on a trial state $|\Phi\rangle$ yields

$$\begin{aligned} \mathcal{U}(\tau, 0) |\Phi\rangle &= \sum_i c_i \mathcal{U}(\tau, 0) |\Psi_i\rangle \\ &= \sum_i c_i \exp(-E_i\tau) |\Psi_i\rangle \end{aligned} \quad (3.7)$$

where we have expanded $|\Phi_0\rangle$ in terms of the eigenstates $|\Psi_i\rangle$ of H_0 . With increasing τ , the term in Eq. (3.7) involving the ground state energy E_0 will dominate. By propagating the wave function forward in time and repeatedly renormalizing the wave function after a number of time steps, the ground state $|\Psi_0\rangle$ can be obtained. Note that for ITP, the trial state $|\Phi\rangle$ must be chosen such that it has a nonzero overlap with the ground state, $c_0 = \langle \Psi_0 | \Phi \rangle \neq 0$.

After obtaining the ground state, the first excited state $|\Psi_1\rangle$ can be constructed by redoing the ITP, and projecting out the ground state at each time step,

$$\Psi(\tau + \Delta\tau) = \mathcal{U}(\tau + \Delta\tau, \tau) \left(1 - |\Psi_0\rangle \langle \Psi_0| \right) |\Psi(\tau)\rangle. \quad (3.8)$$

After sufficiently many iterations, the excited state $|\Psi_1\rangle$ is obtained. In the same way, higher excited states can be obtained.

3.1.2 Complex absorbing potentials

In the numerical treatment of the TDSE, a finite basis must be used, which often involves the truncation of the coordinate space. The continuum WPs that are created during the interaction with a strong laser pulse can travel great distances during the pulse, and if such distances are greater than the simulation boundaries, unphysical reflections can occur, which in turn can disturb the dynamics. It is therefore crucial to make sure that the wave packets do not reach the boundaries of the simulation volume.

One method to achieve this is to add a CAP [77] to the Hamiltonian

$$H(t) \rightarrow H(t) - iV_{\text{CAP}}, \quad (3.9)$$

that can absorb the outgoing continuum WPs without modifying the bound part of the total wave function.

The forms of the CAPs used in this thesis are

$$V_{\text{CAP}} = \begin{cases} 1 - \cos \left[\frac{\pi(|q| - q_{\text{CAP}})}{2(q_{\text{max}} - q_{\text{CAP}})} \right], & \text{for } |q| > q_{\text{CAP}}, \\ 0, & \text{else,} \end{cases} \quad (3.10)$$

and

$$V_{\text{CAP}} = \begin{cases} \eta (|q| - q_{\text{CAP}})^n, & \text{for } |q| > q_{\text{CAP}}, \\ 0, & \text{else,} \end{cases} \quad (3.11)$$

with q the relevant coordinate (either electronic or nuclear), q_{CAP} the start of the CAP region, and q_{max} the grid boundary. The CAP is not a perfect absorber and small unphysical reflections will always occur in the CAP regions. In Eq. (3.11) the prefactor η and the order n are chosen such that the unphysical reflections remain as small as possible. For most of our calculations, we choose $\eta = 0.001$ and $n = 2$.

The effect of the CAP can be made plausible by a simple argument. To first order in Δt , the TEO can be approximated by the split operator

$$\mathcal{U}(t + \Delta t, t) = \exp[-iH(t + \Delta t/2)\Delta t] \exp(-V_{\text{CAP}}\Delta t). \quad (3.12)$$

The action of this operator on the wave function $|\Psi(t)\rangle$ clearly decreases the density in the CAP regions where V_{CAP} is nonzero.

Many methods exist that can be used to remove the outgoing flux in numerical calculations. Such methods include multiplication of the wave function by a mask function at each time step [78] and complex scaling where the coordinates are rotated into the complex plane [79]. Recently, the infinite-range exterior complex

scaling, a method for perfect absorption, was introduced [80]. We have chosen to use CAPs in this thesis due to their straightforward implementation and good absorption properties.

3.1.3 Propagation methods

We now discuss some methods used to propagate the TDSE with the short-time propagator in Eq. (3.4).

The split-operator, fast Fourier transform propagator

We will first discuss the split-operator fast Fourier transform (SO-FFT) method [81]. For illustrative purposes, consider a model atom with one degree of freedom interacting with a laser field, with the Hamiltonian

$$H(x, p, t) = h(p, t) + v(x, t), \quad (3.13)$$

where $h(p, t)$ [$v(x, t)$] is the momentum- [position-] dependent part of the Hamiltonian,

$$h(p, t) = T_e(p) + pA(t), \quad v(x) = V(x), \quad (\text{VG}) \quad (3.14)$$

$$h(p) = T_e(p), \quad v(x, t) = V(x) + F(t)x, \quad (\text{LG}). \quad (3.15)$$

The short-time propagator can be written

$$\mathcal{U}(t + \Delta t, t) = e^{-ih(p,t)\frac{\Delta t}{2}} e^{-iv(x,t)\Delta t} e^{-ih(p,t)\frac{\Delta t}{2}} + \mathcal{O}(\Delta t^3), \quad (3.16)$$

with $\mathcal{O}(\Delta t^3)$ denoting error terms proportional to third and higher orders in Δt . By choosing a time-step much smaller than the characteristic time-scale of the Hamiltonian, the error terms can be neglected.

The $v(x, t)$ is diagonal in coordinate representation, while $h(p, t)$ is diagonal in momentum representation. We proceed by defining N_b equidistant grid points in both representations.

$$x_l = x_0 + l\Delta x, \quad p_m = p_0 + m\Delta p, \quad (l, m = 0, \dots, N_b - 1), \quad (3.17)$$

with $\Delta x = L_e/N_b$, $\Delta p = 2\pi/L_e$, and L_e the length of the spatial grid. The wave function in spatial representation $\Psi(x)$ can be written in terms of the backward Fourier transform (FT) of the momentum wave function $\Phi(p)$:

$$\Psi(x_l, t) = \frac{\Delta p}{\sqrt{2\pi}} \sum_m \Phi(p_m, t) e^{ip_m x_l} \quad (3.18)$$

with the momentum wave function given as the forward FT of the spatial wave function:

$$\Phi(p_m, t) = \frac{\Delta x}{\sqrt{2\pi}} \sum_l \Psi(x_l, t) e^{-ip_m x_l}. \quad (3.19)$$

During each step of the time-propagation, the action of the short-time propagator on the wave function is performed by successively representing the wave function in a basis that diagonalizes the operator in question, as follows:

$$\Psi(x_l, t) \xrightarrow{\text{forward FT}} \Phi(p_m, t) \quad (3.20a)$$

$$\Phi(p_m, t) \xrightarrow{\text{multiplication}} \Phi^{(1)}(p_m, t) \equiv e^{-ih(p_m, t)\frac{\Delta t}{2}} \Phi(p_m, t) \quad (3.20b)$$

$$\Phi^{(1)}(p_m, t) \xrightarrow{\text{backward FT}} \Psi^{(1)}(x_l, t) \quad (3.20c)$$

$$\Psi^{(1)}(x_l, t) \xrightarrow{\text{multiplication}} \Psi^{(2)}(x_l, t) \equiv e^{-iv(x_l, t)\Delta t} \Psi^{(1)}(x_l, t) \quad (3.20d)$$

$$\Psi^{(2)}(x_l, t) \xrightarrow{\text{forward FT}} \Phi^{(2)}(p_m, t) \equiv e^{-ih(p_m, t)\frac{\Delta t}{2}} \Phi^{(2)}(p_m, t) \quad (3.20e)$$

$$\Phi^{(2)}(p_m, t) \xrightarrow{\text{backward FT}} \Psi(x_l, t + \Delta t). \quad (3.20f)$$

In the SO-FFT method, most of computational effort is in the discrete FT that has to be performed multiple times for each time step. With the Cooley-Tukey fast fourier transformation (FFT) algorithm the scaling of each transform with respect to the number of grid points is in the order of $N_b \log(N_b)$. For d degrees of freedom, d -dimensional FFTs should be performed, with each transform scaling as $(N_{b,1} \cdots N_{b,d}) \log(N_{b,1} \cdots N_{b,d})$, where $N_{b,1}, \dots, N_{b,d}$ are the number of discretization points for each degree of freedom. We perform the FFT using the Fastest Fourier Transform in the West library¹.

Short-iterative Lanczos propagator

In the short-iterative Lanczos (SIL) method [82] for Hermitian Hamiltonians $H(t)$, a Krylov subspace \mathcal{L} of dimension $L + 1$ is defined at each time step, spanned by the set of vectors $\{H^k |\Psi(t)\rangle\}_{k=0}^L$. For notational convenience, we will henceforth not always explicitly write the dependency on t . An orthonormal basis $\{|Q_k\rangle\}_{k=0}^L$ for \mathcal{L} is found by the Gram-Schmidt orthogonalization procedure,

$$\begin{aligned} |Q_0\rangle &= |\Psi\rangle, \\ H|Q_j\rangle &= \beta_{j-1}|Q_{j-1}\rangle + \alpha_j|Q_j\rangle + \beta_j|Q_{j+1}\rangle, \end{aligned} \quad (3.21)$$

with

$$\beta_{j-1} = \langle Q_j | H | Q_{j-1} \rangle, \quad \alpha_j = \langle Q_j | H | Q_j \rangle. \quad (3.22)$$

¹<http://www.fftw.org>

We approximate the Hamiltonian in this basis,

$$H = \sum_{i=0}^L \sum_{j=0}^L |Q_i\rangle [\mathbf{H}_{\mathcal{L}}]_{ij} \langle Q_j|, \quad (3.23)$$

with the tridiagonal Krylov Hamiltonian

$$\mathbf{H}_{\mathcal{L}} = \begin{bmatrix} \alpha_0 & \beta_0 & & & \\ \beta_0 & \alpha_1 & \ddots & & \\ & \ddots & \ddots & \beta_{L-1} & \\ & & \beta_{L-1} & \alpha_L & \end{bmatrix}. \quad (3.24)$$

Now the short-time propagator in Eq. (3.4) becomes

$$\mathcal{U}(t + \Delta t, t) \approx \sum_{i=0}^L \sum_{j=0}^L |Q_i\rangle [\exp(-i\mathbf{H}_{\mathcal{L}}\Delta t)]_{ij} \langle Q_j|. \quad (3.25)$$

After diagonalization of $\mathbf{H}_{\mathcal{L}}$,

$$\mathbf{H}_{\mathcal{L}} = \mathbf{S} \text{diag}(\lambda_0, \dots, \lambda_L) \mathbf{S}^\dagger, \quad (3.26)$$

the expansion coefficients c_i of the propagated wave function in the Krylov subspace can be evaluated,

$$\begin{aligned} |\Psi(t + \Delta t)\rangle &= U(t + \Delta t, t) |\Psi(t)\rangle \approx \sum_{k=0}^L c_k |Q_k\rangle \\ c_k &= \sum_j^L [\mathbf{S}]_{kj} \exp(-i\lambda_j\Delta t) [\mathbf{S}^{-1}]_{j0}. \end{aligned} \quad (3.27)$$

In this thesis, the Krylov dimension is ranging from 8 to 12. For non-Hermitian Hamiltonians, e.g. when CAPs are included, a similar method exist, called the short-iterative Arnoldi (SIA) method [78], where the Krylov Hamiltonian becomes a Hessenberg matrix. Both methods are used in this thesis.

Note that the SIL and SIA propagation methods are quite general, and are applicable to all problems where the TDSE can be written in matrix form. The computational effort is mainly in the L evaluations of the matrix-vector products at each time step. Each matrix-vector product scales as $\mathcal{O}(L^2)$ for a filled matrix, $\mathcal{O}(L)$ for a diagonal matrix, and inbetween these scalings for a sparse matrix.

3.2 Numerical solution of the surface model

We now discuss the method used to propagate the BO surface model described in Section 2.2 to simulate strong-field physics without the electronic continua. Our strategy for propagation is to employ the SO-FFT method. The TDSE in Eq. (2.32) with $\mathbf{H}^{(3)}$ neglected can be written as

$$i \frac{\partial}{\partial t} \mathbf{G}(R, t) = \left[\mathbf{T}_N + \mathbf{M}(t) + \mathbf{H}^{(2)}(t) \right] \mathbf{G}(R, t), \quad (3.28)$$

with

$$\begin{aligned} [\mathbf{T}_N]_{ij} &= T_N \delta_{ij} \\ [\mathbf{M}(t)]_{ij} &= \{E_{el,i}(R) - i[\Gamma_i(R)/2 + V_{CAP}] + V_{I,N}(R, t)\} \delta_{ij} \\ [\mathbf{H}^{(2)}(t)]_{ij} &= \beta^{\text{LG}} [\mathbf{D}(R)]_{ij} F(t). \end{aligned} \quad (3.29)$$

The short-time propagator is expressed as follows:

$$\begin{aligned} \mathbf{u}(t + \Delta t, t) &= \exp \left(-i \mathbf{T}_N \frac{\Delta t}{2} \right) \exp \left(-i \mathbf{M}(t) \frac{\Delta t}{2} \right) \\ &\quad \times \exp \left[-i \mathbf{H}^{(2)}(t) \Delta t \right] \\ &\quad \times \exp \left(-i \mathbf{M}(t) \frac{\Delta t}{2} \right) \exp \left(-i \mathbf{T}_N \frac{\Delta t}{2} \right). \end{aligned} \quad (3.30)$$

In the right hand side of Eq. (3.30), the second and fourth factors are diagonal in the nuclear position space R , while the first and the fifth factors are diagonal in nuclear momentum space, which makes them easy to evaluate using the SO-FFT method. The third factor, while being diagonal in position space, is not diagonal in the BO basis $|\phi_{el,i}\rangle$. Hence to treat matrix exponential in the third factor of Eq. (3.30), $\mathbf{D}(R)$ is diagonalized for all R ,

$$\mathbf{C}^\dagger(R) \mathbf{D}(R) \mathbf{C}(R) = \bar{\mathbf{D}}(R), \quad (3.31)$$

with $\bar{\mathbf{D}}(R)$ diagonal matrices. The diagonalization is performed before the time propagation, with \mathbf{C} and $\bar{\mathbf{D}}(R)$ stored in memory. The memory requirement is completely manageable, as it scales as $\mathcal{O}(N_{BO} N_N)$, with N_N the number of discretization points for R . The third factor in Eq. (3.30) is then rewritten,

$$\begin{aligned} \exp \left[-i \mathbf{H}^{(2)}(t) \Delta t \right] &= \exp \left[-i \beta^{\text{LG}} \mathbf{D}(R) F(t) \Delta t \right] \\ &= \mathbf{C}(R) \exp \left[-i \beta^{\text{LG}} \bar{\mathbf{D}}(R) F(t) \Delta t \right] \mathbf{C}^\dagger(R). \end{aligned} \quad (3.32)$$

Now the SO-FFT propagation method described in the previous section is applicable, by successively transforming the wave function into a basis where the operator in question is diagonal, and performing the operator operation by multiplication.

3.3 Numerical solution of 1D H_2^+

The 1D H_2^+ model was introduced in Section 2.3 for the investigation of breakup processes involving both the electronic and nuclear continua. We propagate the TDSE using the SO-FFT method. The Hamiltonian for the problem in Eq. (2.37) is

$$H(x, R, p, k, t) = h(p, k, t) + v(x, R, t), \quad (3.33)$$

where p (k) is the electronic (nuclear) momentum operator, and

$$h(p, k, t) = \begin{cases} T_e(p) + T_N(k) + V_L(p, k, t), & \text{(VG)} \\ T_e(p) + T_N(k), & \text{(LG)} \end{cases} \quad (3.34)$$

$$v(x, R, t) = \begin{cases} V_{eN}(x, R) + V_N(R), & \text{(VG)} \\ V_{eN}(x, R) + V_N(R) + V_L(x, t), & \text{(LG)}, \end{cases} \quad (3.35)$$

with the individual terms given by Eq. (2.38). The short-time propagator is then written as in Eq. (3.16),

$$\mathcal{U}(t + \Delta t, t) = e^{-ih(p,k,t)\frac{\Delta t}{2}} e^{-v(p,k,t)\Delta t} e^{-ih(p,k,t)\frac{\Delta t}{2}} + \mathcal{O}(\Delta t^3). \quad (3.36)$$

The discretization grids are defined,

$$\begin{aligned} x_l &= x_0 + l\Delta x, & p_m &= p_0 + m\Delta p, & (l, m &= 0, \dots, N_{b,e} - 1) \\ R_j &= R_0 + j\Delta R, & k_n &= k_0 + n\Delta k, & (j, n &= 0, \dots, N_{b,N} - 1) \end{aligned} \quad (3.37)$$

with $\Delta x = L_e/N_{b,e}$, $\Delta R = L_N/N_{b,N}$, $\Delta p = 2\pi/L_e$, $\Delta k = 2\pi/L_N$, and L_e and L_N the length of the electronic and nuclear coordinate grids. The SO-FFT propagation scheme described in Eq. (3.20) can then be performed. In the numerical propagation for 1D H_2^+ , we use the time-step $\Delta t = 0.005$.

3.4 Numerical solution of the TD-GASCI method

The TD-GASCI method [67, 68] for solving the TDSE for a many-electron system in FNA was introduced in Section 2.4. The method was first implemented by Hochstuhl et al. in Ref. [67], while the version discussed in this thesis has been implemented by Bauch et al. [68]. Larsson et al. [83] implemented the prolate spheroidal basis set, while the Dyson orbitals, WFAT, and flux methods in the TD-GASCI are the new implementations, which will be discussed at a later stage in this thesis.

In this section, we briefly discuss some important points in the core implementation of TD-GASCI, for more details, see Refs. [67, 68, 83].

3.4.1 The primitive basis

The primitive single-particle basis f_i discussed in Subsection 2.4.4 should be chosen such that it is computationally feasible and accurate for both the bound and the continuum parts of the wave function. Standard Gaussian basis sets from quantum chemistry can accurately describe the bound states [76], but is unable to describe the continuum due to the fast decaying asymptotic tails of the Gaussian functions. The two-center character of diatomics also makes the expansion in spherical harmonics unfeasible due to the high angular momentum states required.

Working with prolate spheroidal coordinates, combined with finite-element discrete variable representation (FE-DVR) basis, overcomes some of these obstacles. In DVR [84] and FE-DVR methods [85], analytic basis functions localized about discrete coordinate values are used. They can be constructed using Gaussian quadrature rules, and integral evaluations are with Gaussian quadrature accuracy. Kinetic energy matrix elements are known analytically, while potential energy matrix elements are diagonal, making the evaluation and storage of the matrix elements high efficient. The FE-DVR approach is a combination of a FE method with a DVR basis. The total spatial region is divided into finite elements, each element with its own set of DVR basis functions. This allows for an good adaption of the basis to a physical problem, as we can specify the position of the elements and the number of the DVR functions in each element. For example in the problem of ionization, a FE element containing a large number of DVR functions can be used near the nucleus to accurately represent the bound part of the wave function, while FE's with less dense quadrature points far from the bound region can be used to describe the continuum. See Appendix A for the construction and properties of the FE-DVR basis set. For more details, see also [85].

We briefly discuss the prolate spheroidal basis set [86–88] used in the TD-GASCI [83]. Consider the two nuclei placed at \mathbf{R}_A and \mathbf{R}_B , with $R = |\mathbf{R}| = 2a$ the internuclear distance, and $r_A = |\mathbf{r} - \mathbf{R}_A|$ and $r_B = |\mathbf{r} - \mathbf{R}_B|$ the distances to the nuclei. The prolate spheroidal coordinates are defined by [89]

$$\zeta = \frac{r_A + r_B}{R}, \quad \zeta \in [1, \infty), \quad (3.38a)$$

$$\mu = \frac{r_A - r_B}{R}, \quad \mu \in [-1, 1], \quad (3.38b)$$

$$\varphi = \arctan\left(\frac{y}{x}\right), \quad \varphi \in [0, 2\pi]. \quad (3.38c)$$

The relation to some other relevant coordinate systems are given in Appendix D.

The single-particle primitive basis are chosen as

$$f_{ia}^m(\zeta, \mu, \phi) = \sqrt{\frac{1}{a^3(\zeta_i^2 - \mu_a^2)}} \theta_i^m(\zeta) \theta_a^m(\mu) \frac{\exp(im\phi)}{\sqrt{2\pi}}, \quad (3.39)$$

where the factor $[a^3(\zeta_i^2 - \mu_a^2)]^{-1/2}$ is introduced to counteract the prolate spheroidal volume element $dV = a^3(\zeta^2 - \mu^2)d\zeta d\mu d\phi$, and the Gauss-Lobatto DVR basis sets [Appendix A]

$$\theta_n^m(s) = \frac{1}{\sqrt{\omega_n}} \prod_{i \neq n}^{N_{b,s}} \frac{s - s_i}{s_n - s_i} \times \begin{cases} 1, & m \text{ even} \\ \sqrt{\frac{s^2-1}{s_n^2-1}}, & m \text{ odd,} \end{cases} \quad (3.40)$$

are used for the ζ and μ coordinates, with $s = \zeta$ or $s = \mu$ in Eq. (3.40), and $N_{b,s}$ the number of basis functions for coordinate s . The extra factor for odd m in Eq. (3.40) is to treat the non-polynomial behavior of the wave function at the points $\zeta = 1$ and $|\mu| = 1$ [86]. For the η coordinates, a Gauss-Legendre DVR is used, with the end points not chosen as quadrature points. For the ζ coordinates, a FE-DVR basis is used, where the Gauss-Radau quadrature is employed for the first element with $\zeta = 1$ excluded, and Gauss-Lobatto quadrature is used for the rest of the elements [see Appendix A]. Using the primitive basis in Eq. (3.18) and the mentioned quadrature rules, the matrix elements for the kinetic energy operator and potential energy operators can be evaluated [83]:

$$\langle f_{ia}^m | T_e | f_{jb}^{m'} \rangle \propto a^{-2} \delta_{mm'} (A_{ab}^m \delta_{ij} + B_{ij}^m \delta_{ab} + C_{ia}^m \delta_{ij} \delta_{ab}) \quad (3.41a)$$

$$\langle f_{ia}^m | V_{eN} | f_{jb}^{m'} \rangle \propto a^{-1} \delta_{mm'} \delta_{ij} \delta_{ab} \quad (3.41b)$$

$$\langle f_{ia}^m | z | f_{jb}^{m'} \rangle = a \delta_{mm'} \delta_{ij} \delta_{ab} \zeta_i \mu_a \quad (3.41c)$$

$$\langle f_{i_1 a_1}^{m_1} f_{i_2 a_2}^{m_2} | V_{ee} | f_{j_1 b_1}^{m'_1} f_{j_2 b_2}^{m'_2} \rangle = a^{-1} \delta_{m_1 - m'_1, m'_2 - m_2} \delta_{a_1 b_1} \delta_{a_2 b_2} \delta_{i_1 j_1} \delta_{i_2 j_2}, \quad (3.41d)$$

where A_{ab}^m , B_{ij}^m , and C_{ia}^m are known analytically. The matrix elements are seen to be highly sparse, and especially scaling of the two-electron integrals in Eq. (3.41d) are drastically reduced from $\mathcal{O}(N_b^4)$ to $\mathcal{O}(N_{b,\zeta}^2 N_{b,\mu}^2 N_{b,\phi})$.

3.4.2 The orbital basis - partially rotated basis

Having defined the primitive basis, the spatial-orbital basis should be constructed. The orbitals should correctly describe the bound structure near the nucleus, as well as accurately describe the electron continuum. A space-partition concept is used for this purpose, with the basis split into two regions: an inner region with $\zeta < \zeta_s$ and an outer region with $\zeta \geq \zeta_s$, with ζ_s coinciding with a FE-DVR

boundary. The spatial orbitals are chosen as

$$\phi_i(\mathbf{r}) = \begin{cases} \sum_j c_{ij} f_j(\mathbf{r}), & \text{if } \zeta < \zeta_s, \\ f_i(\mathbf{r}), & \text{if } \zeta \geq \zeta_s, \end{cases} \quad (3.42)$$

where we have used a common index i to denote the three DVR indices in f_{ia}^m . In the inner region, the first $N/2$ spatial orbitals are the occupied HF orbitals, with c_{ij} obtained from the HF procedure sketched in Subsection 2.4.3. The virtual HF orbitals are often too diffuse to be useful in truncated CI. Instead, the inner region virtual orbitals are chosen as the virtual orbitals of the $(N - 2)$ -electron HF problem (with nuclear charges Z_1 and Z_2 unchanged), orthogonalized to the occupied N -electron occupied orbitals [68]. This choice is based on intuition of the photoionization problem: when one electron is ionized, another electron near the nucleus feels the effective potential created by the $N - 2$ remaining electrons. In the outer region, the primitive-basis functions are used as the spatial orbitals, to better describe the continuum. Due to the properties of the FE-DVR basis, the outer-region orbitals are orthogonal to the inner-region orbitals, and the orbital basis defined in Eq. (3.42) is an orthonormal basis. All the choices made here are to construct an orthonormal orbital basis that is able to describe the single-ionization physics as good as possible, with a minimal primitive basis.

3.4.3 Solution outline

A TD-GASCI calculation proceeds as follows. First, the primitive basis and the corresponding Hamiltonian matrix elements are set up in the inner region. The HF calculations are then performed to obtain the expansion coefficients c_{ij} for the inner-region orbitals. Afterwards, the primitive basis and corresponding Hamiltonian matrix elements are set up over the total spatial region. Subsequently, the matrix elements in Eqs. (2.52) and (2.53) are set up in the spatial orbital basis $\phi_i(\mathbf{r})$. The CI-matrix is constructed using Slater-Condon rules and the initial ground state is obtained by ITP using the SIL method in Subsection 3.1.1. Finally the TD-GASCI can be propagated in real time using the SIL or SIA methods. The efficient extraction of continuum observables is discussed in the next chapter.

CHAPTER 4

EXTRACTION OF SPECTRA FROM THE TDSE

After the introduction of different methods that can be used to simulate strong-field molecular breakup in Chapter 2 and Chapter 3, the attention now turns toward the efficient extraction of continuum observables from such simulations. Standard methods of obtaining PMS and PES from numerical calculations include the projection on plane waves [90, 91], the projection on scattering states [75, 92], and the usage of flux methods [71–73, 93]. In the first method, huge simulation volumes are required, as it must be ensured that after the end of the pulse, the scattered parts of the wave packet are well-separated from its bound part and not reflected from the box boundaries. In the second method, the simulation volume can be reduced somewhat compared to the first method due to the orthogonality between the scattering and bound states, and the projection can be performed immediately at the end of the pulse. However, the construction of scattering states is tedious and constitutes a numerical challenge in itself. For the flux methods, absorbers are placed at the boundaries of the simulation volume to remove the outgoing flux, and spectra are obtained by monitoring the flux going through surfaces placed at distances smaller than the absorber regions. In this way the simulation volume can be significantly reduced. One of these flux methods is the time-dependent surface flux (tSURFF) method, which was first introduced for the extraction of spectra in strong-field ionization of atoms [73, 94]. In this chapter, this method is generalized to treat molecular breakup, as well as single-ionization of many-electron systems.

4.1 Differential spectra for 1D H_2^+

For H_2^+ interacting with a laser pulse, there are two breakup pathways:

- The DI channel $H_2^+ \rightarrow p + p + e$, where the molecule completely breaks up into two protons and one electron. The observable of interest is the JES that shows the energy sharing between the protons and the electron.
- The dissociation channel $H_2^+ \rightarrow H + p$, where the molecule dissociates into a proton and a hydrogen atom in a given state (channel). The relevant observables are the channel specific NKER spectra that show how the nuclear kinetic energies are shared between the different dissociation channels belonging to different BO surfaces.

The tSURFF method for DI and dissociation will now be outlined here for the specific case of our model H_2^+ molecule.

To identify the different channels and the corresponding observables, we partition the total coordinate space into four regions as shown in Fig. 4.1. Each region corresponds to a reaction channel. By monitoring the flux going through the surfaces at $x = x_s$ and $R = R_s$, the JES for DI and the channel-specific NKER for dissociation can be constructed. To proceed formally, we define the projection operators

$$\theta_e = \int dx \theta(|x| - x_s) |x\rangle \langle x|, \quad (4.1a)$$

$$\theta_N = \int dR \theta(R - R_s) |R\rangle \langle R|, \quad (4.1b)$$

where x_s and R_s are coordinates of the surfaces beyond which the Coulomb interactions V_{eN} and V_N are neglected, respectively, and $\theta(x)$ is the Heaviside step function. The total wavefunction is partitioned into the four parts belonging to the different spatial domains of Fig. 4.1

$$|\Psi(t)\rangle = |\Psi_B(t)\rangle + |\Psi_D(t)\rangle + |\Psi_I(t)\rangle + |\Psi_{DI}(t)\rangle, \quad (4.2)$$

with $|\Psi_B(t)\rangle = (1 - \theta_e)(1 - \theta_N) |\Psi(t)\rangle$, $|\Psi_D(t)\rangle = (1 - \theta_e)\theta_N |\Psi(t)\rangle$, $|\Psi_I(t)\rangle = \theta_e(1 - \theta_N) |\Psi(t)\rangle$, and $|\Psi_{DI}(t)\rangle = \theta_e\theta_N |\Psi(t)\rangle$. For sufficiently large times after the end of the laser pulse $T > T_{\text{pulse}}$, the dissociation and DI WPs will have moved into their specific spatial regions such that $|\Psi_B(T)\rangle$ contains the bound part, $|\Psi_D(T)\rangle$ contains the dissociative part, and $|\Psi_{DI}(T)\rangle$ contains the DI part. At time T , the wave packet in the spatial region corresponding to ionization $|\Psi_I(T)\rangle = \theta_e(1 - \theta_N) |\Psi(T)\rangle = 0$, as all the ionized part will have moved into the DI region since the nuclei do not support bound states after the removal of the electron.

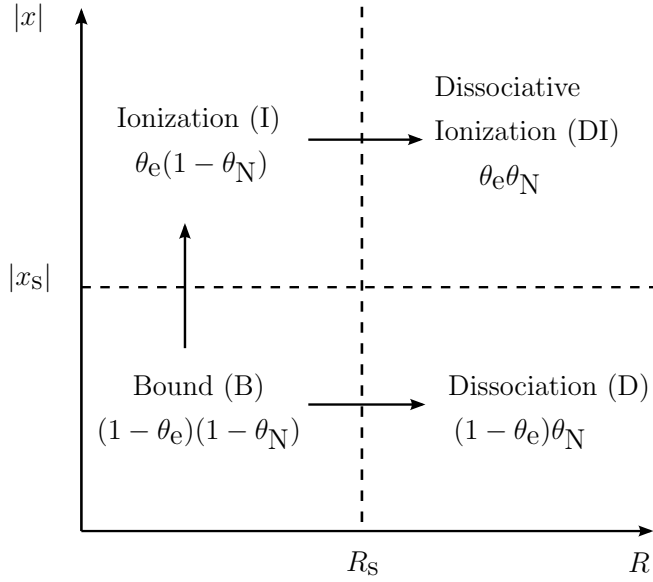


Figure 4.1: Sketch showing the four spatial domains used to analyse the WPs. The dashed line at $x = x_s$ is a boundary surface beyond which the electron-nuclear interaction V_{eN} is neglected in the DI channel, while the dashed line at $R = R_s$ is a boundary surface beyond which the nuclear repulsion V_N is neglected. In the tSURFF method, the flux passing through these surfaces are monitored and used to construct the differential probability amplitudes. The projection operators of different spatial domains are also indicated.

4.1.1 tSURFF for dissociative ionization

The TDSE projected on the spatial region describing the DI channel reads

$$i\partial_t |\Psi_{DI}(t)\rangle = H_{DI}(t) |\Psi(t)\rangle, \quad (4.3)$$

with $H_{DI}(t) = \theta_e \theta_N H(t) \approx T_e + T_N + V_L(t)$. Notice that $|\Psi(t)\rangle$, and not $|\Psi_{DI}(t)\rangle$, appears on the right-hand-side of Eq. (4.3), due to the fact that $H(t)$ does not commute with $\theta_e \theta_N$.

The TDSE for $H_{DI}(t)$ is separable in the electronic and nuclear degrees of freedom, with the electronic TDSE given by

$$i\partial_t |\phi(t)\rangle = (T_e + V_L(t)) |\phi(t)\rangle, \quad (4.4)$$

and the nuclear TDSE given by

$$i\partial_t |\chi(t)\rangle = T_N |\chi(t)\rangle. \quad (4.5)$$

A complete set of the solutions in position space is formed by the Volkov waves $\phi_p^V(x, t) = \langle x | \phi_p^V(t) \rangle$ with momentum p for the electron [see Subsection 2.1.4] and

plane waves $\chi_k(R, t) = \langle R | \chi_k(t) \rangle$ with momentum k for the nuclei. The explicit forms of these wave functions, with normalizations $\delta(k - k') = \langle \chi_k(t) | \chi_{k'}(t) \rangle$ and $\delta(p - p') = \langle \phi_p^V(t) | \phi_{p'}^V(t) \rangle$, are

$$\phi_p^V(x, t) = (2\pi)^{-1/2} \exp \left[i \left(px - \frac{p^2 t}{2\mu} - \frac{p}{\mu} \int^t A(t') dt' \right) \right], \quad (4.6)$$

$$\chi_k(R, t) = (2\pi)^{-1/2} \exp \left[i \left(kR - \frac{k^2 t}{m_p} \right) \right]. \quad (4.7)$$

The WP $|\Psi_{DI}(t)\rangle$ is expanded in the direct product basis of Volkov and plane waves

$$|\Psi_{DI}(t)\rangle = \theta_e \theta_N |\Psi(t)\rangle = \int dp \int dk b_{p,k}(t) |\phi_p^V(t)\rangle |\chi_k(t)\rangle, \quad (4.8)$$

where

$$b_{p,k}(T) = \langle \phi_p^V(t) | \langle \chi_k(t) | \theta_e \theta_N |\Psi(t)\rangle \quad (4.9)$$

is the differential probability amplitude for measuring p and k . The joint momentum spectrum (JMS) and JES are given by

$$\frac{\partial^2 P}{\partial p \partial k} = |b_{p,k}(T)|^2, \quad (4.10a)$$

$$\frac{\partial^2 P}{\partial E_e \partial E_N} = \sum_{\text{sgn}(p)} \frac{m_p \mu}{2pk} |b_{p,k}(T)|^2, \quad (4.10b)$$

with $E_N = k^2/m_p$, $E_e = p^2/2\mu$, and the summation over $\text{sgn}(p)$ referring to the summation of $\pm p$ corresponding to the same E_e .

The expression for $b_{p,k}(T)$ can be rewritten using Eqs. (4.3)-(4.5) and the fundamental theorem of calculus. The result reads

$$b_{p,k}(T) = b_{p,k}^e(T) + b_{p,k}^N(T) \quad (4.11)$$

with

$$b_{p,k}^e(T) = i \int_{-\infty}^T dt \langle \phi_p^V(t) | [T_e + V_L(t), \theta_e] \langle \chi_k(t) | \theta_N |\Psi(t)\rangle, \quad (4.12)$$

and

$$b_{p,k}^N(T) = i \int_{-\infty}^T dt \langle \chi_k(t) | [T_N, \theta_N] \langle \phi_p^V(t) | \theta_e |\Psi(t)\rangle. \quad (4.13)$$

In Eqs. (4.12)-(4.13), the commutators vanish everywhere except at the discontinuity of the step functions. The probability amplitudes can thus be obtained by integrating the time-dependent surface flux. In Fig. 4.1, $b_{p,k}^e(T)$ is the amplitude corresponding to the flux going from the dissociation region into the DI region,

while $b_{p,k}^N(T)$ is the amplitude corresponding to the flux going from the ionization region into the DI region. The two amplitudes must be added coherently to obtain the total amplitude for DI. It is, however, possible to choose R_s sufficiently large so that all the flux going into the DI region in Fig. 4.1 originate from the ionization region, and therefore we can set $b_{p,k}^e(T) = 0$. The commutator in the expression (4.13) for $b_{p,k}^N(T)$ can be calculated explicitly

$$[T_N, \theta_N] = -\frac{1}{m_p} \int dR |R\rangle \left[\delta^{(1)}(R - R_s) + 2\delta(R - R_s) \frac{\partial}{\partial R} \right] \langle R|, \quad (4.14)$$

where δ and $\delta^{(1)}$ are the Dirac delta function and its first derivative, respectively. After inserting Eq. (4.14) into Eq. (4.13), evaluating the resulting integral and collecting terms in Eq. (4.11), we obtain

$$b_{p,k}(T) = \frac{1}{m_p} \int_{-\infty}^T dt \chi_k^*(R_s, t) \left[k - i \frac{\partial}{\partial R} \right] \langle \phi_p^V(t) | \theta_e | \Psi(t) \rangle \Big|_{R_s}. \quad (4.15)$$

To calculate the amplitude of Eq. (4.15), the matrix element $\langle \phi_p^V(t) | \theta_e | \Psi(t) \rangle$ must be evaluated at R_s . Direct projection of $\theta_e | \Psi(t) \rangle$ on the Volkov waves $|\chi_p(t)\rangle$ is not an option as the electronic CAP will absorb part of the wavefunction at $x > x_{\text{CAP}} > x_s$. To circumvent this problem we expand $\langle \phi_p^V(t) | \theta_e | \Psi(t) \rangle$ in an arbitrary time-independent basis $\zeta_m(R)$

$$\langle \phi_p^V(t) | \theta_e | \Psi(t) \rangle = \sum_m a_{p,m}(t) |\zeta_m\rangle \quad (4.16)$$

with $a_{p,m}(t) = \langle \zeta_m | \langle \phi_p^V(t) | \theta_e | \Psi(t) \rangle$. In our calculations we use a sine basis for ζ_m . By taking the time derivative of $a_{p,m}(t)$, it can be shown that $a_{p,m}(t)$ satisfies

$$\frac{d}{dt} a_{p,m}(t) = -i \sum_{m'} \langle \zeta_m | T_N | \zeta_{m'} \rangle a_{p,m'}(t) + f_{p,m}^+(t) + f_{p,m}^-(t) \quad (4.17)$$

with

$$f_{p,m}^+(t) = \phi_p^{V*}(x_s, t) \left[\left(\frac{p}{2\mu} + A(t) \right) - \frac{i}{2\mu} \frac{\partial}{\partial x} \right] \langle \zeta_m | \Psi(t) \rangle \Big|_{x_s} \quad (4.18)$$

and

$$f_{p,m}^-(t) = -\phi_p^{V*}(-x_s, t) \left[\left(\frac{p}{2\mu} + A(t) \right) - \frac{i}{2\mu} \frac{\partial}{\partial x} \right] \langle \zeta_m | \Psi(t) \rangle \Big|_{-x_s}. \quad (4.19)$$

The terms $f_{p,m}^+(t)$ and $f_{p,m}^-(t)$ can be interpreted as flux terms, counting the flux going through the surfaces at $x = x_s$ and at $x = -x_s$, respectively. In our

calculations we solve Eq. (4.17) using a fourth-order Runge-Kutta method. The coefficients $a_{p,m}(t)$ give us information on the WP even in regions where the CAP is active ($x > x_{\text{CAP}} > x_s$), as seen in Eq. (4.16). When describing laser ionization, one of the two terms in $f_{p,m}(t)$ will usually be negligible and can be ignored. For example, if p is positive, f^- will be zero since in this case there is no incoming wave at $x = -x_s$.

Inserting Eq. (4.16) into Eq. (4.15), we obtain the final expression for $b_{p,k}(T)$ determining the JES through Eq. (4.10b).

$$b_{p,k}(T) = \frac{1}{m_p} \sum_m \left[k - i \frac{\partial}{\partial R} \right] \zeta_m(R) \Big|_{R_s} \int_{-\infty}^T dt \chi_k^*(R_s, t) a_{p,m}(t). \quad (4.20)$$

Numerical demonstrations – JES for DI

We demonstrate the tSURFF method for DI by considering an $A(t)$ pulse in VG with sine squared envelope, $N_c = 10$, $I = 8.8 \times 10^{13}$ W/cm², and two different frequencies, $\lambda = 400$ nm and $\lambda = 800$ nm. The simulation volume is chosen as $|x| \leq 200$ and $|R| \leq 60$, the grid spacings chosen as $x = 0.781$ and $R = 0.078$, the CAP placed at $x_{\text{CAP}} = 105$ and $R_{\text{CAP}} = 26$, and the tSURFF surfaces placed at $x_s = 100$ and $R_s = 25$. The converged JES obtained for $T = 1200$ are shown in Fig. 4.2. For both wavelengths, the energy conservations predicted in Ref. [75]

$$E_N + E_e = E_0 + n\omega - U_p, \quad (4.21)$$

corresponding to multi-photon absorptions, are satisfied (white diagonal lines in Fig. 4.2). The size of the simulation volume used should be compared with the sizes of the volumes used by other methods. Two other methods have been used to determine the JES based on wave packet propagation. In one work [75], a projection on approximate scattering states was performed with the simulation volume $|x| \leq 1500$. In another work [21], a resolvent technique was used with $|x| \leq 3000$. Both these values significantly exceed the simulation volume used here, which clearly demonstrates the advantage of the present tSURFF method. Our obtained result of the JES for 400 nm is the same as the one presented in Ref. [75]. In Fig. 4.2, for both wavelengths, there are structures not explained by the energy conservations in Eq. (4.21). We will explain these interesting structures in Chapter. 7.

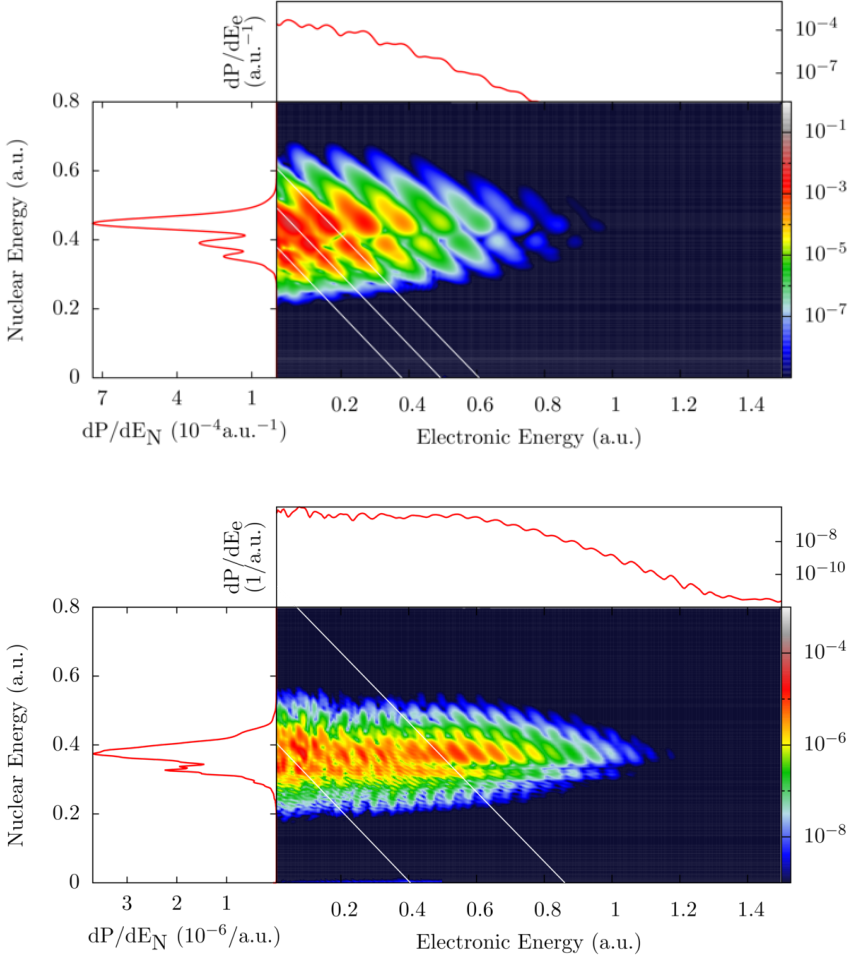


Figure 4.2: JES for DI of H_2^+ , for a sine-squared pulse with parameters $N_c = 10$ and $I = 8.8 \times 10^{13} \text{ W/cm}^2$. Upper figure: $\lambda = 400 \text{ nm}$, lower figure: $\lambda = 800 \text{ nm}$. The top and left side panels are the ATI and NKER spectra, respectively. The energy conservation corresponding to n -photon absorption satisfying $E_N + E_e = E_0 + n\omega - U_p$ are the white lines. The two lines in the upper figure correspond to $n = 9$ and $n = 10$, while for the bottom figure they correspond to $n = 21$ and $n = 29$.

4.1.2 tSURFF for Dissociation

Consider now the dissociation process $H_2^+ \rightarrow H + p$. The projected TDSE on the region describing dissociation without ionization reads (see Fig. 4.1)

$$i\partial_t |\Psi_D(t)\rangle = H_D(t) |\Psi(t)\rangle, \quad (4.22)$$

where we have defined the projected Hamiltonian $H_D(t) = (1 - \theta_e)\theta_N H(t)$. To obtain the dissociation-channel-specific NKER spectrum we define the adiabatic Born-Oppenheimer (BO) basis states $|\phi_{el,i}\rangle$ as the solutions to the electronic time-independent Schrödinger equation with parametric dependence on R

$$\left(T_e + V_{eN} + V_N\right) |\phi_{el,i}\rangle = E_{el,i}(R) |\phi_{el,i}\rangle, \quad (4.23)$$

where $E_{el,i}(R)$ is the i 'th electronic potential energy surface in the BO approximation. To ease notation we do not explicitly include the parametric dependence on R in the BO-states. The WP $\Psi_D(x, R, t)$ is expanded in the BO basis as

$$\begin{aligned} |\Psi_D(t)\rangle &= (1 - \theta_e)\theta_N |\Psi(t)\rangle \\ &= \int dk \sum_i c_{i,k}(t) |\chi_k(t)\rangle |\phi_{el,i}(t)\rangle, \end{aligned} \quad (4.24)$$

where $|\chi_k(t)\rangle$ is a plane wave with momentum k given by Eq. (4.7), $|\phi_{el,i}(t)\rangle = |\phi_{el,i}\rangle e^{-iE_{el,i}(R)t}$ and

$$c_{i,k}(t) = \langle \chi_k(t) | \langle \phi_{el,i}(t) | (1 - \theta_e)\theta_N |\Psi(t)\rangle. \quad (4.25)$$

In Eq. (4.24), all the trivial time-dependence is included in $|\phi_{el,i}(t)\rangle$ and $|\chi_k(t)\rangle$, while the non-trivial time dependence due to the external field and flux going from the bound region into the dissociation region of Fig. 4.1 is included in the expansion coefficients $c_{i,k}(t)$. At time $T > T_{\text{pulse}}$, when all the dissociative parts of the WP have moved into the dissociative region, $c_{i,k}(T)$ describes the differential probability amplitude for the electron to be in the bound state i and the nuclei to have momentum k .

The expression for $c_{i,k}(T)$ can be written in terms of a time integral:

$$c_{i,k}(T) = c_{i,k}^N(T) + c_{i,k}^e(T) + c_{i,k}^L(T), \quad (4.26)$$

with

$$c_{i,k}^N(T) = i \int_{-\infty}^T dt \langle \chi_k(t) | [T_N, \theta_N] \langle \phi_{el,i}(t) | (1 - \theta_e) |\Psi(t)\rangle, \quad (4.27)$$

$$c_{i,k}^e(T) = i \int_{-\infty}^T dt \langle \phi_{el,i}(t) | [T_e + V_{eN} + V_N, (1 - \theta_e)] \langle \chi_k(t) | \theta_N |\Psi(t)\rangle, \quad (4.28)$$

$$c_{i,k}^L(T) = -i \int_{-\infty}^T dt \langle \phi_{el,i}(t) | \langle \chi_k(t) | (1 - \theta_e)\theta_N V_L(t) |\Psi(t)\rangle. \quad (4.29)$$

In the derivation of Eq. (4.27), it is assumed that the action of the nuclear kinetic energy operator on the electronic BO-states is neglected. This is in accordance with the BO approximation wherein the first- and second-order derivatives of the electronic state with respect to R are neglected.

In Fig. 4.1, The amplitude $c_{i,k}^N(T)$ corresponds to the flux going from the bound region into the dissociation region through the surface at $R = R_s$, while $c_{i,k}^e(T)$ corresponds to the flux going through the surfaces at $x = \pm x_s$. The amplitude $c_{i,k}^e$ can thus be neglected if the dissociative WP never reaches the surface $x = \pm x_s$ at time T . In the pure dissociation process, the electron is localized near one of the protons, i.e., along the lines $x = \pm R/2$. The previous condition can thus always be satisfied if we choose $x_s > R_s/2$.

The amplitude $c_{i,k}^L(T)$ in Eq. (4.29) includes the time-dependent interaction $V_L(t)$. Let T_{impact} be the instant at which the fastest part of the dissociative WP hits the surface $R = R_s$. Then $c_{i,k}^L(T)$ can be neglected as long as $T_{\text{impact}} \geq \tau$, with τ the pulse duration. This can be seen by rewriting Eq. (4.29) as

$$c_{i,k}^L(T) = -i \int_{-\infty}^T dt \left\{ \langle \phi_{el,i}(t) | \langle \chi_k(t) | V_L(t) (1 - \theta_e) \theta_N | \Psi(t) \rangle \right. \\ \left. + \langle \phi_{el,i}(t) | \langle \chi_k(t) | \left[(1 - \theta_e), V_L(t) \right] \theta_N | \Psi(t) \rangle \right\} \quad (4.30)$$

with the commutator in the velocity gauge given by

$$\left[(1 - \theta_e), V_L(t) \right] = -i\beta A(t) \int d|x\rangle \text{sgn}(x) \delta(|x| - x_s) \langle x|. \quad (4.31)$$

For $T_{\text{impact}} \geq \tau$, both terms in Eq. (4.30) are zero. The first term is zero because $|\Psi_D(t)\rangle = (1 - \theta_e) \theta_N |\Psi(t)\rangle = 0$ for $t < \tau$, while $V_L(t) = 0$ for $t > \tau$. Similarly, the second term is zero because $\Psi(\pm x_s, R, t) = 0$. The condition $T_{\text{impact}} \geq \tau$ depends on the interaction $V_L(t)$ and can be satisfied by placing the R_s appropriately.

The final expression for the $c_{i,k}(T)$ is then, using Eq. (4.14) and Eq. (4.26),

$$c_{i,k}(T) = \frac{1}{m_p} \int_{-\infty}^T dt \chi_k^*(R_s, t) \left[k - i \frac{\partial}{\partial R} \right] \langle \phi_{el,i}(t) | (1 - \theta_e) | \Psi(t) \rangle \Big|_{R_s}. \quad (4.32)$$

We see that the differential probability amplitude $c_{i,k}(T)$ can be calculated by monitoring the flux going through the surface $R = R_s$. Moreover, the electronic BO-states $\phi_{el,i}(x; R)$ with parametric dependence on R only has to be calculated at points near R_s , reducing the numerical effort.

tSURFF for dissociation – the surface model

The NKER spectrum in the surface model [Section 2.2] can also be obtained by the tSURFF method. The dissociation-channel-specific differential probability amplitudes $c_{i,k}^{BO}(T)$, with $i = 0, \dots, N_{BO} - 1$, reads

$$\begin{aligned} c_{i,k}^{BO}(T) &= \langle \chi_k(T) | \theta_N | G_i(T) \rangle \\ &= \frac{1}{m_p} \int_{-\infty}^T dt \chi_k^*(R_s, t) \left[k - i \frac{\partial}{\partial R} \right] G_i(t) \Big|_{R_s}, \end{aligned} \quad (4.33)$$

which is obtained using the same techniques as the rest of this section. We have assumed that the laser pulse is over at the time the dissociative WPs first hit the surface R_s . To check this method, the dissociative spectrum within the two-surface model obtained using tSURFF was compared with the results in Ref. [95], and a perfect match was observed.

Numerical demonstrations – NKER for dissociation

We here give a demonstration of tSURFF for the dissociation process and provide some numerical results, using the same simulation parameters as for the demonstration of tSURFF for DI.

Figure 4.3(a) shows the NKER spectrum for the 400 nm pulse with dissociation via the two lowest electronic states in H_2^+ : $\phi_{el,0}^{g/u}$ corresponding to the $1s\sigma_g$ and $2p\sigma_u$ states. The vertical dashed lines in Fig. 4.3(a) are the n -photon energy conservation lines satisfying $E_0 + n\omega = E_{el,0}(R = \infty) + E_N$, where $E_{el,0}(R = \infty)$ is the ground state energy of the hydrogen atom. Dissociation via $1s\sigma_g$ is located around the 2-photon line, while dissociation via $2p\sigma_u$ is located around the 3-photon line. This result can be understood by drawing the diabatic Floquet potential curves [96, 97], shown in Fig. 4.4(a).

Starting from the vibrational ground state, the laser can induce a dissociative wave packet by the ATD process, which will move down the $2p\sigma_u - 3\omega$ curve. The time for the wave packet to move from the intersection between $1s\sigma_g - 0\omega$ and $2p\sigma_u - 3\omega$ at $R = 2.23$ a.u. to the intersection between $1s\sigma_g - 2\omega$ and $2p\sigma_u - 3\omega$ at $R = 4.7$ a.u. is approximately 204 a.u. (4.93 fs). At the latter intersection, part of the population can be transferred to the $1s\sigma_g - 2\omega$ curve by stimulated photoemission. The time for the population to move from $R = 4.7$ to $R = 10$ via the surface $1s\sigma_g - 2\omega$ is approximately 311 a.u. (7.52 fs), so the total time to reach $R = 10$ a.u. from the vibrational groundstate via the described pathway approximately equals the pulse duration of 13.3 fs. The pulse duration is therefore not long enough to induce transitions between the $1s\sigma_g - 2\omega$ and $2p\sigma_u - 1\omega$ curves, nor is it intense enough to lower the adiabatic Floquet potentials (gap proportional

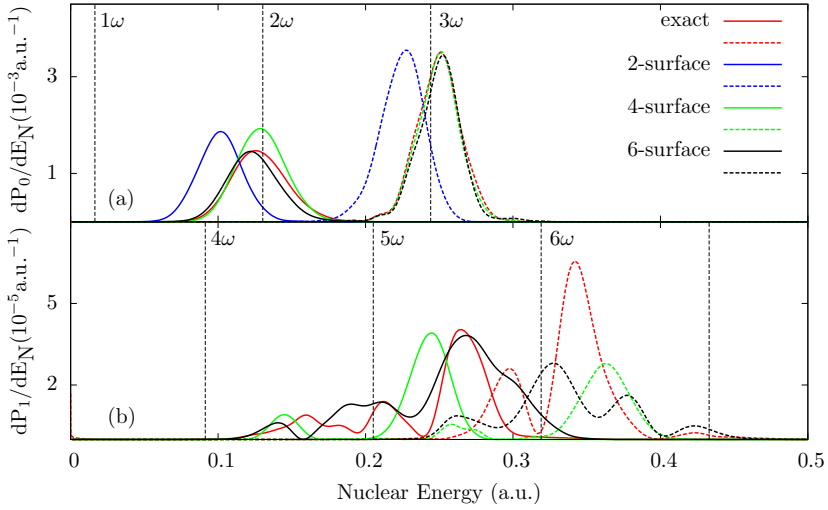


Figure 4.3: NKER spectra for dissociation with pulse parameters $\lambda = 400$ nm, $N_c = 10$, and $I = 8.8 \times 10^{13}$ W/cm², with dissociation via (a) the first pair of gerade or ungerade states ($1s\sigma_g$ and $2p\sigma_u$), and (b) the second pair of gerade or ungerade states ($2s\sigma_g$ and $3p\sigma_u$). As indicated, different colors correspond to different methods used for the calculations. The solid and dashed lines show dissociation via the gerade and ungerade states, respectively. In the BO calculations, the spectra are scaled for easier comparison with the TDSE calculation. The vertical lines labeled by $n\omega$ ($n = 1, 2, \dots, 6$) denote photon absorptions above threshold (see text).

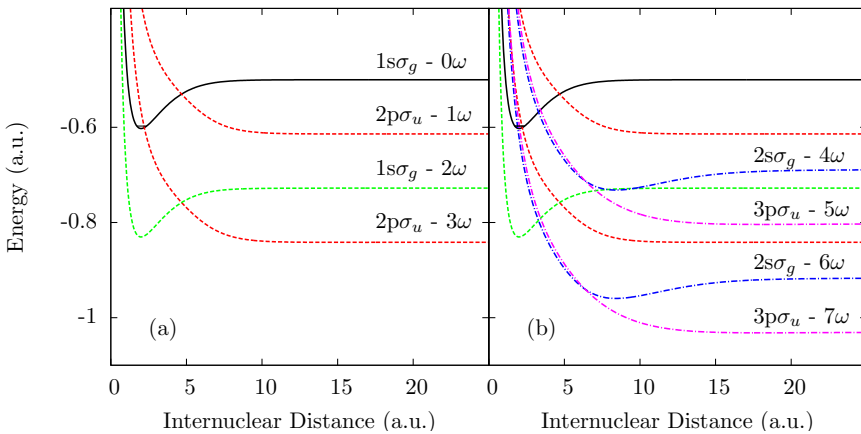


Figure 4.4: The diabatic Floquet potentials for 1D H_2^+ with $\lambda = 400$ nm. (a) Relevant dressed curves of $1s\sigma_g$ and $2p\sigma_u$ states. (b) Additional dressed curves of $2s\sigma_g$ and $3p\sigma_u$ states.

to electric field) to induce tunneling from the vibrational ground state ($v = 0$) to the $2p\sigma_u - 1\omega$ curve. This is the reason for the absence of the 1-photon peak in the nuclear KER spectrum.

In addition to the TDSE calculation, calculations in the BO-approximation are performed for the surface model with $N_{BO} = 2, 4, 6$. In Fig. 4.3(a) it is seen that the nuclear KER yield for the 2-surface model is shifted more from the energy conservation lines than the TDSE calculation, indicating that the AC-Stark shift is inaccurately accounted for in the 2-surface model. Moreover, the ratio of the $1s\sigma_g$ dissociation yield to the $2p\sigma_u$ dissociation yield is overestimated in the 2-surface model. As seen in Fig. 4.3(a), the dissociation spectra is somewhat improved in the 4-surface model, where the peaks now are located at the correct positions, but the ratio of the $1s\sigma_g$ dissociation yield to the $2p\sigma_u$ dissociation yield is still overestimated. For the 6-surface model, the spectra almost overlaps with the spectra in the full TDSE calculation, with correct locations and ratio. This result indicates that when six BO states are used instead of four, additional dressed states can couple to $1s\sigma_g$, leading to depletion in the dissociation wave packet in $1s\sigma_g$, resulting in the correct spectra.

Figure 4.3(b) shows the nuclear KER spectrum for the 400 nm pulse with dissociation via the third and fourth electronic states $\phi_{el,1}^{g/u}$ corresponding to the $2s\sigma_g$ and $3p\sigma_u$ states. The vertical dashed lines in Fig. 4.3(b) are the n -photon energy conservation lines satisfying $E_0 + n\omega = E_{el,1}(R = \infty) + E_N$, where $E_{el,1}(R = \infty)$ is the energy of the first excited state in hydrogen. Dissociation via $2s\sigma_g$ is located between the 4- and 6-photon lines, while dissociation via $3p\sigma_u$ is located between the 5- and 7-photon lines.

To understand the dissociation spectrum in Fig. 4.3(b), the Floquet potential curves for $2s\sigma_g$ and $3p\sigma_u$ dressed by four to seven photons are plotted in Fig. 4.4(b). Furthermore, a study is performed where we gradually increase the intensity of the laser field and observe the resulting nuclear KER spectra, shown in Fig. 4.5. At lower intensities, $I \lesssim 2 \times 10^{13}$ W/cm² in Figs. 4.5(a) and 4.5(b), the 4-photon peak for the gerade state and the 5-photon peak for the ungerade state are clearly seen, stemming from the wave packet following the pathway $1s\sigma_g - 0\omega \rightarrow 2p\sigma_u - 3\omega \rightarrow 1\sigma_g - 2\omega \rightarrow 2\sigma_g - 4\omega$ and $3p\sigma_u - 5\omega$, shown in Fig. 4.4(b). This is also indicated by the $2s\sigma_g - 4\omega$ and $3p\sigma_u - 5\omega$ curves in Fig. 4.4(b). In Fig. 4.5(b) a small peak at around $E_N = 0.4$ a.u. is seen for the ungerade state and a smaller peak at around $E_N = 0.27$ a.u. is seen for the gerade state. These are the AC-Stark shifted 7-photon and 6-photon absorption peaks, respectively. Figure 4.4(b) clearly shows that the $3p\sigma_u - 7\omega$ and $2s\sigma_g - 6\omega$ curves cross the $1s\sigma_g - 0\omega$ curve at $R = 2$ a.u., below the energy of the vibrational groundstate ($v = 0$), leading to ATD processes explaining the peaks in Fig. 4.5(b). As the

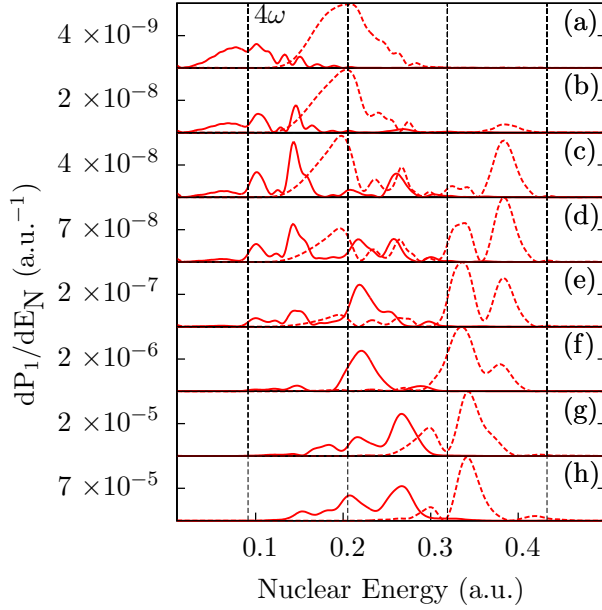


Figure 4.5: Each subplot is as in Fig. 4.3(b), now for the intensities: (a) $I = 1 \times 10^{13}$ W/cm², (b) $I = 2 \times 10^{13}$ W/cm², (c) $I = 3 \times 10^{13}$ W/cm², (d) $I = 3.5 \times 10^{13}$ W/cm², (e) $I = 4 \times 10^{13}$ W/cm², (f) $I = 5 \times 10^{13}$ W/cm², (g) $I = 8 \times 10^{13}$ W/cm², and (h) $I = 1 \times 10^{14}$ W/cm².

intensity is increased from Fig. 4.5(c) to Fig. 4.5(h), the 7-photon and 8-photon peaks are Stark shifted to lower nuclear energies, and additional structures in the peaks emerge. The additional structures are believed to be due to the interferences from the near-degeneracy of the $3p\sigma_u - 7\omega$ and $2s\sigma_g - 6\omega$ curves in Fig. 4.4(b) for $R < 7$ a.u., i.e. the strong coupling inducing many 1-photon absorption/emission paths that all lead to the same final dissociating state.

In Figure 4.3(b) the corresponding N -surface calculations with $N = 4, 6$ are shown. For the N -surface calculations, the peaks are located in the same energy region as the TDSE calculation, ranging from $E_N = 0.1$ to $E_N = 0.35$ for the $2s\sigma_g$ yields and from $E_N = 0.22$ to $E_N = 0.5$ for the $3p\sigma_u$ yields. However, the structures in the spectra are very different, indicating that coupling to even higher excited electronic states and the double continuum are important. Thus, the numerous previous descriptions of the dissociation process of H_2^+ where the 2-surface model has been used [95, 96, 98–102], are inadequate to describe all the correct dissociation processes. We have thus demonstrated here that the tSURFF method can be used to efficiently extract the NKER for dissociation.

4.2 Continuum observables in many-electron systems

For many-electron systems, the extraction of continuum observables from a TDSE solver presents a challenge as well. We will here present a generalized tSURFF method that is able to obtain the PAD and the differential PMS and PES for single ionization from TD-GASCI, formulated in second quantization.

4.2.1 Single-ionization projection operator

We define the operator

$$\hat{\theta}_s = \int d\mathbf{q} \hat{\psi}^\dagger(\mathbf{q}) \hat{\psi}(\mathbf{q}) \theta_{r_s}(r), \quad (4.34)$$

where $\hat{\psi}^\dagger(\mathbf{q})$ ($\hat{\psi}(\mathbf{q})$) is a creation (annihilation) field operator with position-spin coordinate $\mathbf{q} = (\mathbf{r}, \sigma)$, the integral is $\int d\mathbf{q} \equiv \sum_\sigma \int d\mathbf{r}$, and $\theta_{r_s}(r) \equiv \theta(r - r_s)$ with θ the Heaviside step function. The field operators satisfy the anti-commutation relations

$$\begin{aligned} \left\{ \hat{\psi}(\mathbf{q}), \hat{\psi}(\mathbf{q}') \right\} &= \left\{ \hat{\psi}^\dagger(\mathbf{q}), \hat{\psi}^\dagger(\mathbf{q}') \right\} = 0 \\ \left\{ \hat{\psi}(\mathbf{q}), \hat{\psi}^\dagger(\mathbf{q}') \right\} &= \delta(\mathbf{r} - \mathbf{r}') \delta_{\sigma\sigma'}. \end{aligned} \quad (4.35)$$

In Eq. 4.34, the surface radius r_s is chosen sufficiently large such that for $r > r_s$ the binding potentials can be neglected and the electron only feels the laser field. To be a projection operator, $\hat{\theta}_s$ must be idempotent, satisfying $\hat{\theta}_s = \hat{\theta}_s \hat{\theta}_s$, but a simple calculation shows

$$\begin{aligned} \hat{\theta}_s \hat{\theta}_s &= \int d\mathbf{q}' \int d\mathbf{q} \hat{\psi}^\dagger(\mathbf{q}) \hat{\psi}(\mathbf{q}) \hat{\psi}^\dagger(\mathbf{q}') \hat{\psi}(\mathbf{q}') \theta_{r_s}(r) \theta_{r_s}(r') \\ &= \hat{\theta}_s + 2\hat{\theta}_d, \end{aligned} \quad (4.36)$$

with

$$\hat{\theta}_d = \frac{1}{2} \int d\mathbf{q}' \int d\mathbf{q} \hat{\psi}^\dagger(\mathbf{q}') \hat{\psi}^\dagger(\mathbf{q}) \hat{\psi}(\mathbf{q}) \hat{\psi}(\mathbf{q}') \theta_{r_s}(r) \theta_{r_s}(r'). \quad (4.37)$$

The involvement of $\hat{\theta}_d$ in Eq. (4.36) seems to make $\hat{\theta}_s$ non-idempotent, but for all the TD-GASCI partition schemes considered in this work, only a single particle is included in the continuum, such that $\hat{\theta}_s$ is actually a projection unto the single-ionized space. Indeed, by considering the total wave function $|\Psi(t)\rangle$ as a linear combination of determinants with maximal one continuum orbital occupied in each determinant, $\hat{\theta}_d |\Psi(t)\rangle = 0$ and $\hat{\theta}_s |\Psi(t)\rangle \xrightarrow{t \rightarrow \infty} |S\rangle$, where $|S\rangle$ contains only the single-ionized terms of $|\Psi(t)\rangle$.

For completeness, we discuss here the general case of multiple ionization. Consider first a TD-GASCI partition scheme with max two electrons in the continuum. A simple calculation shows

$$\hat{\theta}_d \hat{\theta}_d = \hat{\theta}_d + \hat{\theta}_{\text{higher-order}}, \quad (4.38)$$

with $\hat{\theta}_{\text{higher-order}}$ containing normal-ordered operator strings with three or more field-operator pairs. As max two electrons in the continuum are assumed to be allowed, $\hat{\theta}_d$ projects out the double-ionized part of the wave function, as can be easily checked for the simple example $\hat{\theta}_d \hat{\psi}^\dagger(\mathbf{q}_1) \hat{\psi}^\dagger(\mathbf{q}_2) |0\rangle = \hat{\psi}^\dagger(\mathbf{q}_1) \hat{\psi}^\dagger(\mathbf{q}_2) |0\rangle$ with $r_1, r_2 > r_s$. The single-ionized part can be projected out by the operator $\hat{\theta}_s - \hat{\theta}_d$, which satisfies the idempotent condition

$$\begin{aligned} (\hat{\theta}_s - \hat{\theta}_d)(\hat{\theta}_s - \hat{\theta}_d) &= \hat{\theta}_s \hat{\theta}_s - (\hat{\theta}_s \hat{\theta}_d + \hat{\theta}_d \hat{\theta}_s) + \hat{\theta}_d \hat{\theta}_d \\ &= (\hat{\theta}_s + 2\hat{\theta}_d) - 4\hat{\theta}_d + (\hat{\theta}_d + \hat{\theta}_{\text{higher-order}}) \\ &= (\hat{\theta}_s - \hat{\theta}_d) + \hat{\theta}_{\text{higher-order}}. \end{aligned} \quad (4.39)$$

For the general case, let N_{cont} denote the maximal continuum electrons allowed in a specific TD-GASCI scheme, and let m denote the specific ionization process, with $m = 1$ for single ionization, $m = 2$ for double ionization and so on. The projection operator that gives us the part of $|\Psi(t \rightarrow \infty)\rangle$ with exactly m ionized electrons is

$$\hat{\theta}(N_{\text{cont}}, m) = \hat{\theta}_m - \hat{\theta}_{m+1} - \dots - \hat{\theta}_{N_{\text{cont}}}, \quad (4.40)$$

with $\hat{\theta}_1 = \hat{\theta}_s$, $\hat{\theta}_2 = \hat{\theta}_d$, and the other $\hat{\theta}_i$ defined analogously.

As mentioned, for the TD-GASCI partition schemes considered in this thesis, a maximum of one electron is assumed in the continuum, meaning that $\hat{\theta}_s$ in Eq. (4.34) is a projection onto the single-ionized space. This is assumed henceforth.

4.2.2 PAD flux method

At asymptotic large times T when the ionized WPs have moved beyond the radius r_s , the probability of occupation in the single-ionized configuration space is

$$\begin{aligned} P_{\text{ion}}(T) &= \langle \Psi(T) | \hat{\theta}_s \hat{\theta}_s | \Psi(T) \rangle \\ &= \langle \Psi(T) | \hat{\theta}_s | \Psi(T) \rangle \\ &= i \int^T dt \langle \Psi(t) | [H(t), \hat{\theta}_s] | \Psi(t) \rangle, \end{aligned} \quad (4.41)$$

where we used Eq. (4.37) at the second equality, and the Schrödinger equation and the fundamental theorem of calculus at the third equality. The Hamiltonian

in FNA

$$H = T_e + V_{eN} + V_{ee} + V_L(t), \quad (4.42)$$

is given in terms of the field operators in second quantization

$$T_e = -\frac{1}{2} \int d\mathbf{q} \hat{\psi}^\dagger(\mathbf{q}) \nabla_{\mathbf{r}}^2 \hat{\psi}(\mathbf{q}), \quad (4.43a)$$

$$V_{eN} = \int d\mathbf{q} \hat{\psi}^\dagger(\mathbf{q}) V_{eN}(\mathbf{r}) \hat{\psi}(\mathbf{q}), \quad (4.43b)$$

$$V_{ee} = \frac{1}{2} \int d\mathbf{q} \int d\mathbf{q}' \hat{\psi}^\dagger(\mathbf{q}) \hat{\psi}^\dagger(\mathbf{q}') V_{ee}(|\mathbf{r} - \mathbf{r}'|) \hat{\psi}(\mathbf{q}') \hat{\psi}(\mathbf{q}), \quad (4.43c)$$

$$V_L(t) = \int d\mathbf{q} \hat{\psi}^\dagger(\mathbf{q}) V_L(\mathbf{r}, t) \hat{\psi}(\mathbf{q}), \quad (4.43d)$$

with the laser field interaction $V_L(\mathbf{r}, t) = -i\mathbf{A}(t) \cdot \nabla_{\mathbf{r}}$ in velocity gauge and $V_L(\mathbf{r}, t) = \mathbf{E}(t) \cdot \mathbf{r}$ in length gauge. The following commutators can be derived (not shown in this thesis) in spherical coordinates (a linearly polarized field in the positive z direction is assumed),

$$[T, \hat{\theta}_s] = \frac{1}{2} \sum_{\sigma} \int d\Omega r^2 \left(\frac{\partial}{\partial r} \hat{\psi}^\dagger(\mathbf{q}) \hat{\psi}(\mathbf{q}) - \hat{\psi}^\dagger(\mathbf{q}) \frac{\partial}{\partial r} \hat{\psi}(\mathbf{q}) \right) \Big|_{r=r_s}, \quad (4.44a)$$

$$[V_{eN}, \hat{\theta}_s] = [V_{ee}, \hat{\theta}_s] = 0, \quad (4.44b)$$

$$[V_L, \hat{\theta}_s] = \begin{cases} -iA(t) \sum_{\sigma} \int d\Omega r^2 \cos \theta \hat{\psi}^\dagger(\mathbf{q}) \hat{\psi}(\mathbf{q})|_{r=r_s} & \text{(VG)} \\ 0 & \text{(LG)} \end{cases} \quad (4.44c)$$

The field operators can be transformed into a spin-orbital basis

$$\begin{aligned} \hat{\psi}^\dagger(\mathbf{q}) &= \sum_{\bar{p}} \bar{\phi}_{\bar{p}}^*(\mathbf{q}) \hat{a}_{\bar{p}}^\dagger \\ \hat{\psi}(\mathbf{q}) &= \sum_{\bar{q}} \bar{\phi}_{\bar{q}}(\mathbf{q}) \hat{a}_{\bar{q}}, \end{aligned} \quad (4.45)$$

with the spin orbitals $\bar{\phi}_{\bar{p}}(\mathbf{q}) = \phi_{p, m_s}(\mathbf{r}, \sigma) = \phi_p(\mathbf{r}) \chi_{m_s}(\sigma) = \phi_p(\mathbf{r}) \delta_{m_s, \sigma}$. Insetting Eq. (4.44) into Eq. (4.41), and using Eq. (4.45), we obtain the final expression for P_{ion} in Eq. (4.41)

$$\begin{aligned} P_{\text{ion}} &= r_s^2 \int d\Omega \int^T dt \sum_{pq} D_{pq}(t) \\ &\times \left\{ \frac{i}{2} \left[\frac{\partial}{\partial r} \phi_p^*(\mathbf{r}) \phi_q(\mathbf{r}) - \phi_p^*(\mathbf{r}) \frac{\partial}{\partial r} \phi_q(\mathbf{r}) \right] + K_{pq}(\mathbf{r}, t) \right\} \Big|_{r=r_s}, \end{aligned} \quad (4.46)$$

with

$$K_{pq}(\mathbf{r}, t) = \begin{cases} A(t) \cos \theta \phi_p^*(\mathbf{r}) \phi_q(\mathbf{r}) & \text{(VG)} \\ 0 & \text{(LG)} \end{cases} \quad (4.47)$$

and the reduced one-particle spin-independent density matrix

$$D_{pq}(t) = \sum_{\sigma} \langle \Psi(t) | \hat{a}_{p\sigma}^{\dagger} \hat{a}_{q\sigma} | \Psi(t) \rangle. \quad (4.48)$$

The expression for the PAD is then

$$\begin{aligned} \frac{dP_{\text{ion}}}{d\Omega} = & r_s^2 \int^T dt \sum_{pq} D_{pq}(t) \\ & \times \left\{ \frac{i}{2} \left[\frac{\partial}{\partial r} \phi_p^*(\mathbf{r}) \phi_q(\mathbf{r}) - \phi_p^*(\mathbf{r}) \frac{\partial}{\partial r} \phi_q(\mathbf{r}) \right] + K_{pq}(\mathbf{r}, t) \right\} \Big|_{r=r_s}. \end{aligned} \quad (4.49)$$

When a CAP is placed at $r > r_{\text{CAP}} > r_s$ to absorb the outgoing flux and to prevent reflection at the simulation boundaries, one has to make sure that Eq. (4.49) is unchanged when $|\Psi(t)\rangle$ is replaced by $|\Psi'(t)\rangle$, the solution to TDSE with the CAP included. Obviously $D'_{pq}(t) = \sum_{\sigma} \langle \Psi'(t) | \hat{a}_{p\sigma}^{\dagger} \hat{a}_{q\sigma} | \Psi'(t) \rangle$ is not equal to $D_{pq}(t)$ for every p and q , but because the orbitals in the outer region $\phi_p^*(\mathbf{r})$ are localized FE-DVR functions, the sum in Eq. (4.49) will only run over indices p and q with the $D_{pq}(t) = D'_{pq}(t)$ condition satisfied. This shows that the PAD can be obtained with Eq. (4.49) even when a CAP is used.

The radius r_s is always taken outside the HF region, so the orbitals in Eq. (4.49) are the primitive spatial orbitals. For atoms, the spherical coordinate system with the orbitals $\phi_{klm}(r, \theta, \varphi) = f_k(r) Y_{lm}(\theta, \varphi)/r$ is the natural choice, and evaluation of Eq. (4.49) is straightforward using the FE-DVR functions $f_k(r)$. In the case of diatomics, the prolate spheroidal basis is preferred. For the calculation of the PAD, a desired grid in spherical coordinates $(r_s, \theta_i, \varphi_j)$ (with i, j grid indices) is first defined, then transformed into the corresponding prolate spheroidal grid $(\zeta_i, \mu_i, \varphi_j)$ using Eqs. (D.2) and (D.6). The orbitals $\phi_p(\zeta_i, \mu_i, \varphi_j)$ and orbital derivatives $\partial \phi_p(\zeta, \mu, \varphi)/\partial r = (\partial \zeta/\partial r) \partial \phi_p(\zeta, \mu, \varphi)/\partial \zeta + (\partial \mu/\partial r) \partial \phi_p(\zeta, \mu, \varphi)/\partial \mu$ can then be evaluated in at $(\zeta_i, \mu_i, \varphi_j)$, and the PAD in Eq. (4.49) be calculated.

4.2.3 PMS and PES flux method

We now derive a flux method that can be efficiently used to obtain the PMS and PES for single ionization in multi-electron codes such as TD-GASCI.

Ionization channel

We define a single-ionization channel

$$|\Phi_{c,\mathbf{p},m_s}(t)\rangle = |\Phi_c^{\text{ion}}(t)\rangle |\phi^V(\mathbf{p}, m_s, t)\rangle, \quad (4.50)$$

with $|\phi^V(\mathbf{p}, m_s, t)\rangle$ describing a free electron with canonical momentum \mathbf{p} and spin projection m_s , and $|\Phi_c^{\text{ion}}(t)\rangle$ the c 'th ionic channel. We approximate $|\phi^V(\mathbf{p}, m_s, t)\rangle$ by a Volkov state, so that the form of $|\phi^V(\mathbf{p}, m_s, t)\rangle$ in spatial representation is

$$\langle \mathbf{r} | \phi^V(\mathbf{p}, m_s, t) \rangle = \begin{cases} \langle \mathbf{r} | \mathbf{p} \rangle e^{-iS^{\text{VG}}(\mathbf{p}, t)} |\chi_{m_s}\rangle, & \text{(VG)} \\ \langle \mathbf{r} | \mathbf{p} + \mathbf{A}(t) \rangle e^{-iS^{\text{LG}}(\mathbf{p}, t)} |\chi_{m_s}\rangle, & \text{(LG)}, \end{cases} \quad (4.51)$$

with the spin ket $|\chi_{m_s}\rangle$, the Volkov phases

$$\begin{aligned} S^{\text{VG}}(\mathbf{p}, t) &= \int_{-\infty}^t \left[\frac{\mathbf{p}^2}{2} + \mathbf{p} \cdot \mathbf{A}(t') \right] dt', \\ S^{\text{LG}}(\mathbf{p}, t) &= \frac{1}{2} \int_{-\infty}^t [\mathbf{p} + \mathbf{A}(t')]^2 dt', \end{aligned} \quad (4.52)$$

and

$$\langle \mathbf{r} | \mathbf{p} \rangle = (2\pi)^{-3/2} e^{i\mathbf{p} \cdot \mathbf{r}}. \quad (4.53)$$

The second quantized operator that describes a Volkov state $\phi^{V\dagger}(\mathbf{p}, m_s, t)$ in the spin-orbital representation is

$$\begin{aligned} \phi^V(\mathbf{p}, m_s, t) &= \phi^{V\dagger}(\mathbf{p}, m_s, t) |0\rangle = \sum_{i, \sigma} |i, \sigma\rangle \langle i, \sigma | \phi^V(\mathbf{p}, m_s, t) \rangle \\ &= \sum_{i, \sigma} \langle i, \sigma | \left(\int |\mathbf{r}\rangle \langle \mathbf{r}| d^3\mathbf{r} \right) |\phi^V(\mathbf{p}, m_s, t)\rangle \hat{a}_{i, \sigma}^\dagger |0\rangle \\ &= \sum_i \underbrace{\int \phi_{i, m_s}^*(\mathbf{r}) \langle \mathbf{r} | \phi^V(\mathbf{p}, m_s, t) \rangle d^3\mathbf{r}}_{\equiv \phi_i^*(\mathbf{p}, t)} \hat{a}_{i, m_s}^\dagger |0\rangle. \end{aligned} \quad (4.54)$$

Using Eq. (4.51), we obtain for the (spin-independent) momentum-space Volkov orbitals

$$\phi_i^*(\mathbf{p}, t) = \begin{cases} \phi_i^*(\mathbf{p}) e^{-iS^{\text{VG}}(\mathbf{p}, t)} & \text{(VG)} \\ \phi_i^*(\mathbf{p} + \mathbf{A}(t)) e^{-iS^{\text{LG}}(\mathbf{p}, t)} & \text{(LG)}, \end{cases} \quad (4.55)$$

with the momentum space representation of the spatial orbital

$$\phi_i^*(\mathbf{p}) = (2\pi)^{-3/2} \int d^3\mathbf{r} \phi_i^*(\mathbf{r}) e^{i\mathbf{p} \cdot \mathbf{r}}. \quad (4.56)$$

In Eq. (4.55) we see that $\phi_i^*(\mathbf{p}, t)$ in velocity gauge is just a position-independent phase factor multiplied by the momentum space orbital, which often can be calculated once, stored, and then reused at each time during time propagation. In length gauge, on the other hand, since $\phi_i^*(\mathbf{p})$ is not known analytically (at least not derived here), to calculate $\phi_i^*(\mathbf{p} + \mathbf{A}(t))$, the integral in Eq. (4.55) must be evaluated at each time-step, making it computationally unfeasible.

PMS amplitude

At a sufficiently large time T at which all the single-ionized fragments has moved into the configuration space specified by $\hat{\theta}_s$, the momentum amplitude for single-ionization into the channel state $|\Phi_{c,\mathbf{p},m_s}(T)\rangle$ can be written

$$\begin{aligned} b_{c,\mathbf{p},m_s}(T) &= \langle \Phi_{c,\mathbf{p},m_s}(T) | \hat{\theta}_s | \Psi(T) \rangle \\ &= i \int dt \langle \Phi_{c,\mathbf{p},m_s}(t) | [H, \hat{\theta}_s] | \Psi(t) \rangle \\ &= i \int dt \langle \phi^V(\mathbf{p}, m_s, t) | [H, \hat{\theta}_s] \langle \Phi_c^{\text{ion}}(t) | \Psi(t) \rangle, \end{aligned} \quad (4.57)$$

where we at the second equality used that the states $|\Phi_{c,\mathbf{p},m_s}(t)\rangle$ and $|\Psi(t)\rangle$ satisfy the same TDSE. At the third equality in Eq. (4.57), we have commuted $\langle \Phi_c^{\text{ion}} |$ to the right as it assumed that the ionic bound state is confined to $r \ll r_s$, and the commutator acts near the surface $r \approx r_s$. The overlap between the N -electron state and the $(N-1)$ -electron ionic state, $\langle \Phi_c^{\text{ion}}(t) | \Psi(t) \rangle$, is the (time-dependent) Dyson orbital, which we here will denote as $|\mathcal{Y}_c(t)\rangle$. The evaluation and implementation of the Dyson orbital in the TD-GASCI is described in Sec. 8.3. Here, the Dyson orbital in spin-orbital representation can be written

$$\begin{aligned} |\mathcal{Y}_c(t)\rangle &\equiv \langle \Phi_c^{\text{ion}}(t) | \Psi(t) \rangle \\ &= \sum_i \underbrace{\langle i, m_s | \mathcal{Y}_c(t) \rangle}_{\equiv d_i(t)} \hat{a}_{i,m_s}^\dagger | 0 \rangle. \end{aligned} \quad (4.58)$$

To evaluate the time-dependent Dyson orbital, the $(N-1)$ -electron ionic channel states $|\Phi_c^{\text{ion}}(t)\rangle$ are needed at all times. We prepare the $(N-1)$ -electron ionic state $|\Phi_c^{\text{ion}}(T)\rangle$ in the primitive basis of the N -electron problem, and obtain and store the CI vector of $|\Phi_c^{\text{ion}}(t)\rangle$ by propagating it backwards in time to $t=0$.

Insertion of the commutators (4.44), the basis transformations (4.45), and the Volkov state (4.54) into Eq. (4.57), we obtain the expression for the channel-resolved transition amplitude in velocity gauge

$$\begin{aligned} b_{c,\mathbf{p},m_s}^{\text{VG}}(T) &= ir_s^2 \int dt e^{iS^{\text{VG}}(\mathbf{p},t)} \int d\Omega \\ &\times \left\{ \frac{1}{2} \sum_{pq} \phi_p(\mathbf{p}) \left[\frac{d}{dr} \phi_p^*(r) \phi_q(r) - \phi_p^*(r) \frac{d}{dr} \phi_q(r) \right]_{r=r_s} d_q(t) \right. \\ &\left. - iA(t) \cos \theta \sum_{pq} \phi_p(\mathbf{p}) \phi_p^*(r) \phi_q(r) d_q(t) \Big|_{r=r_s} \right\}, \end{aligned} \quad (4.59)$$

and in length gauge

$$b_{c,\mathbf{p},m_s}^{\text{LG}}(T) = ir_s^2 \int dt e^{iS^{\text{LG}}(\mathbf{p},t)} \int d\Omega \times \frac{1}{2} \sum_{pq} \phi_p(\mathbf{p} + \mathbf{A}(t)) \left[\frac{d}{dr} \phi_p^*(r) \phi_q(r) - \phi_p^*(r) \frac{d}{dr} \phi_q(r) \right]_{r=r_s} d_q(t). \quad (4.60)$$

While the expression in length gauge seems to be of simpler form with one less term compared to the velocity gauge expression, the evaluation of $\phi_p(\mathbf{p} + \mathbf{A}(t))$ at each time mentioned in previous subsection makes the length gauge form computationally unfeasible. Henceforth in this chapter we consider the velocity gauge.

Recently, similar expressions to the one presented in Eq. (4.60) were presented in Ref. [103], used in the hybrid coupled channels approach. However, our current calculation and derivation are done in second quantization, and are directly applicable in the TD-GASCI method.

4.2.4 Demonstration of the flux methods

Although the implementation of the PAD and PMS flux methods should be possible and straightforward to implement in the spherical and prolate basis, this is not yet done. Instead, to demonstrate the method, we implement it for a reduced-dimensionality model for He, where the electrons are confined to one dimension only. The Hamiltonian considered is

$$H(t) = \sum_{i=1,2} \left(-\frac{1}{2} \frac{\partial^2}{\partial z_i^2} - \frac{2}{\sqrt{(z_i - z_{\text{He}})^2 + 1}} - iA(t) \frac{\partial}{\partial z_i} \right) + \frac{1}{\sqrt{(z_1 - z_2)^2 + 1}}, \quad (4.61)$$

with z_{He} the position of the He nucleus.

For a \sin^2 pulse with $\omega = 1.5$, $F_0 = 0.05$ and $N_c = 10$, we calculate the PMS using the flux method for the single-ionization channel with the ion at $t = T$ is in the ground state. The CIS partition is used in the TD-GASCI, and results for the total PMS for both spins projections

$$\frac{dP}{dp} = \sum_{m_s} |b_{c,\mathbf{p},m_s}^{\text{VG}}(T)|^2 \quad (4.62)$$

are shown in Fig. 4.6. Except at small values of $|p|$ which are generally difficult to converge, the PMS is seen to be converged to the accuracy 10^{-9} w.r.t variation of z_s . Also plotted in Fig. 4.6 are the results obtained by calculating the momentum distribution [68] at T

$$n(\mathbf{p}, T) = \sum_{pq} \rho_{pq}(T) \phi_p^*(\mathbf{p}) \phi_q(\mathbf{p}), \quad (4.63)$$

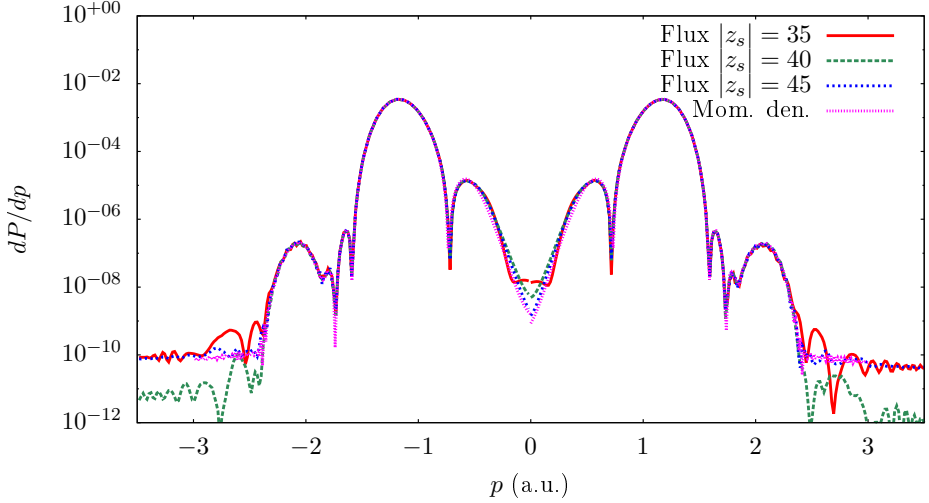


Figure 4.6: PMS for ionization of 1D He in the ionic ground state, calculated using the CIS partition scheme in TD-GASCI, for a pulse with parameters $\omega = 1.5$, $F_0 = 0.05$ and $N_c = 6$. Simulation box is $z \in [0, 110]$ with the inner HF region $z \in [50, 60]$ and the atom placed at $z_{\text{He}} = 55$. Length of each FE interval is 2, 8 DVR function are used in each FE, CAP acts in the region $|z - z_{\text{He}}| > z_{\text{CAP}} = 46$, and final time in the propagation is chosen as $T = 150$, with time step $\Delta t = 0.2$. Also shown is the PMS from the momentum-space density, obtained for time-propagation without CAP and $z \in [0, 490]$, $z_{\text{He}} = 245$.

with ρ_{pq} the spin-independent density matrix. This way of obtaining the PMS requires the asymptotic parts of the single-ionized WPs to be well-represented, and time-propagation is performed without the CAP. The simulation volume is $z \in [0, 490]$ ($z_{\text{He}} = 245$), which should be compared to $z \in [0, 110]$ used in the flux method, which again illustrates the advantage of flux methods. The PMS calculated in the two methods agree quite well.

In Table. 4.1 the ionization probabilities are shown, calculated using three different methods: integration of the flux method PMS in Fig. 4.6; using the flux PAD method described in Sec. 4.2.2 adapted to 1D; and by calculating the norm $1 - \langle \Psi(T) | \Psi(T) \rangle$ removed by the CAP. A single run of the program is used to obtain all results in Table. 4.1. The total PAD flux norm and CAP norm are the same to the accuracy considered, indicating the accuracy of the flux method. The difference in norms between PMS integration and PAD flux is because only the PMS for ionization into the ground ionic state is calculated here, and thus 1.8×10^{-5} is the norm for ionization into the excited states of He.

We have thus demonstrated that the flux method derived for single ionization for TD-GASCI works quite well.

Table 4.1: Left, right, and total ionization probabilities for ionization of 1D He for a pulse with $\omega = 1.5$, $F_0 = 0.05$ and $N_c = 6$. The total ionization probability in the last row is the total norm removed by the CAP. The results are for $r_s = 40$.

	Left (10^{-3})	Right (10^{-3})	Total (10^{-3})
PMS integration	1.103	1.103	2.205
PAD flux method	1.112	1.112	2.223
CAP norm			2.223

MOLECULAR DYNAMIC INTERFERENCE IN THE INTENSE XUV REGIME

As discussed in the introduction, recent advances in laser technology has led to the production of very intense femtosecond XUV laser pulses, with intensities greater than 4×10^{17} W/cm² being reported [43]. This has sparked the interest in the theoretical investigation of ionization using such intense XUV laser pulses in simple atomic systems [47, 48, 91, 104–106]. Modulations in the PES were discovered, with the following explanation. Due to the external field, the field-dressed ground state energy is shifted in time by the ac-Stark shift, which follows the laser field intensity envelope. There are two times during the pulse at which there is resonance conditions to the same continuum energy, once at the rising part and another at the falling part of the laser pulse [47, 48]. The two electronic wave packets ionized at the two different times pick up different phases during the duration of the pulse and interfere in the continuum, resulting in the interference structure observed in the PES. This ac-Stark shift induced effect is referred to as the dynamic interference [48]. In this chapter, we show, by considering H₂⁺, that the dynamic interference effect can be observed in molecules, and models are presented to describe the effect.

5.1 Numerical results

For our numerical calculations, we use the simulation volume $|x| \leq 200$ and $R \leq 60$, with grid spacings $\Delta x = 0.391$ and $\Delta R = 0.059$. The CAPs are placed at $x_{\text{CAP}} = 110$ and $R_{\text{CAP}} = 25$, and the tSURFF surfaces placed at $x_s = 100$, $R_s = 20$. The ground state energy is found by ITP to be $E_0 = -0.597$. We work in VG, and the pulse envelope chosen to be a Gaussian with FWHM τ . The

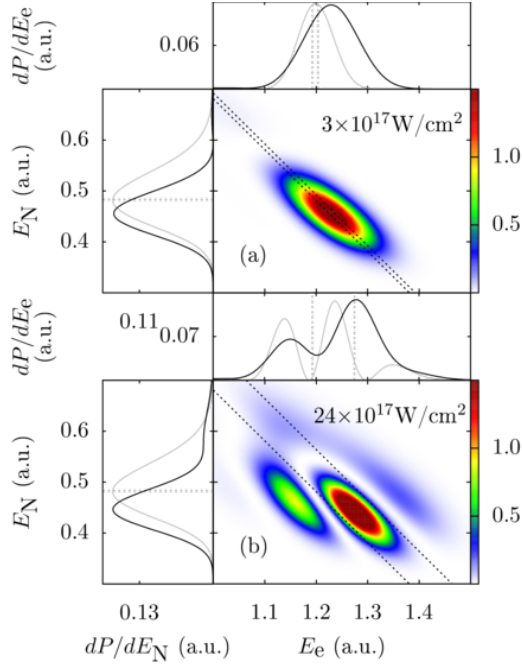


Figure 5.1: Spectra of H_2^+ exposed to pulses with $\omega = 2.278$, $\tau = 1.1$ fs and two different intensities I . Main panels show the JES. The left and right dashed diagonal lines indicate the energy conservations $E_e + E_N = E_0 + \omega$ and $E_e + E_N = E_0 + \omega + \Delta$, respectively, with Δ the Stark shift [Eq. (5.1)]. In the upper subpanels, thick, black curves show the PES obtained by integration of the JES, while the thin, grey curves show the PES for nuclei fixed at the equilibrium distance $R_0 = 2.06$. The fixed nuclei PES are scaled for better comparability with the moving nuclei PES. The dashed grey vertical lines show the energy conservations and Stark shifted energies for the fixed nuclei calculations. In the side subpanels, thick, black curves show the NKER obtained by integration of the JES, while the thin, grey curves show the scaled reflection principle results [Eq. (5.2)]. The horizontal dashed grey lines indicate the position $E_N = 1/R_0$.

carrier frequency of the laser pulse is chosen as $\omega = 2.278$, allowing for dissociative ionization by one-photon absorption, and the intensities are in the range from $I = 3 \times 10^{17}$ W/cm² to $I = 24 \times 10^{17}$ W/cm². Here, we are specifically interested in the first JES peak corresponding to one-photon absorption from the ground state, located close along the diagonal line $E_N + E_e \approx E_0 + \omega$ in the JES [see Fig. 5.1]. Note that although the pulses considered in this work are intense, we are still in the non-relativistic regime. Indeed, if the cycle-averaged quiver energy of a free electron (the ponderomotive energy) $U_p = A_0^2/4$ is much less than its rest energy $m_e c^2 = 137^2$, we are in the non-relativistic regime [107–109]. This condition is certainly satisfied here, as even for the most intense pulse $I = 24 \times 10^{17}$ W/cm² the ponderomotive energy is only $U_p = 3.29$.

Figure 5.1 shows the JES, NKER and PES for dissociative ionization of H_2^+ for laser pulses with $\tau = 1.1$ fs and two different intensities. In the JES panels, we define the Stark energy shift Δ of the ground state $|\Psi_0\rangle$ to be the shift at the field maximum, $t = 0$,

$$\Delta = \dot{\phi}(0) - E_0, \quad (5.1)$$

where $\phi(t)$ is the phase of the ground state amplitude $\langle \Psi_0 | \Psi(t) \rangle = |\langle \Psi_0 | \Psi(t) \rangle| e^{-i\phi(t)}$, which is directly extracted from the TDSE calculations [105]. In the side subpanels of Fig. 5.1, the NKER from the TDSE calculations and the reflection principle are shown. The reflection principle [110–112] amounts to the approximation where the electron is emitted into the continuum by the laser at the internuclear distance R , leaving behind two bare protons that Coulomb explode, gaining the kinetic energy $E_N = 1/R$. The NKER is then obtained by reflecting the probability density of the initial vibrational state $\chi_0(R)$, and weighting with $-dR/dE_N = 1/E_N^2$:

$$\frac{dP}{dE_N} \propto \frac{|\chi_0(1/E_N)|^2}{E_N^2}. \quad (5.2)$$

In the upper subpanels of Fig. 5.1, the PES are shown for the moving nuclei and fixed nuclei TDSE calculations. For the fixed nuclei calculations, we fix the internuclear distance at the equilibrium $R_0 \equiv \langle \Psi_0 | R | \Psi_0 \rangle = 2.06$.

For the intensity $I = 3 \times 10^{17}$ W/cm² in Fig. 5.1(a), the JES displays a single peak centered at $(E_e, E_N) = (1.23, 0.46)$, with a region of zero density along the line $E_N = 0.6$ (perhaps more discernible in the NES). In the NKER panel, the result for the reflection approximation peaks at $E_N = 1/R_0 = 0.484$, a clear shift with respect to the correct NKER peak located at 0.455. Furthermore, the minima at $E_N = 0.6$ is absent in the reflection principle result. This is to be expected, as the reflection principle is a crude approximation, and can only be used for qualitative analysis. In the PES panel, there is a shift of the peak of the fixed nuclei result compared to the moving nuclei result. This shift is due to the fact that the fixed nuclei result does not take into account the probability density of the initial vibrational state $|\chi_0(1/E_N)|^2$.

For the more intense pulse in Fig. 5.1(b), additional structures appear in the JES and the Stark shift is larger as indicated by the dashed energy conservation lines in the JES. At least four peaks are now clearly visible in the JES, with the largest one centered at $(E_e, E_N) = (1.28, 0.44)$. The three most visible peaks are more or less along energy conservation lines $E_e + E_N = 1.62, 1.72, 1.85$ (lines not drawn in Fig. 5.1(b)). In the NES, the TDSE result is shifted towards lower E_N , with the magnitude of the shift similar to the case for the lower laser intensity in Fig. 5.1(a). In the PES for moving nuclei, only two peaks are visible, with the highest energy peak in the JES being weighted out from the integration of

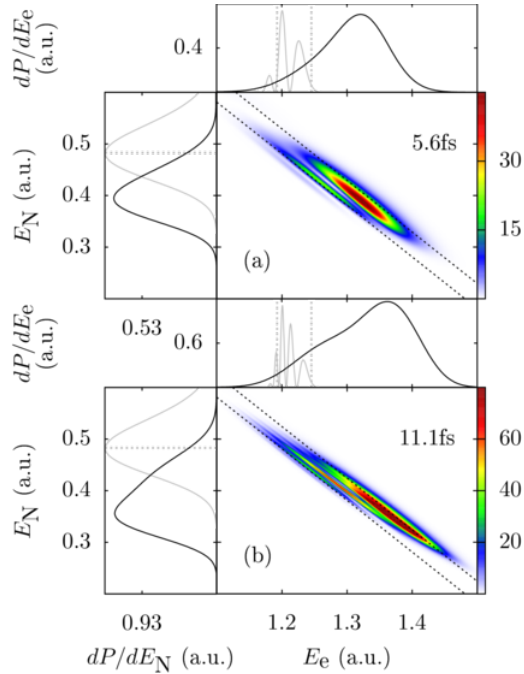


Figure 5.2: As Fig. 5.1, but for pulses with parameters $\omega = 2.278$, $I = 15 \times 10^{17}$ W/cm² and two different pulse durations.

the JES. We therefore stress the importance of the JES: if only the PES and the NKER were at our disposal, no information on the third peak in the JES could be obtained. This extends the conclusion of Refs. [21, 22, 75] to the XUV regime that the JES is a very useful observable.

It should be noted that in Ref. [91], it was suggested that the combination of using small simulation volumes and CAPs placed at the box boundaries would make it impossible to produce the dynamic interference in the PES, and enormously large simulation volumes (radial coordinate up to $r_{\max} = 10000$) were used in their calculations to obtain the PES for hydrogen. However, as shown in Fig. 5.1(b), it is indeed possible to observe interference effects in the JES and PES by using t-SURFF in a small simulation volume $|x| \leq 200$.

Figure 5.2 shows the JES for longer laser pulses $\tau = 5.6$ fs, 11.1 fs, with intensity $I = 15 \times 10^{17}$ W/cm². The increase of the pulse duration has several effects on the JES. Firstly, due to the smaller bandwidth of the laser pulse, the JES in Fig. 5.2 are now narrower compared to the results for the shorter pulses in Fig. 5.1. Secondly, the increase of pulse duration from 5.6 fs in Fig. 5.2(a) to 11.1 fs in Fig. 5.2(b) leads to more interference peaks emerging, similar to the case of dynamic interference in hydrogen [48, 91, 105, 106], but now visible along

the diagonal in the JES. In addition, the JES and NKER for the 5.6 fs pulse in Fig. 5.2(a) are shifted toward smaller E_N values compared to the shorter pulses used in Fig. 5.1, with the peak now located around $E_N = 0.4$ in the NES. For the 11.1 fs pulse in Fig. 5.2(b), a peak is observed around $E_N = 0.36$ in the NES, while a "shoulder" structure is seen around $E_N = 0.42$. When we compare the PES results for moving nuclei to the corresponding fixed nuclei results in Fig. 5.2, the PES for moving nuclei has its dynamic interference peaks completely smeared out, with no interference patterns visible. Furthermore, the PES for moving nuclei in Fig. 5.2(b) peaks at $E_e = 1.31$, a clear shift with respect to the fixed nuclei peaks around $E_e = 1.21$. Thus, due to the inclusion of the nuclear degree of freedom, the fixed nuclei results for the PES are completely wrong. This again stresses the importance of using the JES for the detection of dynamic interference in molecules.

5.2 Analysis of the JES

We will now analyze the structures in the spectra of Figs. 5.1 and 5.2, using two methods.

5.2.1 Essential states expansion

In the first analysis we follow Ref. [48] and extend it to the molecular case of H_2^+ by including the nuclear degree of freedom. The molecule-laser interaction is now chosen in the length gauge, with $V_L^{\text{LG}} = \beta^{\text{LG}} x F(t)$. The electric field is chosen on the form $F(t) = F_0 g(t) \cos(\omega t)$, $g(t)$ a Gaussian envelope.

The wave function is first expanded in terms of the "essential" states consisting of the initial state and the continuum eigenstates of the field-free Hamiltonian

$$|\Psi(t)\rangle = c_0(t) |\Psi_0\rangle e^{-iE_0 t} + \sum_P \int dE_e \int dE_N c_{E_e, E_N}^P(t) |u_{E_e, E_N}^P\rangle e^{-i\omega t}, \quad (5.3)$$

where $|u_{E_e, E_N}^P\rangle$ is a field-free continuum state of H_2^+ with parity P ("e" for even, "o" for odd), electronic continuum energy E_e and nuclear continuum energy E_N . The latter states are obtained in the BO approximation by the method outlined in the Appendix B. Inserting Eq. (5.3) into the TDSE and projecting onto the "essential" states, we arrive at the coupled differential equations:

$$i\dot{c}_0(t) = \int dE_e \int dE_N \left[\frac{1}{2} d_{E_e, E_N}^{0*} F_0 \right] g(t) e^{iE_0 t} c_{E_e, E_N}^o(t) \quad (5.4a)$$

$$i\dot{c}_{E_e, E_N}^o(t) = \left[\frac{1}{2} d_{E_e, E_N}^o F_0 \right] g(t) e^{-iE_0 t} c_0(t) + (E_e + E_N - \omega) c_{E_e, E_N}^o(t), \quad (5.4b)$$

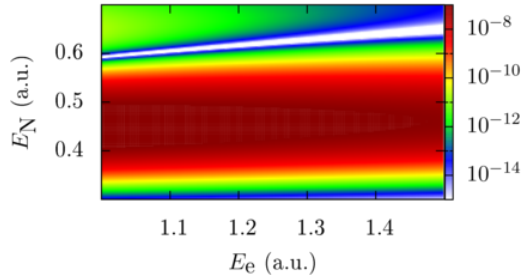


Figure 5.3: The transition dipole matrix element squared $|d_{E_e, E_N}^o|^2 = |\langle u_{E_e, E_N}^o | x | \Psi_0 \rangle|^2$ [see the discussion of Eq. (5.4)].

where $d_{E_e, E_N}^P = \langle u_{E_e, E_N}^P | x | \Psi_0 \rangle$ is the transition dipole matrix element. In obtaining Eq. (5.4), we have used the RWA and the fact that the initial state $|\Psi_0\rangle$ has even parity. Furthermore, we have neglected the continuum-continuum couplings. The solution to Eq. (5.4b) is given by

$$c_{E_e, E_N}^o(t) = -i \left[\frac{1}{2} d_{E_e, E_N}^o F_0 \right] e^{-i(\delta + E_0)t} \int_{-\infty}^t c_0(t') g(t') e^{i\delta t'} dt', \quad (5.5)$$

where

$$\delta = E_e + E_N - \omega - E_0 \quad (5.6)$$

is the detuning. The JES is then

$$\frac{\partial^2 P}{\partial E_e \partial E_N} = |c_{E_e, E_N}^o(T)|^2 \quad (5.7)$$

with $T \gg \tau$.

We see from Eqs. (5.5) and (5.7) that in the present model, the structure of $|d_{E_e, E_N}^o|^2$ will determine the structure of the JES. The former is plotted in Fig. 5.3. The highest-density region is located along $E_N = 0.45$, immediately explaining the peaks in the JES and NKER of Fig. 5.1(a). Furthermore, a valley of zero density is seen in Fig. 5.3, explaining the minima in Fig. 5.1(a) located around $(E_e, E_N) = (1.1, 0.6)$ in the JES. However, Fig. 5.3 does not explain the structures in Fig. 5.1(b), where the peak in the NKER is still at $E_N = 0.45$, but instead of a minimum at $E_N = 0.60$, there is now a local maximum.

To calculate the JES using Eq. (5.7), we need to solve the coupled differential equations in Eq. (5.4). These equations can be decoupled by following the procedure of Refs. [48, 105]. First, if $c_0(t')g(t')$ in Eq. (5.5) varies slowly compared to the rest of the integrand, it can be taken out of the integral and evaluated at time t . This approximation will be referred to as the local approximation. By

evaluating Eq. (5.5), plugging the result into Eq. (5.4a) and solving the resulting uncoupled differential equation, we obtain $c_0(t)$ on the form

$$c_0(t) \cong e^{-(i\Delta + \Gamma/2)J(t)}, \quad (5.8)$$

where Δ is the Stark shift, Γ the ionization rate, and

$$J(t) = \int_{-\infty}^t g^2(t') dt'. \quad (5.9)$$

As noted in Refs. [48, 105], Δ is difficult to calculate and also depends on the "non-essential" states which were omitted in the present model. We therefore follow the procedure proposed in Ref. [105] and extract Δ from the TDSE calculations by employing Eq. (5.1) and use it in Eq. (5.8). The Stark shift obtained in this way is beyond the RWA. The expression for Γ obtained in the derivation of Eq. (5.8) is

$$\Gamma = 2\pi \int dE_e \int dE_N \left| \frac{d_{E_e, E_N} F_0}{2} \right|^2 \delta(E_0 + \omega - E_e - E_N). \quad (5.10)$$

Note that Eq. (5.10) can also be obtained using Fermi's golden rule. Compared with the previous works on atoms [48, 105], Γ now contains an extra integral over the nuclear kinetic energy, with the energies related by $E_e + E_N = E_0 + \omega$. For the laser pulse used in Fig. 5.1(a), the survival probability of the ground state in the present model is

$$P_0^{\text{model}}(\infty) = |c_0(\infty)|^2 = e^{-\Gamma J(\infty)} = 0.978, \quad (5.11)$$

which is comparable to the TDSE result $P_0^{\text{TDSE}} = 0.975$. This demonstrates that the approximation (5.10) is not too bad, at least for the intensity used in Fig. 5.1(a).

We may insert the approximation for $c_0(t)$ given by Eq. (5.8) into Eq. (5.5) to obtain an approximate formula for the JES in the local approximation:

$$\frac{\partial^2 P}{\partial E_e \partial E_N} \cong \left| \frac{1}{2} d_{E_e, E_N}^o F_0 \int_{-\infty}^T g(t') e^{-\Gamma/2 J(t') + i\Phi(t')} dt' \right|^2, \quad (5.12)$$

with

$$\Phi(t) = \delta t - \Delta J(t). \quad (5.13)$$

It should be noted that because $c_0(t)$ of Eq. (5.8) was obtained in the local approximation, Eq. (5.12) also only works in this approximation, a point we will come back to below. Figures 5.4(a) and 5.4(b) show the JES, calculated using Eq. (5.12), and their corresponding PES and NES, for two different pulse durations (same laser parameters as in Fig. 5.2). In the JES of Fig. 5.4(a), two peaks

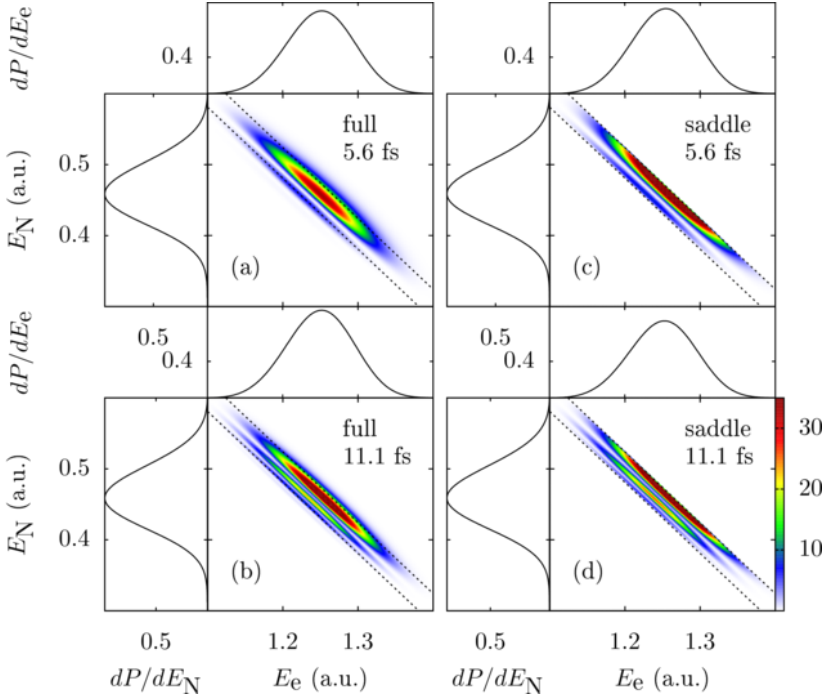


Figure 5.4: Panels (a) and (b): JES calculated using the approximation (5.12) (denoted by “full” in the panels). Panels (c) and (d): JES calculated using the saddle-point approximation (5.14) (denoted by “saddle” in the panels). Laser parameters are the same as in Fig. 5.2, i.e. $\omega = 2.278$, $I = 24 \times 10^{17}$ W/cm² and two different pulse durations τ displayed in the figure. The magnitude of the spectra are in arbitrary units. The left and right dashed diagonal lines correspond to $\delta = 0$ and $\delta = \Delta$, respectively.

are clearly visible, with a large peak located along $E_e + E_N = 1.71$ and a smaller one along $E_e + E_N = 1.68$. This is in agreement with the results for the full TDSE calculation shown in Fig. 5.2(a), where we also had two clearly visible peaks along the same mentioned diagonals. However, in the present model where the ground state is assumed to be the only bound state, the norm-squared of the dipole matrix element $|d_{E_e, E_N}^0|^2$ restricts the NKER to be centered around $E_N = 4.5$, in disagreement with Fig. 5.2(a). In the JES of Figure 5.4(b), three peaks are now visible, along the diagonal lines $E_e + E_N = 1.68, 1.69, 1.71$. The number of peaks and diagonal positions of these peaks are in agreement with the full TDSE result in Fig. 5.2(b). The spectrum is again incorrectly centered around $E_N = 4.5$, due to $|d_{E_e, E_N}^0|^2$ and the insufficient description of the nuclear degree of freedom.

To gain more physical insight into the structures of the JES in Figs. 5.4(a) and 5.4(b), we have evaluated Eq. (5.12) using the saddle-point approximation and in this way obtained an approximate expression for the JES (see Refs. [48, 105] for

the a similar expression for the PES in the atomic case):

$$\begin{aligned} \frac{\partial^2 P}{\partial E_e \partial E_N} &\propto \left| \frac{d_{E_e, E_N}^0 F_0}{2} \sum_{t=\pm t_s} \frac{g(t)}{\sqrt{|\ddot{\Phi}(t)|}} e^{-\Gamma/2 J(t)} e^{i[\Phi(t)+\zeta(t)]} \right|^2 \\ &\propto \left| \frac{d_{E_e, E_N}^0 F_0 \tau}{2\sqrt{\Delta t_s}} \right|^2 \left\{ e^{-\Gamma J(-t_s)} + e^{-\Gamma J(t_s)} \right. \\ &\quad \left. + 2e^{-\Gamma/2[J(-t_s)+J(t_s)]} \cos[K(\delta)] \right\}, \end{aligned} \quad (5.14)$$

with

$$K(\delta) = -2\delta t_s - \Delta(J(-t_s) - J(t_s)) - \pi/2. \quad (5.15)$$

In Eqs. (5.14) and (5.15), $\zeta(\pm t_s) = \pm\pi/4$; $J(t)$ is given by Eq. (5.9); and $\pm t_s$ are the saddle points with

$$t_s = \frac{\tau}{2} \sqrt{\frac{\ln(\Delta/\delta)}{2 \ln(2)}} \quad (5.16)$$

satisfying the stationary-phase condition

$$\dot{\Phi}(\pm t_s) = \delta - \Delta g^2(\pm t_s) = 0. \quad (5.17)$$

The JES calculated using the saddle-point expression (5.14) are shown in Figs. 5.4(c) and 5.4(d). Comparing these results with Figs. 5.4(a) and 5.4(b), it is seen that the saddle-point approximation captures the essential features of the JES calculated using the full time-integral (5.12): the number of peaks perpendicular to the diagonal, the positions of the peaks, and the relative intensities of the peaks are qualitatively similar to the results of the full calculation. From the stationary-phase condition (5.17) and the definition of $g(t)$ in Eq. (2.7a), it is seen that for a saddle point to exist, the detuning must belong to the interval $\delta \in [0, \Delta]$. For δ lying in this interval, $K(\delta)$ is a monotonically decreasing function, as $dK/d\delta = -2\delta \leq 0$. Furthermore, $K(0) = \Delta J(\infty) - \pi/2$ and $K(\delta) = -\pi/2$. The total accumulated phase of the cosine in Eq. (5.14) is thus $\Delta J(\infty) = \sqrt{\pi/(8 \ln 2)} \Delta \tau \equiv 2\pi k$, with k corresponding to the number of oscillations. For $\tau = 5.6$ fs the accumulated phase is $1.19 \times 2\pi$ while for $\tau = 11.1$ fs it is $2.38 \times 2\pi$. These numbers are indeed in qualitative agreement with the JES of Figs. 5.4(c) and 5.4(d), where slightly more than one oscillation and slightly more than two oscillations are visible, respectively. At $\Delta = \delta$, the saddle point is $t_s = 0$, and the approximation for the JES in Eq. (5.14) diverges. This divergence is seen in Fig. 5.4 as the discrepancy between the “full” results and the “saddle” results near the right dashed lines corresponding to $\Delta = \delta$. We have thus demonstrated that the interference patterns in the JES are indeed due to the dynamic Stark effect, where two contributions to the same energy pair (E_e, E_N) in the JES coherently superimpose. Figure 5.4

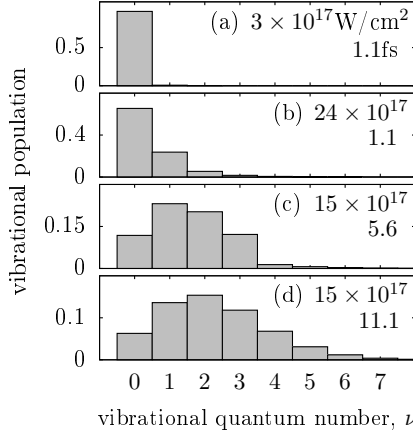


Figure 5.5: Vibrational distributions at the end of the laser pulses, for the laser parameters used in Figs. 5.1 and 5.2.

again confirmed that the introduction of a nuclear degree of freedom makes the dynamic interference effect completely invisible in the PES.

We now discuss the two main deficiencies in the present model. The first one is the neglect of the excited vibrational states in the expansion of Eq. (5.3), which could have been populated during the pulse by impulsive Raman-type transitions from the ground vibrational state. The vibrational populations of the first few vibrational states at the end of the laser pulse are shown in Fig. 5.5. For the short pulses considered in Figs. 5.5(a) and 5.5(b), the population is predominantly in the vibrational ground state, and the expansion in Eq. (5.3) is expected to be a good approximation. However, for the high intensity pulse with $I = 24 \times 10^{17} \text{ W/cm}^2$, the variation of $c_0(t')g(t')$ in Eq. (5.5) is comparable to the rest of the integrand, and the local approximation cannot be applied. As a result, the approximation for the JES in Eqs. (5.12) and (5.14) will fail. For the longer pulses, the local approximation is expected to work well. However, the pulse energy of the laser is much greater, meaning that much stronger Raman couplings and thus much greater population of excited vibrational states is observed, as shown in Figs. 5.5(c) and 5.5(d). The essential expansion in Eq. (5.3) that neglects the excited vibrational states is thus expected to break down, which is indeed seen to be the case by comparing the results of Figs. 5.2 and 5.4. Although Eq. (5.3) is not expected to work well, the analysis in the present section is still useful, as it provides insight into the structures of the JES in terms of dynamical interference, provided that only the vibrational ground state is populated.

Another deficiency in the present model is the neglect of continuum-continuum couplings. The ponderomotive energy of the most intense pulse used is $U_p =$

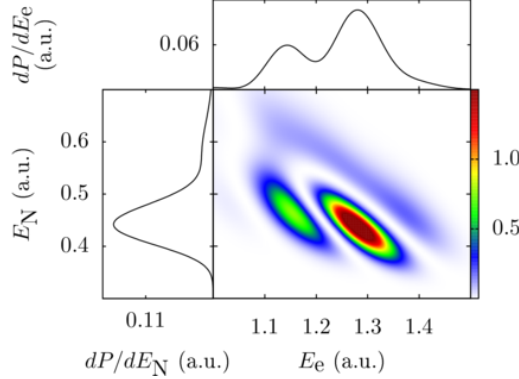


Figure 5.6: JES calculated using Eq. (5.18) for the same laser parameters as in Fig. 5.1(b), $\omega = 2.278$, $\tau = 1.1$ fs and $I = 24 \times 10^{17}$ W/cm².

3.29, larger than the photon energy $\omega = 2.278$. This indicates that multiphoton processes at these intensities cannot be neglected and will contribute to differences in the JES calculated using the present model and the JES obtained from the full TDSE calculations. Such differences were observed in the atomic case [91] in terms of differences in the relative amplitudes of the peaks in the PES.

5.2.2 Reflection method for the JES

In situations where ionization from the initial state is dominant, the JES can be approximated by weighting the fixed nuclei results with the initial vibrational density:

$$\frac{\partial^2 P}{\partial E_e \partial E_N} \propto \frac{|\chi_0(1/E_N)|^2}{E_N^2} \frac{dP}{dE_e}(1/E_N), \quad (5.18)$$

where $dP/dE_e(R)$ is the PES calculated at the fixed internuclear distance R . We refer to this model as the reflection method for the JES. The JES calculated using Eq. (5.18) for the field parameters in Fig. 5.1(b) are shown in Fig. 5.6. There is indeed a good qualitative match, with all structures in the JES of Fig. 5.1(b) accounted for in Fig. 5.6. The reason for this is simple: all of the electron-laser couplings are included in $dP/dE_e(R)$ of Eq. (5.18), while there are minimal populations of higher excited vibrational states (see Fig. 5.5).

For the longer pulses considered in Fig. 5.2 there is significant vibrational excitation during the pulse, as shown in Figs. 5.5(c) and 5.5(d), and the approximation leading to Eq. (5.18) is not valid. This is indeed verified by comparing Fig. 5.7 with Fig. 5.2(a), where in Fig. 5.2(a) the JES is shifted towards lower E_N . Notice that we have solved the TDSE exactly at fixed internuclear distances in the present approximation, meaning that the electronic continuum-continuum

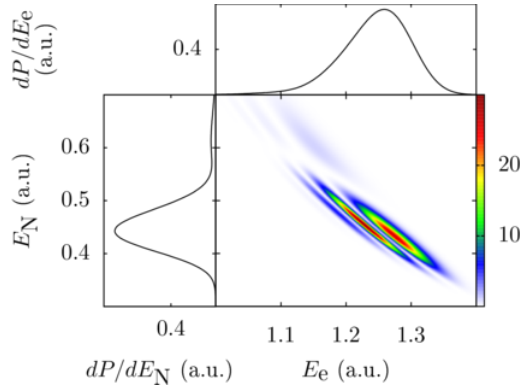


Figure 5.7: JES calculated using Eq. (5.18) for the same laser parameters as in Fig. 5.1(a), $\omega = 2.278$, $\tau = 5.6$ fs and $I = 15 \times 10^{17}$ W/cm².

couplings neglected in the "essential states" model from Sec. 5.2.1 are included here.

The shift towards lower nuclear energies in the JES of Fig. 5.2 compared to Fig. 5.1 is due to the excited vibrational populations, which can be shown qualitatively using the simple reflection principle (5.2). In Fig. 5.8, results of Eq. (5.2) for the lowest four vibrational states are plotted. For the $\tau = 5.6$ fs pulse in Fig. 5.2(a), the most populated vibrational state at the end of the pulse is $\nu = 1$. In Fig. 5.8, reflection result for $\nu = 1$ has the large peak at $E_N = 0.408$, thus explaining the peak in the NKER of Fig. 5.2(a) at around $E_N = 0.408$. Similarly, for the $\tau = 11.1$ fs pulse in Fig. 5.2(b), the most populated vibrational state is $\nu = 2$, which in Fig. 5.8 has the largest peak located at $E_N = 0.366$, explaining the the peak in the NKER of Fig. 5.2(b) at around $E_N = 0.36$. The shoulder structure in the NKER of Fig. 5.2(b) at around $E_N = 0.42$ can be interpreted as resulting from the $\nu = 1$ state.

5.3 Conclusion

We investigated dissociative ionization of H_2^+ using intense, femtosecond XUV laser pulses. Distinct interference structures in the JES were observed as the laser intensity is increased. The "essential" states model was able to relate the interference structures to the Dynamics interference effect. The PES and NKER were shown to be inadequate for the observation of the dynamic interference effect in H_2^+ , stressing the importance of the JES.

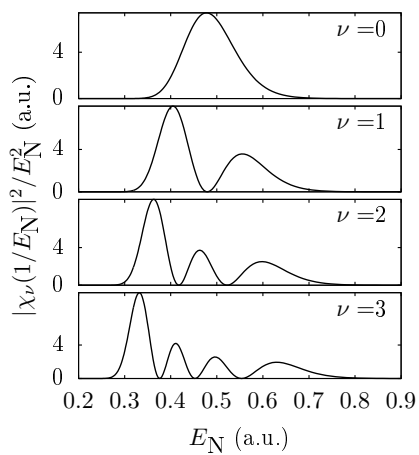


Figure 5.8: Reflection results [Eq. (5.2)] for the lowest four vibrational states.

CHAPTER 6

MOLECULAR BREAKUP IN THE VERY INTENSE XUV REGIME

There has recently been a renewed interest [113–115] in the laser parameter regime known as the stabilization regime [49, 50], where the ionization rate does not necessarily increase with increasing laser intensities. The effect usually requires the photon energy to be larger than the ionization potential, and experimental evidence for the effect has not yet been observed in the XUV regime, most due to the lack of laser systems with the required intensities. With the new laser sources, such an observation could soon be possible. Theoretical investigations on the stabilization effect have mostly been on atoms or molecules in the FNA, probably due to the intuitive assumption that when the laser frequency is larger than the ionization potential, $\omega > I_p$, the dissociation channels will be so far off-resonance with the one-photon absorption that they will never contribute to the breakup dynamics. In this chapter, we will show that while molecules stabilize w.r.t. ionization, they do not necessarily stabilize w.r.t. dissociation. A theoretical model is proposed to explain the observations, as well as predicting the control of the breakup dynamics.

6.1 TDSE results

We propagate the TDSE with a time step of $\Delta t = 0.005$. The box size is defined as $|x| \leq 100$ and $R \leq 80$ with grid spacings $\Delta x = 0.391$ and $\Delta R = 0.0781$. The ground state energy is $E_0 = -0.597$, dissociation limit $E_d = -0.5$, equilibrium internuclear distance $R_0 = 2.064$, and ionization potential $I_p = 1.1$ at R_0 . We work in VG, with the pulse envelope chosen to be of a Gaussian form. All pulses used in this chapter satisfy the non-relativistic criteria $2U_p/c^2 \ll 1$ [108, 116] and

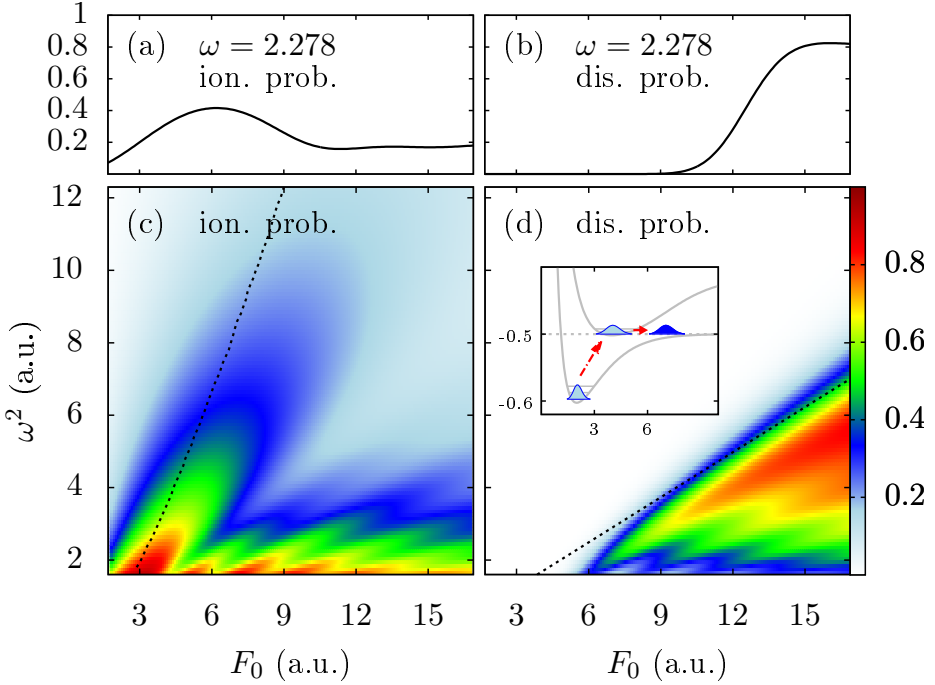


Figure 6.1: Continuum probabilities for H_2^+ interacting with intense laser pulses containing 100 cycles, corresponding to $\tau = 2.1 - 15.8$ fs. (a) and (b) DI and dissociation probabilities for $\omega = 2.278$, (c) and (d) DI and dissociation probabilities for different ω^2 and F_0 . The dashed line in (c) traces the position of the largest DI rate, calculated from HFFT (see text). The dashed, straight line in (d) corresponds to $\alpha_0 = F_0/\omega^2 = 2.41$. The inset in (d) shows the nuclear dynamics for pulse parameters tracing this line (see Fig. 6.4 and the accompanying discussion).

the dipole condition $U_p/2\omega c \ll 1$ [117], with $U_p = F_0^2/4\omega^2$ the ponderomotive potential.

We obtain the total continuum probability from the TDSE calculations by $P_{\text{tot}} = 1 - P_{\text{b}}$, with the bound probability P_{b} obtained at the end of the pulse by projection onto bound states of H_2^+ . The ionization probability is calculated as $P_{\text{ion}} = 1 - P_{\text{box}}$, with P_{box} the norm at T in the spatial region $|x| \leq 60$, $R \leq 70$. For all pulse parameters considered, the dissociative WPs, moving on a much slower time-scale than the ionized wave packets, are inside the box region at T . The dissociation probability is finally calculated as $P_{\text{dis}} = P_{\text{tot}} - P_{\text{ion}}$.

Fig. 6.1(a) shows the DI probability P_{ion} of H_2^+ by pulses with $\tau = 11.1$ fs and $\omega = 2.278$. P_{ion} increases with F_0 for lower amplitudes until it reaches a maximum at $F_0 \simeq 6.2$, whereafter it decreases. The latter behavior indicates stabilization with respect to DI [49]. Figure 6.1(b) shows the dissociation probability P_{dis} . For the lower values of F_0 , no dissociation is observed as expected from perturbation

theory. At $F_0 \simeq 9$, dissociation sets in, increasing with F_0 , until it “saturates” at $F_0 \simeq 15$.

A complete picture is drawn in Figs. 6.1(c) and 6.1(d), which show P_{ion} and P_{dis} , respectively, as functions of F_0 and ω^2 . For fixed ω the suppression of DI for large F_0 is evident [Fig. 6.1(c)]. Lobes corresponding to large P_{ion} are seen emanating from the origin. The dashed line traces the largest high-frequency Floquet theory (HFFT) [118] rate, in reasonable agreement with the TDSE result. A version of the HFFT generalized to include the nuclear degree of freedom is described in the next section. The oscillatory behavior in P_{ion} was discussed for reduced-dimensionality atomic systems [49, 119, 120], and was attributed to the two-center character of dressed the atomic wave function. In the case of P_{dis} in Fig. 6.1(d), appreciable dissociation is observed for pulses with $\alpha_0 = F_0/\omega^2 \geq 2.41$ indicated by the dashed line. In this regime, $P_{\text{ion}} + P_{\text{dis}} = 1$, implying unity probability for breakup. The remnants of the lobes from DI are present in Fig. 6.1(d), an indication of the different time scales for DI and dissociation processes: DI occurs during the pulse, and what is not ionized, dissociates after the pulse. The physics of the dashed line is explained in the next section.

6.2 High-frequency Floquet theory

To understand the TDSE results, we apply the HFFT [49], which is here extended to include the nuclei motion.

6.2.1 Kramers-Henneberger frame

Starting from the TDSE

$$i \frac{\partial}{\partial t} \Psi(x, R, t) = [T_e + T_N + V_{eN}(x, R) + V_L(t)] \Psi(x, R, t), \quad (6.1)$$

and applying the unitary transformation

$$\Psi(x, R, t) = \exp(-\beta\alpha(t)d/dx) \Psi^{KH}(x, R, t) \quad (6.2)$$

with the quiver motion $\alpha(t) = \int^t A(t')dt'$, the Kramers-Henneberger (KH) frame TDSE is obtained:

$$i \frac{\partial}{\partial t} \Psi^{KH}(x, R, t) = [T_e + T_N + V_{eN}(x + \beta\alpha(t), R)] \Psi^{KH}(x, R, t). \quad (6.3)$$

Consider first a monochromatic field, with $A(t) = (F_0/\omega) \cos(\omega t)$, $\alpha(t) = \alpha_0 \sin(\omega t)$, and $\alpha_0 = F_0/\omega^2$. The periodic potential allows the Floquet ansatz for $\Psi^{KH}(x, R, t)$

and the Fourier expansion of $V_{eN}(x + \beta\alpha(t), R)$ in the KH TDSE:

$$\begin{aligned}\Psi^{KH}(x, R, t; \alpha_0) &= e^{-iE(\alpha_0)t} \sum_{n=-\infty}^{\infty} \phi_n(x, R; \alpha_0) e^{in\omega t} \\ V_{eN}(x + \beta\alpha(t)) &= \sum_{n=-\infty}^{\infty} V_n(x, R; \alpha_0) e^{in\omega t}\end{aligned}\tag{6.4}$$

with the parametric dependency on the quiver amplitude α_0 is explicitly stated, and with the Fourier components given by

$$V_n(x, R; \alpha_0) = (\omega/2\pi) \int_0^{2\pi/\omega} V_{eN}(x + \beta\alpha(t), R) e^{-in\omega t} dt.\tag{6.5}$$

The resulting coupled differential equations

$$[H_0(x, R; \alpha_0) - E(\alpha_0) - n\omega] \phi_n(x, R; \alpha_0) = - \sum_{m \neq n} V_{n-m}(x, R; \alpha_0) \phi_m(x, R; \alpha_0),\tag{6.6}$$

with $H_0(x, R; \alpha) \equiv H_e(x, R; \alpha_0) + T_N$ and $H_e(x, R; \alpha_0) = T_e + V_0(x, R; \alpha_0)$, can be treated in the framework of HFFT, where $E(\alpha_0)$ and $\phi_n(x, R; \alpha_0)$ are expanded in terms of contributions of increasing orders in ω^{-1} .

6.2.2 Structure equation

To zeroth-order, corresponding to $\omega \rightarrow \infty$ at fixed α_0 , Eq. (6.6) reduces to the structure equation [49, 121]

$$H_0(x, R; \alpha) u(x, R; \alpha_0) = W(\alpha_0) u(x, R; \alpha_0),\tag{6.7}$$

with $W(\alpha_0)$ and $u(x, R; \alpha_0)$ being the zeroth order approximations to $E(\alpha_0)$ and $\phi_0(x, R; \alpha_0)$, respectively. The Hamiltonian in Eq. (6.7) is Hermitian, which implies that W is real and no ionization occurs to first order in HFFT. Equation (6.7) is solved in the BO approximation. For the bound states, it is assumed

$$u_{i,\nu}(x, R; \alpha_0) = \xi_i(x; R, \alpha_0) \chi_\nu(R; \alpha_0),\tag{6.8}$$

with electronic states $\xi_i(x; R, \alpha_0)$ and nuclear vibrational states $\chi_\nu(R; \alpha_0)$ satisfying

$$\begin{aligned}H_e(x; R, \alpha_0) \xi_i(x; R, \alpha_0) &= V_{el,i}(R, \alpha_0) \xi_i(x; R, \alpha_0) \\ [T_N + E_{el,i}(R; \alpha_0)] \chi_\nu(R; \alpha_0) &= W_{i,\nu}(\alpha_0) \chi_\nu(R; \alpha_0),\end{aligned}\tag{6.9}$$

where $V_{el,i}$ and $W_{i,\nu}$ are the field-dressed BO potential curves and eigenenergies, respectively.

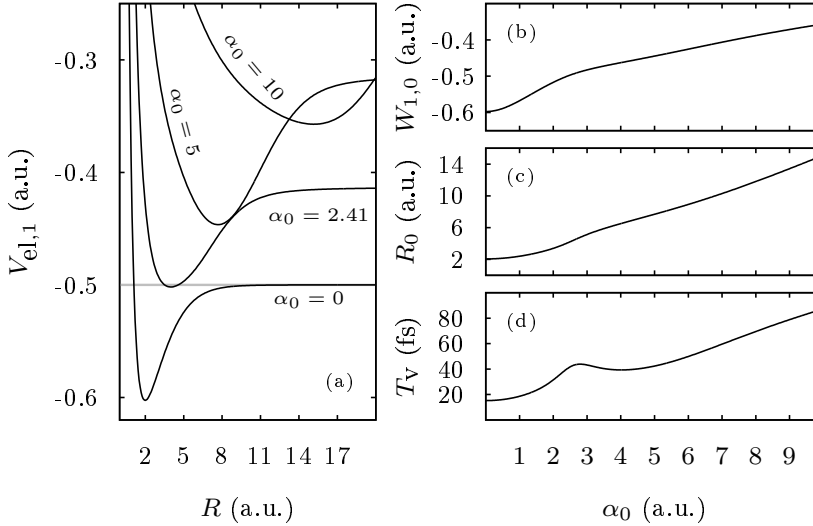


Figure 6.2: (a) field-dressed ground BO curves $V_{el,1}(R, \alpha_0)$, with the dashed line showing the field-free dissociation limit. (b) field-dressed ground state energy $W_{1,0}$, (c) internuclear distance $R_0 \equiv \langle u_{1,0} | R | u_{1,0} \rangle$, and (d) vibrational timescale $T_v \equiv 2\pi/(W_{1,1} - W_{1,0})$, as functions of α_0 .

Figure 6.2 shows $V_{el,1}(R, \alpha_0)$, $W_{1,0}(\alpha_0)$, the equilibrium internuclear distance $R_0(\alpha_0) \equiv \langle u_{1,0}(\alpha_0) | R | u_{1,0}(\alpha_0) \rangle$ and the vibrational time scale $T_v(\alpha_0) \equiv 2\pi/[W_{1,1}(\alpha_0) - W_{1,0}(\alpha_0)]$, as functions of α_0 . With increasing α_0 , the BO curve is shifted upwards in energy, towards greater R , and becomes gradually shallower, which imply the increase of $W_{1,0}(\alpha_0)$, $R_0(\alpha_0)$, and $T_v(\alpha_0)$. The generality of such observations for diatomic molecules in the small- α_0 limit is discussed in Appendix C.

6.2.3 HFFT rates

The unbound solutions to Eq. (6.7) is chosen on the form $u_{E_e E_N}^P(x, R; \alpha_0) = \xi_{E_e}^P(x, R; \alpha_0) \chi_{E_N}(R; \alpha_0)$, satisfying

$$\begin{aligned} \left[H_e(x; R, \alpha_0) - \frac{1}{R} \right] \xi_{E_e}^P(x; R, \alpha_0) &= E_e \xi_{E_e}^P(x; R, \alpha_0) \\ \left[T_N + \frac{1}{R} \right] \chi_{E_N}(R; \alpha_0) &= E_N \chi_{E_N}(R; \alpha_0), \end{aligned} \quad (6.10)$$

with P denoting the parity, and E_e (E_N) the electronic (nuclear) kinetic energy. A numerical method that can be used to solve these equations were presented in Appendix B.

For finite ω , the energy gains an imaginary term, $E(\alpha_0) = \text{Re}[E(\alpha_0)] - i\Gamma(\alpha_0)/2$, with $\Gamma(\alpha_0)$ the ionization rate. In first-order HFFT the total rate

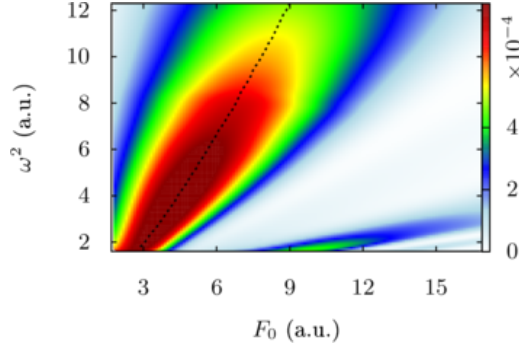


Figure 6.3: One-photon ionization rate Γ_1 as a function of F_0 and ω^2 . The dashed line traces the maximum of the largest “lobe”.

is

$$\Gamma(\alpha_0) = \sum_{m \neq 0} \Gamma_m(\alpha_0), \quad (6.11)$$

with the m -photon rate

$$\Gamma_m(\alpha_0) = 2\pi \langle u_{1,0}(\alpha_0) | V_{-m}(\alpha_0) \quad (6.12)$$

$$\times \delta[W_{1,0}(\alpha_0) + m\omega - H_0(\alpha_0)] V_m(\alpha_0) | u_{1,0}(\alpha_0) \rangle \quad (6.13)$$

$$= \sum_P \int dE_e \int dE_N \frac{\partial^2 \Gamma_m^P(\alpha_0)}{\partial E_e \partial E_N}, \quad (6.14)$$

and

$$\begin{aligned} \frac{\partial^2 \Gamma_m^P(\alpha_0)}{\partial E_e \partial E_N} &= 2\pi | \langle u_{E_e, E_N}^P(\alpha_0) | V_m(\alpha_0) | u_{1,0}(\alpha_0) \rangle |^2 \\ &\times \delta(W_{1,0}(\alpha_0) + m\omega - E_e - E_N). \end{aligned} \quad (6.15)$$

To obtain Eq. (6.14), the identity

$$1 = \sum_{i,\nu} |u_{i,\nu}(\alpha_0)\rangle \langle u_{i,\nu}(\alpha_0)| + \sum_P \int dE_e \int dE_N |u_{E_e, E_N}^P(\alpha_0)\rangle \langle u_{E_e, E_N}^P(\alpha_0)|. \quad (6.16)$$

was inserted. For the ω 's considered here, we checked that $\Gamma(\alpha_0) \simeq \Gamma_1(\alpha_0)$.

Figure 6.3 shows $\Gamma_1(\alpha_0)$ as a function of F_0 and ω^2 . The dashed line traces the largest “lobe” corresponding to the largest ionization rate, which is also plotted in the TDSE results of Fig. 6.1(c). The deviation of this line from the largest “lobe” in Fig. 6.1(c) is partly due to Γ being the rate calculated for a monochromatic field. A pulse with a smooth turn-on and α_{\max} at the field maximum, will sweep through all intermediate values of quiver amplitudes $0 < \alpha_0 < \alpha_{\max}$. For this reason the “lobe” in Fig. 6.1 is shifted towards higher F_0 compared to the line tracing the ionization rate.

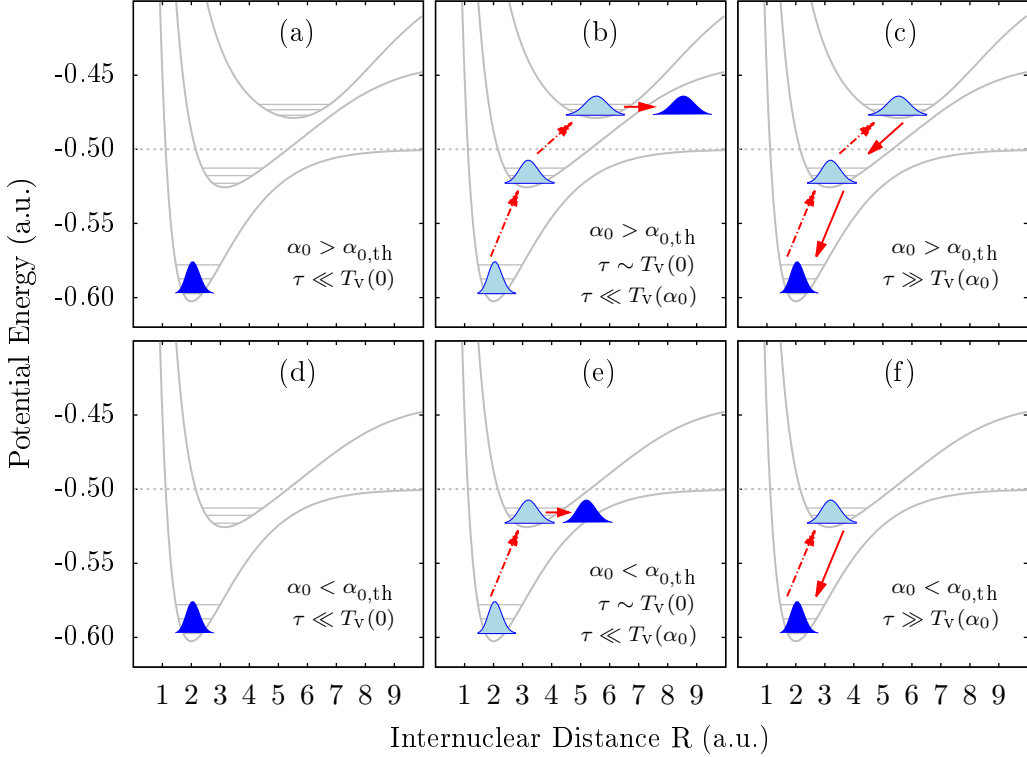


Figure 6.4: Schematic of the nuclear dynamics in the KH frame for different α_0 and τ . For (a)-(c), $\alpha_0 = 3.25$, and for (d)-(f), $\alpha_0 = 1.87$. In each panel, from bottom to top, the lowest field-dressed BO curve is shown for different times corresponding to $\alpha_0(t) = 0, 1.87$, (and 3.25). The lowest three field-dressed vibrational levels are indicated. The horizontal lines indicate E_d . The arrows sketch the pathways of the vibrational WP during the turn-on and -off of the pulse. The final position of the WP after the pulse is shown in dark blue.

6.3 Physical model based on HFFT

For pulsed laser fields, we let the maximal quiver amplitude vary with the field envelope, $\alpha_0 \rightarrow \alpha_0(t) \equiv \alpha_0 g(t)$. The lowest BO curve is plotted in Fig. 6.4 for $\alpha_0(t) = 0, 1.87$ and 3.25 . In accordance with the last section, $W_{1,0}(\alpha_0(t))$, $R_0(\alpha_0(t))$, and $T_v(\alpha_0(t))$ all increase with $\alpha_0(t)$.

A qualitative model of the dissociation mechanism is now presented, which will be validated later by TDSE calculations. Let τ be the time scale for the turn-on (and -off) of the laser pulse, and $\alpha_{0,th}$ satisfy $W_{1,0}(\alpha_{0,th}) = E_d$, i.e. the quiver amplitude at which the dressed ground state equals the dissociation limit

[inset of Fig. 6.1(d)]. Provided the pulse satisfies

- (i) $\alpha_0 > \alpha_{0,th}$
- (ii) $T_v(0) \sim \tau$
- (iii) $T_v(\alpha_0) \gg \tau$

the dissociation process occurs as follows (illustrated in Fig. 6.4(b)). During the turn-on of the pulse, (ii) ensures the population to follow the field-dressed ground state adiabatically. At the field maximum, (i) implies that the bound WP populates dressed eigenstates with energies greater than E_d . Due to (iii), the turn-off of the pulse can be considered sudden, and the nuclear WP does not feel the fast change of the electronic potential, leaving its position and energy unchanged. After the pulse, the nuclear WP is trapped above E_d , resulting in dissociation via the field-free electronic ground state, with NKER given by $E_N(\alpha_0) = W_{1,0}(\alpha_0) - E_d$.

The laser field regime for which P_{dis} is nonzero in the TDSE calculations of Fig. 6.1(d) satisfies (i)-(iii). For H_2^+ , we have $\alpha_{0,th} = 2.41$, $T_v(0) = 15.2$ fs and $T_v(\alpha_{0,th}) = 41.7$ fs. In Fig. 6.1(d), the onset of dissociation is indeed around the dashed line corresponding to $\alpha_0 = \alpha_{0,th}$. This agreement supports the physical model. The frequency range $\omega^2 = 2 - 8$ in Fig. 6.1(d) where P_{dis} is nonzero corresponds to $\tau = 9.0 - 17.9$ fs, which fulfills condition (ii) at least approximately. For $\alpha_0 > \alpha_{0,th}$, we have $\tau \ll T_v(\alpha_{0,th}) < T_v(\alpha_0)$, and condition (iii) is satisfied as well. DI occurs throughout the whole duration of the pulse due to higher-order Floquet components in $V_{eN}(x + \beta\alpha(t), R)$. In the stabilization regime, DI is greatly suppressed, leaving the population trapped above E_d to dissociate. This explains $P_{\text{ion}} + P_{\text{dis}} = 1$ in the parameter regime of Fig. 6.1(d) where P_{dis} is nonzero.

Figures 6.4(a) and (c) illustrate the cases for which (i) is satisfied, but (ii) and (iii) are not. In the case where the pulse duration is short, $\tau \ll T_v(0)$, the perturbation can be considered sudden, and the initial population is unaffected, resulting in no dissociation [Fig. 6.4(a)]. For long pulses $\tau \gg T_v(\alpha_0)$, the adiabatic approximation is accurate, and the initial state follows the dressed ground state throughout the whole pulse resulting in a final bound distribution similar to the initial population [Fig. 6.4(c)]. For the case where (ii) and (iii) are satisfied, but with $\alpha_0 < \alpha_{0,th}$, no dissociation occurs. Instead, an excited vibrational WP is created containing field-free vibrational states with quantum numbers ν satisfying $W_{1,\nu}(0) = W_{1,0}(\alpha_0)$ [Fig. 6.4(e)].

The qualitative physical model is validated by TDSE calculations. Figure 6.5 shows P_{ion} , P_{dis} and $P_{\text{ion}} + P_{\text{dis}}$ for $\omega = 2.278$ and different pulse durations N_c as

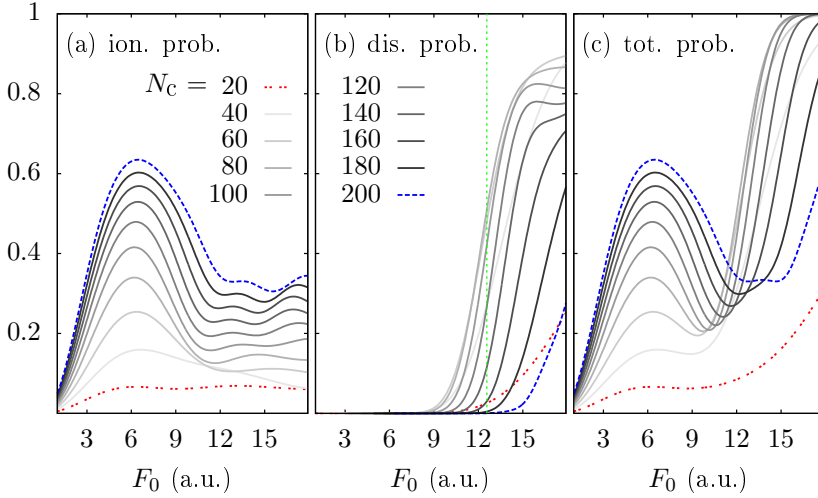


Figure 6.5: (a) Ionization P_{ion} , (b) dissociation P_{dis} , and (c) continuum probabilities $P_{\text{ion}} + P_{\text{dis}}$ for $\omega = 2.278$ and different pulse durations as a function of F_0 . The dotted vertical line indicates the F_0 corresponding to the onset of dissociation at $\alpha_{0,th} = 2.41$ (see text).

a function of F_0 . While P_{ion} in Fig. 6.5(a) increases with N_c for a fixed F_0 , P_{dis} in Fig. 6.5(b) behaves differently. For $N_c = 20$ ($\tau = 2.2$ fs $\ll T_v(0) = 15.2$ fs), there is minimal dissociation in accordance with the model predictions [Fig. 6.4(a)]. For a given F_0 , P_{dis} increases with N_c until it reaches a maximal value at $N_c \simeq 60-80$, whereafter P_{dis} decreases due to adiabaticity. For pulses in the range $N_c = 60-140$ and the larger F_0 , the saturation condition $P_{\text{ion}} + P_{\text{dis}} = 1$ [Fig. 6.5(c)] contributes to the decrease in P_{dis} . For these N_c 's the onset of dissociation is approximately at the dotted line corresponding to $\alpha_0 = \alpha_{0,th}$, consistent with Fig. 6.4(b). For the pulse with $N_c = 200$ ($\tau = 22$ fs), P_{dis} is less than 0.3, consistent with the picture that the population follows the field-dressed states adiabatically and dissociation is suppressed [Fig. 6.4(c)].

6.4 Control of the wave packet

The mechanisms described in Fig. 6.4 imply that by varying τ and α_0 , the vibrational populations, dissociation yields, and NKER can be controlled. This prediction is confirmed by the TDSE results of Fig. 6.6, which shows the bound vibrational populations and the NKER spectra for the $1s\sigma_g$ state at the end of the pulse, for $\omega = 2.278$, $F_0 = 1 - 17.9$, and $N_c = 10 - 500$. We checked that no dissociation occurs via the excited electronic states. For $N_c = 10$, the $\nu = 0$

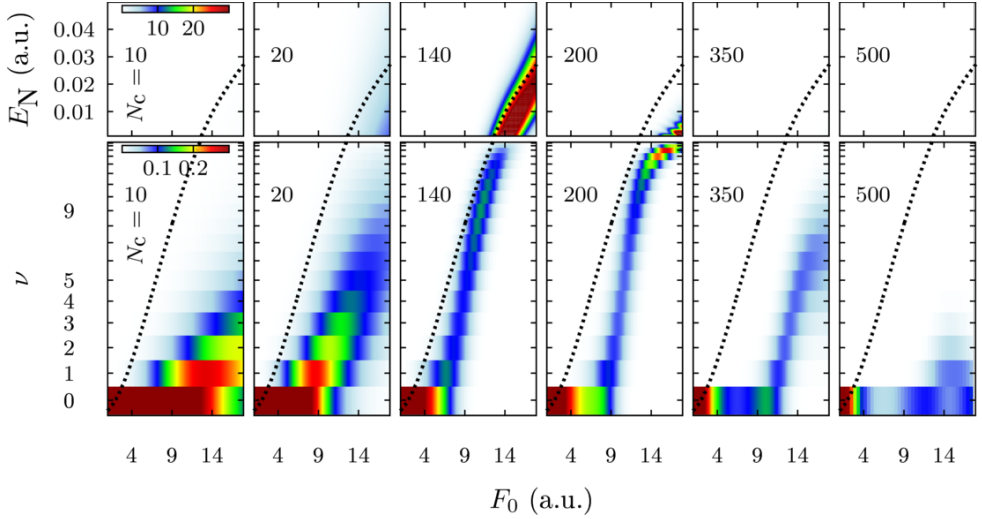


Figure 6.6: Vibrational distributions at the end of the pulse (bottom panels), and NKER spectra for dissociation in the ground electronic $1s\sigma_g$ state of H_2^+ (top panels). The laser pulses have $\omega = 2.278$, varying F_0 , and different N_c . For a given N_c , a vertical cut through the top and bottom panels correspond to a single TDSE calculation. The vertical axes are equidistant in energy using the same scale for the bound (bottom panels) and continuum (top panels) parts. Each row has the same color scale. The dotted lines indicate the energies of the field-dressed vibrational ground state at field maxima with respect to the dissociation limit, $W_{1,0}(\alpha_0) - E_d$.

level is most populated, except at $F_0 \gtrsim 14$ where strong non-adiabatic couplings excite some vibrations. No dissociation occurs, in agreement with Fig. 6.4(a). For $N_c = 140$, the vibrational population and the NKER spectra follow approximately the dotted line corresponding to $W_{1,0}(\alpha_0) - E_d$. This is in agreement with Figs. 6.4(b), 6.4(e), and the accompanying discussions, where we argued that the energy of the final WP with respect to E_d after the pulse is $W_{1,0}(\alpha_0) - E_d$. If $W_{1,0}(\alpha_0) < E_d$, the WP is bound, and field-free vibrational states satisfying $W_{1,\nu}(0) \simeq W_{1,0}(\alpha_0)$ are populated. If $W_{1,0}(\alpha_0) > E_d$, the WP dissociates with NKER $E_N \simeq W_{1,0}(\alpha_0) - E_d$. Note that the onset of dissociation occurs at $F_0 \simeq \omega^2 \alpha_{0,th}$. From $N_c = 140$ to $N_c = 500$, the adiabatic approximation for the evolution of the WP described in Fig. 6.4(c) becomes gradually more appropriate, with the field-free vibrational ground state populated up to increasingly larger F_0 . For $N_c = 350 - 500$, no dissociation occurs. By suitable choices of τ and F_0 , we can thus control the final vibrational populations and the NKER spectra.

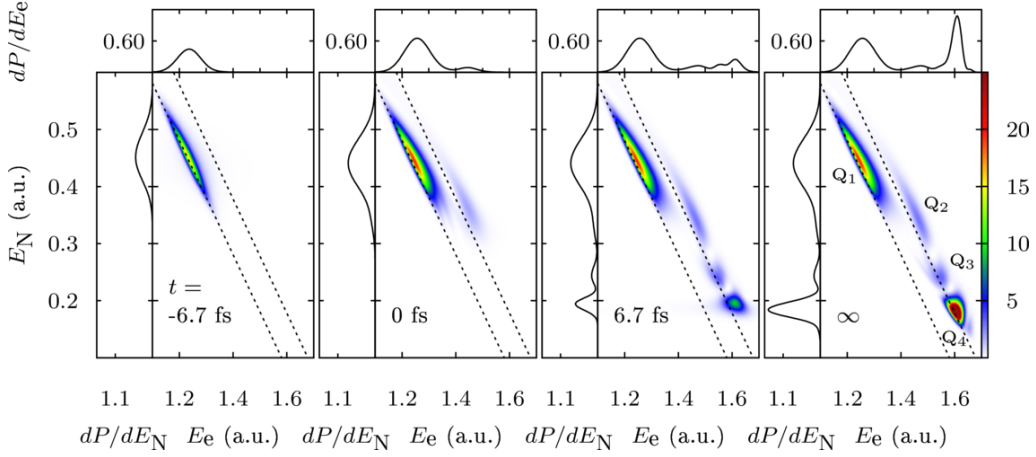


Figure 6.7: Time-resolved analysis showing the buildup of the JES for DI during a laser pulse with parameters $\alpha_0 = 2.41$, $\omega = 2.278$, and $N_c = 100$. Diagonal lines indicate the energy conservations $E_e + E_N = E_0 + \omega$ (left lines) and $E_e + E_N = W_{1,0}(\alpha_0) + \omega$. The upper and side subpanels show respectively the photoelectron and NKER spectra. Q_1, \dots, Q_4 denote the four maxima.

6.5 Probing the dissociative WP

As discussed, ionization happens throughout the whole duration of the pulse, leading to the possibility of probing the dissociation process by monitoring the DI channel. To understand the interplay between DI and dissociation, Fig. 6.7 presents the formation of the JES for the DI process, determined by the tSURFF method. Note that compared to Fig. 6.6, the NKER energies from DI are much greater than that from dissociation. The JES after the pulse ($t = \infty$) shows four distinct peaks, denoted by Q_1, \dots, Q_4 . The physical picture in Fig. 6.4(b) explains these. At $t = -6.7$ fs, the Stark shift $\Delta(t) \equiv W_{1,0}(\alpha_0(t)) - E_0$ is negligible, and ionization produces Q_1 in the JES along the line corresponding to the one-photon resonance $E_e + E_N = E_0 + \omega$. At $t = 0$, according to the model, the nuclear WP has the largest Stark shift $\Delta(0) = 0.09732$, and ionization leads to Q_2 along the shifted one-photon resonance $E_e + E_N = W_{1,0}(\alpha_0) + \omega$. At $t > 0$, the population stays above E_d and dissociates. During dissociation, ionization occurs at large R , leading to Q_3 and Q_4 with low E_N in the JES at $t = 6.7$. The structure of Q_3 and Q_4 will not be discussed here. Note that Q_1 is unchanging in magnitude and position for $t > 0$, consistent with the model prediction that no field-free bound states become repopulated during pulse turn-off. For this reason the dynamic interference effect discussed in Chapter 5, where ionized WPs with equal continuum energy created during the rising and falling edges of the pulse

interfere, is not observed. These insights indicate that dissociation and probing of dissociation by DI can be achieved using a single pulse, with the nuclear WP being promoted to the field-free dissociation continuum during turn-on (pump) and probed through DI during turn-off.

6.6 On the generality of the model

The dynamics in terms of the physical model has two requirements:

$$\text{a) Stabilization with respect to DI;} \quad (6.17)$$

$$\text{b) Increase of } E_{el,1} \text{ and } T_v \text{ with } \alpha_0. \quad (6.18)$$

Consider first a). We expect stabilization to occur in two-electron molecules such as H_2 , D_2 , and HeH^+ , provided $\omega > I_p$ [114, 122]. For other diatomics like N_2 , O_2 , CO , or NO , the orbital energies can be grouped into two classes formed by innershells with energies less than -11, and outershells with energies larger than -2. The same classification holds for triatomic molecules (e.g., CO_2 and H_2O), and even larger systems like naphthalene. For typical ω 's considered in this work, e.g. 2-3, the outershells satisfy $\omega > I_p$ where we expect stabilization, while innershell electrons can be excited to Rydberg states by multiphoton absorption and subsequently be stabilized [49, 50].

Now consider b). For large α_0 , it has been shown that $E_{el,1} \propto \alpha_0^{-2/3}$ [122, 123], while a perturbative analysis for small α_0 [Appendix C] shows that for a general diatomic molecule, $E_{el,1}$, R_0 , and T_v increases with α_0 . For intermediate α_0 , using quantum chemistry codes, the requirement b) was also fulfilled for H_2 [123–125]. Even when the molecule is not aligned with the linearly polarized field, the mentioned two requirements a) and b) still holds [123, 126], indicating that the observed dynamics would also occur in non-aligned molecules. In light of these considerations, the described dynamics are expected to be observable in two-electron diatomics, while further studies are required to determine whether this is generally the case.

For a molecule X_2 , with X some atomic species, the charged fragments X^+ and e from DI can be detected in coincidence by cold-target recoil ion momentum spectroscopy [51]. The resulting JES will contain structures satisfying $E_e + 2E_{\text{X}^+} = W_{1,0}(\alpha_0) + \omega$ for outershell DI, and $E_e + 2E_{\text{X}^+} = W_{1,0}(\alpha_0) + n_{\min}\omega$ for innershell DI, with n_{\min} the minimum number of photons required. A large spread in E_{X^+} containing low-energy X^+ fragments is a signature of continuous ionization during dissociation towards larger R , and thus a direct indication of the dressed dissociation channel (see Q_2 - Q_4 in Fig. 6.7 for H_2^+).

6.7 Conclusion

We have characterized some hitherto unobserved molecular breakup phenomena in the regime of super-intense, high-frequency, femtosecond pulses, adding insight to the general field of strong laser-matter interaction. The characteristics we find include: (i) Even with full inclusion of nuclear dynamics, stabilization against ionization occurs. (ii) A mechanism by which dissociation, in contrast to the expectation from energy considerations, completely dominates over ionization; (iii) Control over the vibrational distribution, dissociation yield, and NKER spectra by the parameters of the laser pulse; (iv) Insight into the interplay between dissociation and DI, and possibilities of measuring the dynamics using the JES.

INTER- AND INTRACYCLE
INTERFERENCE EFFECTS IN
DISSOCIATIVE IONIZATION

7.1 Motivation

As mentioned in the introduction, a characteristic atomic strong-field photoelectron spectrum (PES) features peaks separated by the photon energy, and the corresponding process is referred to as above threshold ionization (ATI) [9]. The appearance of such structures in the PES can be interpreted as interference between electronic wave packets (WPs) released during different cycles of the pulse, referred to as intercycle interferences. A decade ago, it was demonstrated that the PES can exhibit structures with modulations on larger energy scales than that of the photon, which were interpreted as intracycle interferences between WPs released during the same subcycle [11, 12, 127]. The signatures of intracycle interferences have been difficult to identify clearly in the complex spectra following strong-field ionization of atoms by linearly polarized laser pulses, but a two-color scheme with orthogonally polarized pulses very recently allowed a unique identification in Ar [128].

In the JES of the electron E_e and nuclear E_N energies, diagonal maxima separated by the laser frequency, ω , appear in the continuum JESs showing the energy sharing between electron and nuclei,

$$E_e + E_N = E_0 + n\omega - U_p. \quad (7.1)$$

The traditional ATI peaks in the PES were shown to be either badly resolved or gone completely due to the energy sharing [21, 75]. For field parameters close to the tunneling regime, the electrons were claimed to not share the energy with the

nuclei at all due to tunneling electrons [21], leading to a distribution of E_N for fixed E_e , i.e., for $E_e \simeq \text{const}$ [Figs. 4(a) and (b)].

In this chapter, we show that the exact inclusion of the nuclear degree of freedom in ionization by strong few-cycle laser pulses leads to clear holographic interference structures in the JES that at first sight defy standard energy conservation interpretations with pronounced cross-diagonal structures, i.e., maxima approximately at $E_e - E_N \simeq \text{const}'$ [Fig. 1(c)]. In the JES with E_N vs E_e we then have (i) diagonal maxima with positive slope [Eq. (7.1)], (ii) vertical maxima at constant E_e (infinite slope), and (iii) cross-diagonal maxima with negative slope. We show that all the structures (i)-(iii) are due to intra- and intercycle interference effects and the laser dependent DI dynamics. The main characteristics of the JES may be controlled by changing the frequency and carrier-envelope phase (CEP) of the driving pulse. The interplay between intra- and intercycle structures are present in the JES for all wavelength considered, but are especially clear for DI with midinfrared pulses. We note that there are different definitions of the midinfrared frequency regime, with 2000 nm often being the lower wavelength threshold of the definition. In this chapter, we will refer to the 1600 nm pulse as a midinfrared pulse.

7.2 TDSE results

We base our study on the 1D H_2^+ model, and work in VG with the vector potential

$$A(t) = \frac{F_0}{\omega} g(t) \cos \left[\omega \left(t - \frac{\tau}{2} \right) + \varphi_{\text{CEP}} \right], \quad (7.2)$$

and a sine-squared envelope $g(t)$. The dipole approximation holds for laser pulses considered here [36, 117].

Figure 7.1 shows the JES for H_2^+ after exposure to fields from the visible to the midinfrared regime. For the 400 nm pulse in Fig. 7.1(a), the characteristic diagonal peaks satisfy Eq. (7.1) [1, 21, 22, 75]. Due to the short pulse, electrons detected at $\pm x$ have different JESs [Fig. 7.1(a) insets]. Modulations along each diagonal is also observed. In the 800 nm case [Fig. 7.1(b)], in addition to the diagonal peaks, oscillatory structures on larger energy-scales are discernible, e.g., a structure with maximum at $E_e = 1.6$, and cross-diagonal structures with a positive slope shown in the insets. For the 1600 nm case in Fig. 7.1(c), the JES is, at first glance, completely dominated by the cross-diagonal structures, seemingly satisfying the nonintuitive energy-conservations $E_e - E_N = \text{const}'$. The insets show diagonal peaks, now superimposed on the cross-diagonal structures. Although one can distinguish fast oscillations superimposed on slower ones in

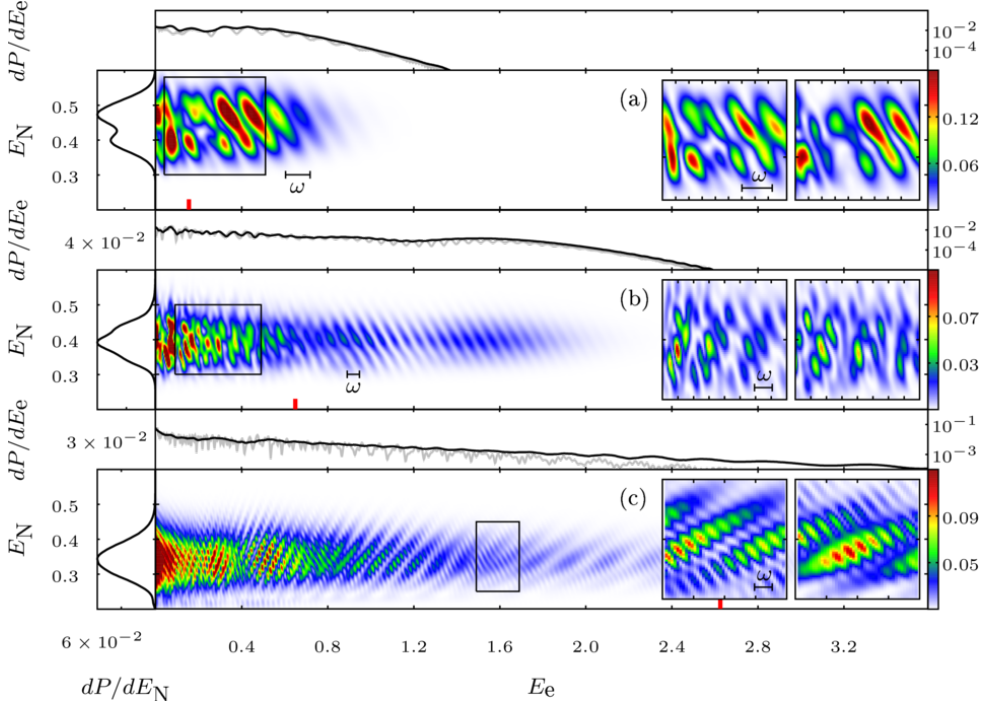


Figure 7.1: JES of H_2^+ after exposure to laser pulses with $I = 3 \times 10^{14} \text{ W/cm}^2$, $N_c = 6$, and (a) $\lambda = 400 \text{ nm}$ (b) 800 nm (c) 1600 nm , calculated by TDSE. The side and upper subpanels show nuclear spectra and PES. The grey lines shows the fixed-nuclei PES with $R = 2.06$ with rescaled magnitude. The left and right insets show zooms of the JES in the rectangular box, for electrons escaping in the positive and negative x -direction, respectively. The red markers indicate values of U_p .

the fixed nuclei PES in Fig. 7.1(c), they are completely washed out in the PES for moving nuclei, proving that for real molecules, the traditional PES is a poor observable. As we will show in the following, the different structures in the JES are due to the interplay between subcycle and intercycle interferences.

7.3 Strong-field approximation

In the strong-field approximation (SFA) [52, 54–56], the transition amplitude for direct ionization to the double continuum reads (we set $\mu \equiv \beta^{\text{VG}} \equiv 1$ for simplicity)

$$T_{p,k} = -i \int_0^\tau dt \langle \phi_p(t) \chi_k(t) | \tilde{V}_I(t) | \Psi_0(t) \rangle, \quad (7.3)$$

with $\tilde{V}_I(t) = -iA(t)\partial/\partial x + A(t)^2/2$ the laser-matter interaction, $|\Psi_0(t)\rangle = |\Psi_0\rangle e^{-iE_0 t}$, $|\phi_p(t)\rangle = |\phi_p\rangle e^{-i \int^t dt' [p + A(t')]^2/2}$ the Volkov wave with $E_e = p^2/2$, and $|\chi_k(t)\rangle =$

$|\chi_k\rangle e^{-ik^2t/m_p}$ the Coulomb wave solution to $T_N + V_N$ with $E_N = k^2/m_p$. We calculate $T_{p,k}$ in the saddle-point approximation [129],

$$T_{p,k} = \sum_s M_{p,k}(t_s) e^{iS_{p,k}(t_s)}. \quad (7.4)$$

The SFA phase is

$$S_{p,k}(t) = \int^t \left\{ \frac{[p + A(t')]^2}{2} + E_N - E_0 \right\} dt', \quad (7.5)$$

and

$$M_{p,k}(t_s) = -i \langle \phi_p \chi_k | \Psi_0 \rangle e^{i\varphi_s} \sqrt{\frac{2\pi}{|\dot{S}_{p,k}(t_s)|}} \left[pA(t_s) + \frac{A^2(t_s)}{2} \right], \quad (7.6)$$

with

$$\varphi_s = \frac{-\theta_s + \xi_s \pi}{2}, \quad (7.7)$$

where $i\ddot{S}(t_s) = |\ddot{S}(t_s)|e^{i\theta_s}$, and the term involving $\xi_s = \pm 1$ in Eq. (7.7) corresponds to the forward and backward directions along the integration trajectories of steepest descent. The angle φ_s determines the relative phase between the terms in Eq. (7.4) and must be evaluated correctly. By considering the global behavior of e.g. $|e^{iS(t)}|^2 = e^{2\text{Re}[iS(t)]}$, we can show that for the present case, $\varphi_s \in [-\pi/2, \pi/2]$ (the principal argument is chosen to lie in the interval $]-\pi, \pi[$). The complex saddle points t_s are solutions of

$$\dot{S}_{p,k}(t) = \frac{[p + A(t)]^2}{2} + E_N - E_0 = 0 \quad (7.8)$$

with $0 < \text{Re}(t_s) < \tau$ and $\text{Im}(t_s) > 0$, and $\dot{S}_{p,k}$ ($\ddot{S}_{p,k}$) denotes the derivative (double-derivative) of $S_{p,k}$ with respect to time, t . For an N_c -cycle \sin^2 pulse there are $2(N_c + 1)$ solutions. The terms in Eq. (7.4) correspond to quantum paths for electrons and nuclei reaching the same final momentum pair (p, k) but released at different times $\text{Re}(t_s)$, leading to interference in the continuum. The left panels of Fig. 7.2 show the SFA JESs obtained from $|T_{p,k}|^2$. We use a logarithmic scale for the SFA analysis due to its qualitative nature. The qualitative similarities with Fig. 7.1 are evident. For 400 nm, the SFA shows three lobes emanating in the cross-diagonal direction, with diagonal structures superimposed on each lobe, which are consistent with the modulations along the diagonals in Fig. 7.1(a). For 800 nm and 1600 nm in Fig. 7.2, the same trend is observed, with shorter spacings between the cross-diagonal structures as the wavelength is increased.

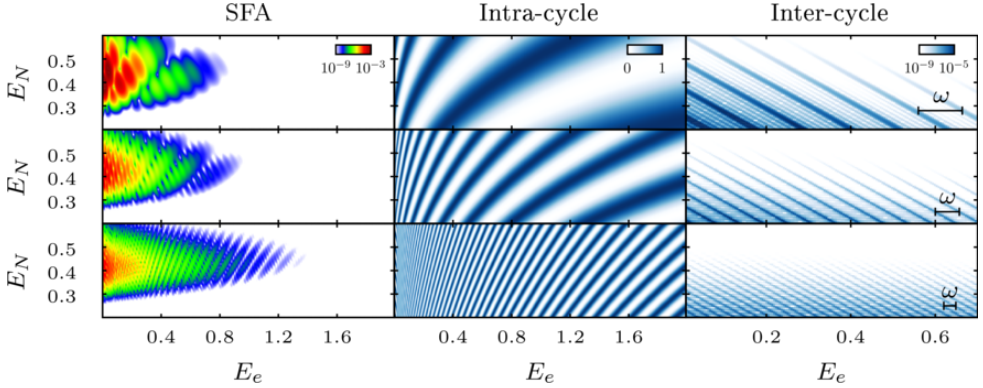


Figure 7.2: Left panels: JES calculated with SFA. Middle and right panels: Intracycle $G_{p,k}^{\text{intra}}$ and intercycle $G_{p,k}^{\text{inter}}$ contributions [Eq. (7.22)] assuming a constant field envelope. The pulse parameters are $I = 3 \times 10^{14}$ W/cm², $N_c = 6$, and from top to bottom: $\lambda = 400$ nm, 800 nm, and 1600 nm.

7.3.1 Analytic expressions for a flat-top pulse

For further analysis, we consider an N_c -cycle flat-top pulse

$$A(t) = \begin{cases} A_0(t) & \text{for } t \in]-\infty, 0[, \\ \frac{F_0}{\omega} \cos(\omega t + \varphi_{\text{CEP}}) & \text{for } t \in [0, \tau], \\ A_1(t) & \text{for } t \in]\tau, \infty[, \end{cases} \quad (7.9)$$

with $A_1(t)$ and $A_2(t)$ the smooth pulse turn-on and turn-off. In the following, we consider only the flat-top segment $t \in [0, \tau]$ of the pulse to obtain analytical expressions and make physical interpretations.

We will only treat the case with $p > 0$, as the case with $p < 0$ can be treated analogously and will not be discussed here. The equation for the saddle points in Eq. (7.8) can be rewritten

$$\cos(\omega t + \varphi_{\text{CEP}}) = -\kappa \pm i\gamma, \quad (7.10)$$

where we have defined the scaled momentum

$$\kappa = \frac{\omega p}{F_0} \quad (7.11)$$

and the E_N -dependent Keldysh parameter

$$\gamma = \frac{\omega \sqrt{2(-E_0 + E_N)}}{F_0}. \quad (7.12)$$

We denote the two complex solutions t_s during the j 'th optical cycle in Eq. (7.10) satisfying $0 < \text{Re}(t_s) < \tau$ and $\text{Im}(t_s) > 0$ as t_{j1} and t_{j2} . They are given by

$$\begin{aligned} t_{j1} &= \frac{1}{\omega} \left[\cos^{-1}(-\kappa - i\gamma) + 2\pi(j-1) - \varphi_{\text{CEP}} \right], \\ t_{j2} &= \frac{1}{\omega} \left[2\pi - \cos^{-1}(-\kappa + i\gamma) + 2\pi(j-1) - \varphi_{\text{CEP}} \right]. \end{aligned} \quad (7.13)$$

Evaluation of $M_{p,k}$

We will now evaluate $M_{p,k}$ and show that $M_{p,k}(t_{j1}) \approx M_{p,k}(t_{j2})$. The factor in square brackets in Eq. (7.6) is easily evaluated to give

$$\begin{aligned} pA(t_{j1}) + \frac{A^2(t_{j1})}{2} &= pA(t_{j2}) + \frac{A^2(t_{j2})}{2} \\ &= -E_e - E_N + E_0. \end{aligned} \quad (7.14)$$

By using the identities $\sin(\cos z) = \sqrt{1 - z^2}$ and $\sqrt{z} = \sqrt{|z| + \text{Re } z} + i \text{sgn}(\text{Im } z) \sqrt{|z| - \text{Re}(z)}$, it is straight forward to show that

$$\begin{aligned} i\ddot{S}(t_{j1}) &= F_0 \sqrt{-E_0 + E_N} (-A + iB), \\ i\ddot{S}(t_{j2}) &= F_0 \sqrt{-E_0 + E_N} (-A - iB), \end{aligned} \quad (7.15)$$

with

$$A = \sqrt{|z_+ z_-| - \text{Re}(z_+ z_-)}, \quad B = \sqrt{|z_+ z_-| + \text{Re}(z_+ z_-)}, \quad (7.16)$$

$$z_+ = \kappa + 1 + i\gamma, \quad z_- = \kappa - 1 + i\gamma, \quad (7.17)$$

Due to $A > 0$ and $B > 0$, θ_{j1} (θ_{j2}) lies in the second (third) quadrant, with $\theta_{j1} = -\theta_{j2}$. So to satisfy the condition $\varphi_s \in [-\pi/2, \pi/2]$, we must have in Eq. (7.7)

$$\begin{aligned} \xi_{j1} &= 1 \\ \xi_{j2} &= -1. \end{aligned} \quad (7.18)$$

The $M_{p,k}(t_s)$ element reads

$$M_{p,k}(t_s) = \tilde{M}_{p,k} \times \begin{cases} e^{i(\pi - \theta_{j1})/2} & \text{for } t_s = t_{j1}, \\ e^{i(-\pi - \theta_{j2})/2} & \text{for } t_s = t_{j2}, \end{cases} \quad (7.19)$$

with

$$\tilde{M}_{p,k} = \frac{-i\sqrt{2\pi} \langle \phi_p \chi_k | \Psi_0 \rangle (E_0 - E_e - E_N)}{\sqrt{F_0} [(A^2 + B^2)(-E_0 + E_N)]^{1/4}}. \quad (7.20)$$

Note that for a flat-top pulse, $M_{p,k}$ is independent of the optical cycle index j .

We will now show that $M_{p,k}(t_{j1}) \approx M_{p,k}(t_{j2})$. First we argue that $A \geq B$. For this to be true, in Eq. (7.16) we must satisfy the condition $-\text{Re}(z_+z_-) = 1 + \gamma^2 - \kappa^2 \geq 0$, which is equivalent to $(1 + \gamma^2)/2 \geq E_e\omega^2/F_0^2$. For the worst scenario with the electron having the largest possible energy without rescattering, $E_e = 2U_p$, and $(1 + \gamma^2)/2 \geq 1/2$, which is always satisfied, proving $A \geq B$. If $A \gg B$, which is often the case, $M_{p,k}(t_{j1}) = M_{p,k}(t_{j2})$ follows. In the worst case scenario $A = B$ [requiring $\text{Re}(z_+z_-) = 0$ in Eq. (7.16)], $\theta_{j1} = -\theta_{j2} = 3\pi/4$, and $\varphi_{j1} = -\varphi_{j2} = \pi/8$. As $\text{Re}(e^{i\varphi_{j1}}) = \text{Re}(e^{i\varphi_{j2}}) = 0.92$ is dominant compared to $\text{Im}(e^{i\varphi_{j1}}) = -\text{Im}(e^{i\varphi_{j2}}) = 0.38$, we have $M_{p,k}(t_{j1}) \approx M_{p,k}(t_{j2})$ also in this (worst) case. Henceforth we will make the approximation

$$M_{p,k}(t_{j1}) = M_{p,k}(t_{j2}) \equiv M_{p,k}. \quad (7.21)$$

Factorization of $|T_{p,k}|^2$

Assuming the relation (7.21), and defining the averaged phase

$$\bar{S}_{p,k,j} = \frac{S_{p,k}(t_{j1}) + S_{p,k}(t_{j2})}{2}, \quad (7.22)$$

and the phase difference (independent of the cycle index j)

$$\Delta S_{p,k} = S_{p,k}(t_{j1}) - S_{p,k}(t_{j2}), \quad (7.23)$$

the transition probability is rewritten

$$\begin{aligned} |T_{p,k}|^2 &= |M_{p,k}|^2 \left| \sum_{j=1}^{N_c} \left[e^{iS_{p,k}(t_{j1})} + e^{iS_{p,k}(t_{j2})} \right] \right|^2 \\ &= |M_{p,k}|^2 \left| \sum_{j=1}^{N_c} e^{i\bar{S}_{p,k,j}} \left(e^{i\Delta S_{p,k}/2} + e^{-i\Delta S_{p,k}/2} \right) \right|^2 \\ &= 4|M_{p,k}|^2 \cos^2 \left(\frac{\Delta S_{p,k}}{2} \right) \left| \sum_{j=1}^{N_c} e^{i\bar{S}_{p,k,j}} \right|^2 \\ &= 4|M_{p,k}|^2 \cos^2 \left(\frac{\Delta S_{p,k}}{2} \right) |C_{p,k}|^2 \left| \sum_{j=1}^{N_c} e^{ijQ_{p,k}} \right|^2 \end{aligned} \quad (7.24)$$

$$= 4|M_{p,k}|^2 \underbrace{\cos^2 \left(\frac{\Delta S_{p,k}}{2} \right)}_{\equiv G_{p,k}^{\text{intra}}} |C_{p,k}|^2 \underbrace{\left[\frac{\sin(N_c Q_{p,k}/2)}{\sin(Q_{p,k}/2)} \right]^2}_{\equiv G_{p,k}^{\text{inter}}}, \quad (7.25)$$

with $Q_{p,k} = 2\pi(-E_0 + E_e + E_N + U_p)/\omega$ and

$$|C_{p,k}|^2 = \left[\frac{1}{2} \left(\sqrt{2} \sqrt{|z_+ z_-| + \kappa^2 + \gamma^2 - 1} + |z_+| + |z_-| \right) \right]^{-\frac{F_0^2}{\omega^3}(\kappa^2 + 1/2 + \gamma^2)} \times \exp \left[\frac{\sqrt{2} F_0^2}{4 \omega^3} (\gamma A + 3\kappa B) \right] \quad (7.26)$$

which is independent of N_c , and

$$\Delta S_{p,k} = \frac{F_0^2}{\omega^3} \left[- \left(\kappa^2 + \frac{1}{2} + \gamma^2 \right) \cos^{-1} \left(\frac{|z_+| - |z_-|}{2} \right) + \frac{\sqrt{2}}{4} (3\kappa A - \gamma B) \right]. \quad (7.27)$$

In Refs. [127, 130], a similar factorization approach was employed for atomic systems where $\text{Im}(t_s)$ and E_0 were neglected. In our case, however, due to the dependence on E_N , $\text{Im}(t_s)$ must be taken into account.

The factor $G_{p,k}^{\text{inter}}$ can be interpreted as intercycle interference where wave packets (WPs) released during different cycles interfere, giving rise to multiphoton peaks as described by Eq. (7.1). This is shown in the right panels of Fig. 7.2, where $G_{p,k}^{\text{inter}}$ is plotted for a six-cycle pulse with different wavelengths. In the limit of an infinitely long pulse, the sum in Eq. (7.24) turns into the Dirac comb,

$$\sum_{j=-\infty}^{\infty} e^{ijQ_{p,k}} = \omega \sum_{n=-\infty}^{\infty} \delta(-E_0 + E_e + E_N + U_p - n\omega). \quad (7.28)$$

The factor $G_{p,k}^{\text{intra}}$ arises due to the intracycle interferences between WPs released during the same subcycle, and is depicted in the middle panels of Fig. 7.2. The period of the intracycle structures increases with E_e for fixed E_N , and decrease with E_N for fixed E_e . With increasing ω , the energy period increases as well. The increase of period with E_e and ω can be understood intuitively: larger E_e and ω imply shorter time interval Δt between WP-releases in a subcycle due to $p \approx -A [\text{Re}(t_s)]$, which in turn corresponds to a larger energy period $\Delta E_e \sim 1/\Delta t$.

Note that in this simple SFA model, the derived formulas for intercycle and intracycle interference patterns determined by $G_{p,k}^{\text{intra}}$ and the \sin^2 factor in $G_{p,k}^{\text{inter}}$ of Eq. (7.24) should work **generally** for all molecular species undergoing dissociative single ionization from a bound state, with the only molecular-dependence being the initial state energy E_0 . Additional patterns in the JES can occur due to the weighing factor $|M_{p,k}|^2$ in Eq. (7.24), which can be molecular structure-specific.

Low frequency limit

In the limit $\omega \ll 1$, by expanding the exponent of the exponential function in Eq. (7.26) to lowest order in ω (the first term in Eq. (7.26) is rewritten as $a = \exp[\ln(a)]$ before expansion), we obtain

$$|C_{p,k}|^2 \stackrel{\omega \ll 1}{\approx} \exp\left(-\frac{2s^3}{3F_0}\right) \exp\left[\left(\frac{s^2}{5} - p^2\right) \frac{s^3 \omega^2}{3F_0^3}\right], \quad (7.29)$$

with $s = \sqrt{2(-E_0 + E_N)}$. The first factor is recognized as the exponential factor in the tunneling ionization rate [131] and predicts the decay of yield with increasing E_N , while the second factor predicts decay of yield with increasing E_e . Both are consistent with the right panels of Fig. 7.2.

For the intracycle structures, to lowest orders in ω ,

$$\begin{aligned} \Delta S_{p,k} \stackrel{\omega \ll 1}{\approx} & -\frac{\pi F_0^2}{4 \omega^3} + 2p \frac{F_0}{\omega^2} - \frac{\pi(p^2 + s^2)}{2} \frac{1}{\omega} \\ & + \left(\frac{p^3}{3} + \frac{3ps^2}{2}\right) \frac{1}{F_0} - \frac{p^2 s^2}{2} \frac{\omega}{F_0^2}. \end{aligned} \quad (7.30)$$

Setting $\Delta S_{p,k} = 2\pi n$, we readily obtain an analytical expression for the maxima of the intracycle structures [see Fig. 7.3],

$$E_N = \frac{-2\pi n \omega - \frac{\pi F_0^2}{4 \omega^2} + \frac{2F_0 p}{\omega} - \frac{\pi p^2}{2} + \frac{\omega p^3}{3F_0}}{\pi - \frac{3\omega p}{F_0} + \frac{\omega^2 p^2}{F_0^2}} + E_0. \quad (7.31)$$

Note that the oscillating parts of $G_{p,k}^{\text{inter}}$ and $G_{p,k}^{\text{intra}}$ have increasing periods in the $\omega \rightarrow 0$ limit. For very small ω this leads to a washing out of any modulation in the spectra in accordance with the expectation from tunneling theory in the dc limit.

7.4 Time-resolved JES

The interplay between inter- and intracycle interferences are directly confirmed by the time-resolved formation of the JES by TDSE calculations, shown in Fig. 7.3. During the first 7/4 cycles of the pulse shown in the top panels of Fig. 7.3, appreciable ionization can only occur during the half-cycle indicated by the dots due to the scaling of F in Eq. (7.29). The ionized WPs can be considered a double-slit in time, giving rise to intracycle interferences in the direction $p > 0$. Half a cycle later, we observe intracycle structures in Fig. 7.3 with $p < 0$. Near the end of the pulse, intercycle structures separated by ω are superimposed on

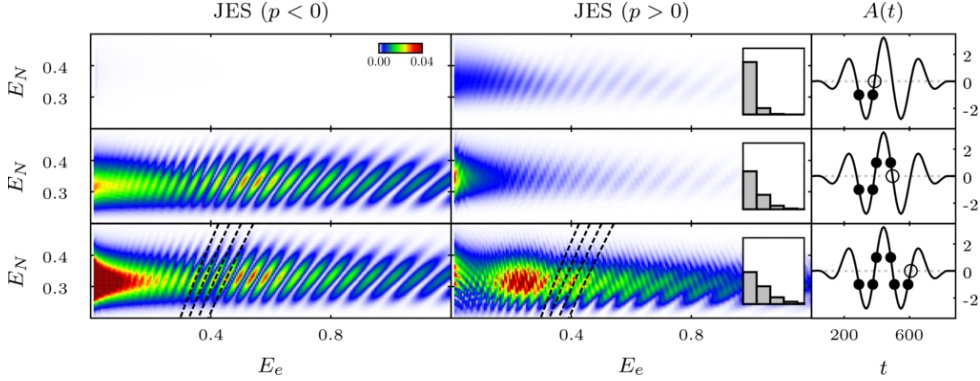


Figure 7.3: The buildup of the JES for $\lambda = 1600$ nm, $I = 3 \times 10^{14}$ W/cm², and $N_c = 4$, calculated with TDSE. The right panels depict the pulse, with the circles indicating the instantaneous times and the dots indicating the contributing $\text{Re}(t_s)$ corresponding to $E_e = 0.5$. The insets show the vibrational populations of the first four vibrational states with the ordinate scale $[0, 1]$. The dashed lines in the lowest panels show the analytical predictions Eq. (7.31) for $n = -35$ to -32 .

intracycle structures for $p > 0$ due to interference of WPs ionized in two different cycles. The clear increase in the JES yield is due to the significant population of excited vibrational states with a smaller ionization potential (IP), shown in the insets of Fig. 7.3. A good agreement is observed between the TDSE intracycle peaks and the analytical prediction in the low-frequency limit given by Eq. (7.31) (dashed lines in Fig. 7.3).

7.5 CEP effects

For a two-cycle pulse, the CEP-dependence of the JES is illustrated in Fig. (7.31). In the $\varphi_{\text{CEP}} = 0$ case, dominant ionization occurs in the direction $p < 0$, corresponding to ionization near the peak of the A -field, and intracycle interference patterns are clearly observed. In the direction $p > 0$, weak intercycle patterns in terms of diagonal structures are present, corresponding to interference wave packets released between the two minima of the field. For $\varphi_{\text{CEP}} = \pi/4$, intracycle structures in the JES are visible for both $p > 0$ and $p < 0$, with the intercycle structures absent due to the absence of equally-contributing WP release from two different cycles. For $\varphi_{\text{CEP}} = \pi/2$, the pulse is symmetric, but the JESs in the two directions are clearly not. The reason is the population of excited vibrational states during the first cycle of the pulse, which ionizes during the second cycle towards the direction $p > 0$ with higher probability. Also, the JES density is largest at $E_e \approx 0.22$ instead of $E_e \approx 0$, suggesting a possible channel-closing

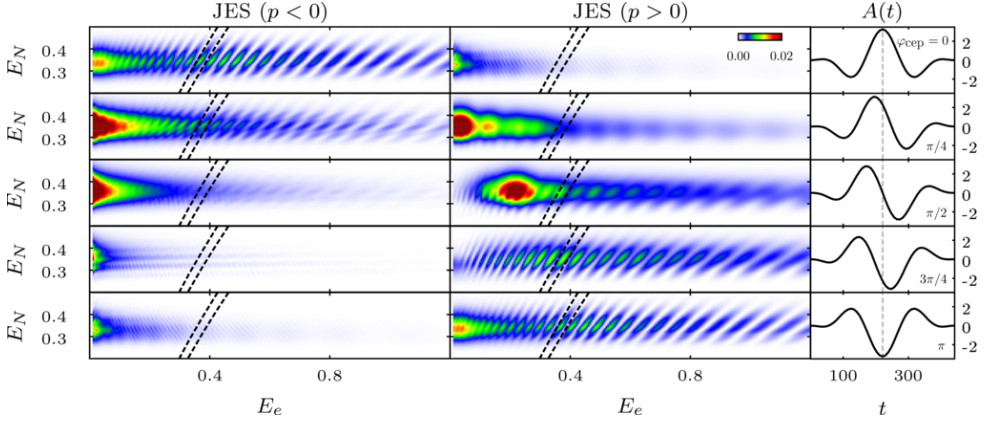


Figure 7.4: The CEP dependence of the JES for $\lambda = 1600$ nm, $I = 3 \times 10^{14}$ W/cm², and $N_c = 2$, by solving the TDSE. The right panels depict the pulse. The insets show the vibrational populations of the first four vibrational states with the ordinate scale $[0, 1]$. The dashed lines in the lowest panels show the analytical predictions (7.31) for $n = -35$ and -34 .

mechanism. This effect is not understood presently and will not be discussed. For $\varphi_{\text{CEP}} = 3\pi/4$, intracycle patterns are clearly observed for $p > 0$, while for $p < 0$ no such structures are present. For $\varphi_{\text{CEP}} = \pi$, the situation is the same as for the $\varphi_{\text{CEP}} = 0$ case, with the role of left and right direction reversed. We have established that the CEP can be used to control the inter- and intracycle interferences, as well as the electron release direction.

7.6 Nuclear motion effects

So far, we have associated the diagonal structures to intercycle effects and the cross-diagonal structures to intracycle effects. At lower intensities however, a different picture emerges, which is depicted in Figs. 7.5(a) and 7.5(b). Instead of intracycle structures with positive slope, the structures are now vertical, and the JES for $p > 0$ is shifted towards smaller E_N compared to the JES for $p < 0$. The physical explanation is sketched in Fig. 7.5(c). At t_1 , the instantaneous intensity is too low to allow significant direct ionization. Instead, a dissociative WP is created on the $2p\sigma_u$ curve. This is confirmed by a separate calculation for the nuclear dynamics wherein we neglect the electronic continuum, and only take into account the lowest two BO surfaces [96]. The population density in $2p\sigma_u$ is shown in Fig. 7.5(e) and a dissociative nuclear WP is seen created at t_1 . At $t \approx t_2$, the dissociative WP has moved towards larger R , but the IP and F are still unsuitable for appreciable ionization, resulting in the JESs at t_3 shown in the

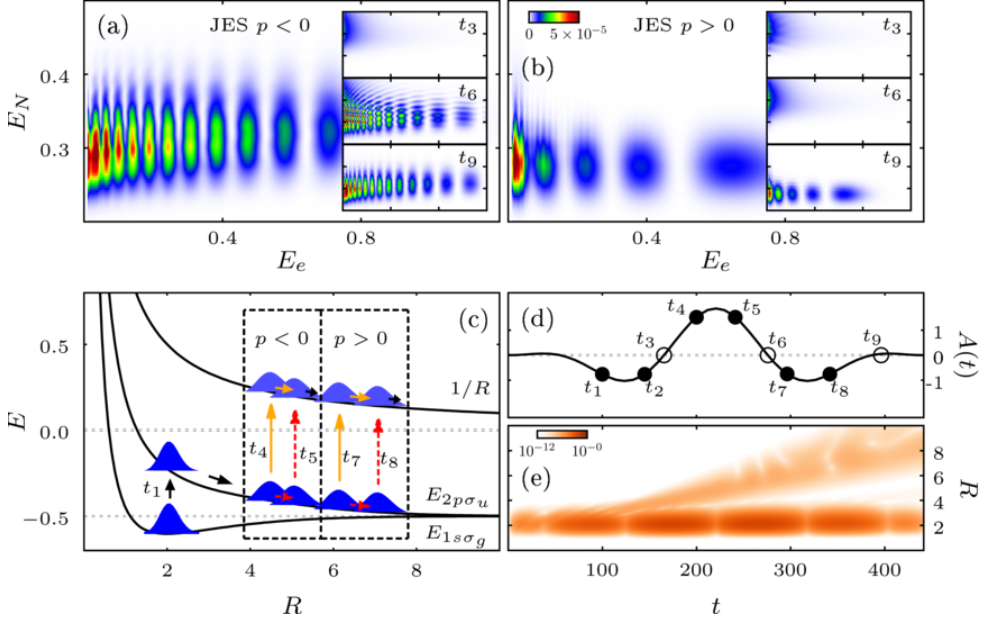


Figure 7.5: (a) JES from TDSE for $\lambda = 1600$ nm, $I = 10^{14}$ W/cm², and $N_c=2$, with $p < 0$. The insets show the time-resolved buildup of the JES during the pulse shown in (d). (b) Same as (a), with $p > 0$. (c) Schematic of the nuclear dynamics. The three curves are the lowest two BO curves corresponding to the electronic states $1s\sigma_g$ and $2p\sigma_u$, and the DI curve $1/R$. (e) Nuclear density in the $2p\sigma_u$ electronic state using a two-surface model (see text).

first inset of Figs. 7.5(a) and 7.5(b). At $t \approx t_4$ and t_5 , two electronic continuum WPs are created, giving rise to intracycle interferences for $p < 0$. However, as the $2p\sigma_u$ and $1/R$ curves are nearly parallel, the effective IP is almost independent of R , and $\Delta S_{p,k}$ is independent of E_N . This explains the vertical structures observed in Fig. 7.5(a). The nuclear WPs follow the two pathways indicated in Fig. 7.5(c) by the orange and red arrows, and lead to the same final nuclear WP. The average nuclear energy \bar{E}_N of the final DI WP is the sum of $1/R(t_5)$ and the kinetic energy gained during dissociation from t_1 to t_5 . The dissociative WP is created at $R \approx 3$ [Fig. 7.5(e)], which leads to $\bar{E}_N = 0.289$, in good agreement with Fig. 7.5(a). By the same reasoning, the electronic WPs created at $t = t_7$ and $t = t_8$ interfere for $p > 0$, resulting in the vertical intracycle interference patterns in Fig. 7.5(b) and a nuclear energy $\bar{E}_N = 0.282$. For longer pulses, we observed near-vertical structures separated by ω , corresponding to intercycle interferences (not shown). Note that our understanding of the vertical structures are different from the one given in Ref. [21], where it was claimed that the vertical structures in the JES were due to tunneling electrons from the ground electronic state $1s\sigma_g$.

The importance of the excited electronic states in the JES were discussed recently in Ref. [132].

7.7 Conclusion

In conclusion, we have established that in strong-field dissociative single ionization of molecules, the emerging rich structures in the JES, involving diagonal [Eq. (7.1)], vertical, and cross-diagonal patterns, are due to the interplay between inter- and intracycle interferences. Although the numerical demonstration is performed for H_2^+ , strong-field physics in the long wavelength regime is the physics of valence electrons, and our results is expected to hold generally for multielectron molecular systems as well. This is also reflected in the fact that for a flat-top pulse, the SFA analytical expressions determining the interference patterns in Eq. (7.24) depend only on the molecular species in terms of the initial state energy.

The PES alone provides a poor observable for the detection of the inter- and intracycle structures. Luckily, measurement techniques such as COLTRIMS [36, 51] exist that can measure ions and electrons in coincidence, and midinfrared sources are also already available [36]. The linear scale of the colorplots, and the distinct characteristic crossings of the structures, therefore points to the feasibility of an experimental verifications of the predicted effects. The inter- and intracycle interference structures carry direct information of femtosecond and sub-femtosecond dynamics, and the present insights therefore add to the understanding of time-resolved phenomena.

MOLECULAR TUNNELING IONIZATION WITH ELECTRON-ELECTRON CORRELATION

The semi-classical model for strong-field processes is described in terms of the three-step model, mentioned briefly in the introduction, consisting of ionization, propagation in the field, and rescattering. In the quasistatic picture at sufficiently low field frequency and high intensity, the electron ionizes by tunneling through the effective potential barrier created by the ionic potential and the instantaneous electric field. The correct description of tunneling ionization is therefore crucial for the understanding of strong-field processes.

We will in Section 8.1 give an overview of tunneling theories, before moving on to give a brief description of many-electron weak-field asymptotic theory (ME-WFAT) in Section 8.2. In Section 8.3 we will discuss the Dyson orbitals required in WFAT and how to obtain them using the TD-GASCI method. Results for the molecular-orientation-dependent structure factor in H₂ and LiH are presented in Section 8.4. Section 8.5 concludes the chapter.

8.1 Tunneling ionization overview

In analytical tunneling theories, the rate for ionization in a static electric field in the limit $F \rightarrow 0$ satisfies the asymptotic expansion [60]

$$\Gamma = cF^b e^{-a/F} (1 + AF \ln F + BF + \dots), \quad (8.1)$$

with the coefficients a, b, c, A, B, \dots independent of F . It took several decades to obtain the leading order coefficients for the hydrogen ground state [131, 133] with $a = 2/3$, $b = -1$, and $c = 4$. Generalizations were later obtained for a short-range

potential [134], arbitrary states of hydrogen [135, 136], and arbitrary states in a spherically symmetric potential [137, 138]. The latter results were reproduced and popularized by Ammosov, Delone, and Krainov [57], and are referred to now as ADK theory. An attempt to extend the atomic results [57] to general molecular systems was performed in Ref. [58], now referred to as MO-ADK theory. The formulas for the MO-ADK ionization rate are not derived with the Schrödinger equation as the starting point, but rather derived by analogy with the atomic ADK theory. Consequently, the range of applicability of the theory and the consistency with respect to the dominant terms in the asymptotic expansion (8.1), remains unclear. Furthermore, the effect of a possible permanent dipole is not included in the original MO-ADK, which is especially unsatisfying in light of recent interest in dipole effects in strong-field ionization [139, 140].

The one-electron weak-field asymptotic theory (OE-WFAT) was developed recently [59] to improve and extend the previous tunneling theories. OE-WFAT naturally incorporates the permanent dipole moment, allows the treatment of polar molecules, gives a more clear range of applicability, and can consistently pick out the dominant leading-order term in the expansion (8.1). The approximations made in the derivation are the non-relativistic approximation, the SAEA (for multi-electron systems), and the FNA. In the dominant leading-order term, Γ consists of two factors. The first factor is the so-called structure factor, which depends on the asymptotic tail of the field-free orbital for the active electron. It is thus independent of F and depends on the orientation of the molecule with respect to the field. The second factor is an analytically known function of F . The WFAT was applied on linear molecules [20, 59, 141, 142], and on more complicated systems such as C_2H_4 [143], H_2O [144], CH_3Br and CH_3F [145], and HCCI [146].

The generalization of the WFAT to the many-electron systems was considered in Ref. [60], which we refer to as ME-WFAT. The dominant term in the expansion (8.1) was shown to take on a similar analytical form as in the one-electron case, being a product of a structure factor and a field-dependent factor. The major difference is now that the structure factor depends on the Dyson orbital, which is the overlap between the N -electron wave function and the $(N - 1)$ -electron wave function of the ion. Formulation of many-electron tunneling theories exist prior to WFAT (e.g. Ref. [147]), but they are not derived from the perspective of the asymptotic expansion in Eq. (8.1). In the next section we will give a brief overview of the derivation of ME-WFAT.

An extension of the WFAT to molecules beyond the FNA with inclusion of the initial nuclear wave function is considered in Ref. [148–150], while conclusion of first-order terms in the expansion (8.1) is treated in Ref. [151] in FNA and SAEA. These extensions will not be considered in this thesis.

8.2 The weak-field asymptotic theory

We will briefly sketch the derivation steps and the main results of ME-WFAT in this section, following the approach in Refs. [59, 60]. The formulas are derived for a general N -electron, polyatomic molecule in first quantization.

In the FNA, the Hamiltonian for an N -electron, A -nuclei system interacting with a static electric field $F > 0$ pointing in the positive z direction of the laboratory frame reads

$$H_N = \sum_{i=1}^N \left(-\frac{1}{2} \nabla_{\mathbf{r}_i}^2 - \sum_{a=1}^A \frac{Z_a}{|\mathbf{r}_i - \mathbf{R}_a|} + \sum_{j=1}^{i-1} \frac{1}{|\mathbf{r}_i - \mathbf{r}_j|} + Fz_i \right). \quad (8.2)$$

The electronic wave function is denoted by $\Psi(\mathbf{Q}_N)$, with $\mathbf{Q}_N = (\mathbf{q}_1, \dots, \mathbf{q}_N)$ and $\mathbf{q}_i = (\mathbf{r}_i, \sigma_i)$, where \mathbf{r}_i is the spatial and σ_i the spin coordinate of the i th electron. A one-electron spin function is denoted χ_{m_s} with the property $\chi_{m_s}(\sigma) = \delta_{m_s \sigma}$, and a spin projection is denoted $\chi_{m_s}^T(\sigma)$ with the orthonormality condition $\chi_{m_s}^T \chi_{m'_s} = \delta_{m_s m'_s}$. $\Psi(\mathbf{Q}_N)$ is a solution to the TISE

$$(H_N - E) \Psi(\mathbf{Q}_N) = 0. \quad (8.3)$$

Regular solutions to Eq. (8.3) with outgoing boundary conditions are the Siegert states (SSs) [152], which has complex eigenvalues

$$E = \mathcal{E} - \frac{i}{2} \Gamma \quad (8.4)$$

with the energy \mathcal{E} and ionization rate Γ .

8.2.1 Adiabatic expansion in parabolic coordinates

In the weak-field limit, one of the N electrons can tunnel out towards the negative z direction, labelled here as the N th electron. Tunneling ionization of more than one electron will be shown to be exponentially suppressed. It is thus instructive to rewrite the Hamiltonian as

$$H_N = H_{N-1} - \frac{1}{2} \nabla^2 + V(\mathbf{r}) + Fz, \quad (8.5)$$

with $\mathbf{r} = \mathbf{r}_N$, $\sigma \equiv \sigma_N$, H_{N-1} the $(N-1)$ -electron Hamiltonian, and $V(\mathbf{r})$ the interaction of the outgoing electron with the nuclei and all other electrons:

$$V(\mathbf{r}) = - \sum_{a=1}^A \frac{Z_a}{|\mathbf{r} - \mathbf{R}_a|} + \sum_{i=1}^{N-1} \frac{1}{|\mathbf{r} - \mathbf{r}_i|}. \quad (8.6)$$

In the asymptotic region

$$V(\mathbf{r})|_{r \rightarrow \infty} = -\frac{Z}{r} + \mathcal{O}(r^{-2}), \quad (8.7)$$

with the total charge of the parent ion

$$Z = \sum_{a=1}^A Z_a - N + 1. \quad (8.8)$$

As known from literature [131], the TISE for a one-electron atom in a static electric field is separable in parabolic coordinates,

$$\xi = r + z, \quad \xi \in [0, \infty] \quad (8.9a)$$

$$\eta = r - z, \quad \eta \in [0, \infty] \quad (8.9b)$$

$$\varphi = \tan^{-1}\left(\frac{y}{x}\right), \quad \varphi \in [0, 2\pi], \quad (8.9c)$$

and due to $V(\mathbf{r})$ approaching $1/r$ at large distances in Eq. (8.7), one expects these parabolic coordinates to be useful in the present context as well. The TISE (8.3) takes on the form

$$\left[\frac{\partial}{\partial \eta} \eta \frac{\partial}{\partial \eta} + \mathcal{B}(\eta) + (E - H_{N-1}) \frac{\eta}{2} + \frac{F\eta^2}{4} \right] \Psi(\mathbf{Q}_N) = 0, \quad (8.10)$$

with the adiabatic Hamiltonian $\mathcal{B}(\eta)$ acting on ξ and φ , and depending on η as a parameter,

$$\mathcal{B}(\eta) = \frac{\partial}{\partial \xi} \xi \frac{\partial}{\partial \xi} + \frac{\xi + \eta}{4\xi\eta} \frac{\partial^2}{\partial \varphi^2} - \frac{\xi + \eta}{2} V(\mathbf{r}) + (E - H_{N-1}) \frac{\xi}{2} - \frac{F\xi^2}{4}. \quad (8.11)$$

In the current adiabatic approach, η is treated as the “slow” variable, similar to the internuclear distance in the BO approximation. Everything is still exact if all non-adiabatic couplings are taken into account. The η -coordinate is the relevant coordinate for tunneling, as the tunneling-ionized electron is accelerated toward $z \rightarrow -\infty$, corresponding to $\eta \rightarrow \infty$. In this limit,

$$\mathcal{B} \equiv \mathcal{B}(\eta)|_{\eta \rightarrow \infty} = \frac{\partial}{\partial \xi} \xi \frac{\partial}{\partial \xi} + \frac{1}{4\xi} \frac{\partial^2}{\partial \varphi^2} + Z + (E - H_{N-1}) \frac{\xi}{2} - \frac{F\xi^2}{4}. \quad (8.12)$$

The ionization channels are defined as eigensolutions of this operator:

$$(\mathcal{B} - \beta_\nu) \Phi_{\nu M'_S}(\mathbf{Q}_{N-1}, \xi, \varphi, \sigma) = 0. \quad (8.13)$$

One can make separation of variables

$$\Phi_{\nu M'_S}(\mathbf{Q}_{N-1}, \xi, \varphi, \sigma) = \Psi_{nM'_S}(\mathbf{Q}_{N-1}) \phi_\nu(\xi) \frac{e^{im\varphi}}{\sqrt{2\pi}} \chi_{M_S - M'_S}(\sigma), \quad (8.14)$$

where $\Psi_{nM'_S}$ is a SS of the $(N - 1)$ -electron subsystem with eigenvalues E_n , n characterizing the ionic SSs, and m the azimuthal quantum number of the outgoing electron. The quantum numbers denoted by a prime such as M'_S are quantum numbers for the $(N - 1)$ -electron subsystem. The functions ϕ_ν satisfy the boundary conditions $\phi_\nu|_{\xi \rightarrow 0} \propto \xi^{|m|/2}$ and $\phi_\nu|_{\xi \rightarrow \infty} = 0$. The channel function is thus completely characterized by the quantum numbers $m_s = M_S - M'_S$ and

$$\nu = (n, n_\xi, m), \quad (8.15)$$

with $n_\xi = 0, 1, 2, \dots$ enumerating the different solutions to Eq. (8.13) for a given n and m .

By continuity, the specification of ionization channels in terms of the quantum numbers ν can be used for all values of η . Making the ansatz for the complete solution to the N -electron TISE in (8.10),

$$\Psi(\mathbf{Q}_N) = \eta^{-1/2} \sum_{\nu M'_S} f_{\nu M'_S}(\eta) \Phi_{\nu M'_S}(\mathbf{Q}_{N-1}, \xi, \varphi, \sigma; \eta), \quad (8.16)$$

results in a differential equation for η with nonadiabatic terms including derivatives of $\Phi_{\nu M'_S}(\mathbf{Q}_{N-1})$ w.r.t. η . These terms will go to zero in the limit $\eta \rightarrow \infty$ as $\Phi_{\nu M'_S}$ ceases to depend on η . In this limit, $f_\nu(\eta)$ satisfies

$$\left[\frac{d^2}{d\eta^2} + p^2(\eta) \right] f_{\nu M'_S}(\eta) = 0, \quad (8.17a)$$

$$p^2(\eta) = \frac{F\eta}{4} + \frac{E - E_n}{2} + \frac{\beta_\nu}{\eta} + \mathcal{O}(\eta^{-2}). \quad (8.17b)$$

The strategy in WFAT is to calculate the flux going through a surface in the limit $\eta \rightarrow \infty$, and the $\mathcal{O}(\eta^{-2})$ term in Eq. (8.17) can be neglected for the leading-order WFAT. For $F > 0$ the SSs satisfy Eq. (8.17) with the outgoing boundary conditions

$$f_{\nu M'_S}(\eta)|_{\eta \rightarrow \infty} = \frac{\sqrt{2} f_{\nu M'_S}}{(F\eta)^{1/4}} \exp \left[\frac{iF^{1/2}\eta^{3/2}}{3} + \frac{i(E - E_n)\eta^{1/2}}{F^{1/2}} \right]. \quad (8.18)$$

Note the independence of the eigenvalue of the ionization channels, β_ν , in the above equation.

8.2.2 Connection formula

The weak-field ionization rate Γ depends on the channel amplitudes $f_{\nu M'_S}$. It is the purpose of the WFAT to express these in terms of the properties for the field-free bound-state wave function.

The $F = 0$ case

For $F = 0$, the solutions to Eq. (8.13) are known, given by

$$\phi_\nu^{(0)} = \kappa_n^{1/2} (\kappa_n \xi)^{|m|/2} e^{-\kappa_n \xi/2} \sqrt{\frac{n_\xi!}{(n_\xi + |m|)!}} L_{n_\xi}^{|m|}(\kappa_n \xi), \quad (8.19a)$$

$$\beta_\nu^{(0)} = Z - \kappa_n \left(n_\xi + \frac{|m| + 1}{2} \right), \quad (8.19b)$$

with $\kappa_n = \sqrt{2I_n}$, $I_n = E_n^{(N-1)} - E_0^{(N)}$ the field-free IP, and $L_{n_\xi}^{|m|}(\kappa_n \xi)$ the generalized Laguerre polynomials. The field-free bound-state wave function can be expanded similarly to Eq. (8.16) and can be shown to take the asymptotic form

$$\Psi_0^{(N)}(\mathbf{Q}_N)|_{\eta \rightarrow \infty} = N^{-1/2} \sum_{\nu M'_S} g_{\nu M'_S} \eta^{\beta_\nu^{(0)}/\kappa_n - 1/2} e^{-\kappa_n \eta/2} \Phi_{\nu M'_S}^{(0)}(\mathbf{Q}_{N-1}, \xi, \varphi, \sigma). \quad (8.20)$$

The coefficients $g_{\nu M'_S}$ can be projected out, and is given by

$$g_{\nu M'_S} = \hat{P}_\nu \left[\chi_{M_S - M'_S}^T \mathcal{Y}_{n M'_S} \right], \quad (8.21)$$

with the projection operator

$$\hat{P}_\nu [\psi(\mathbf{r})] = \eta^{1/2 - \beta_\nu^{(0)}/\kappa_n} e^{\kappa_n \eta/2} \int_0^\infty d\xi \int_0^{2\pi} d\varphi \phi_\nu^{(0)}(\xi) \frac{e^{-im\varphi}}{\sqrt{2\pi}} \psi(\mathbf{r}) \Big|_{\eta \rightarrow \infty}, \quad (8.22)$$

and the Dyson orbital

$$\mathcal{Y}_{n M'_S}(q) = \sqrt{N} \int \Psi_{n M'_S}^{(N-1)T} \Psi_0^{(N)} dV_{N-1}. \quad (8.23)$$

The $F \rightarrow 0$ case

By setting $p(\eta) = 0$ in Eq. (8.17b), the outer turning point for tunneling is obtained to be

$$\eta_t = \frac{\kappa_n^2}{F} + \mathcal{O}(F^0). \quad (8.24)$$

The outer turning point can be considered to determine the η -coordinate scale of the tunneling problem. One therefore considers the asymptotics

$$F \rightarrow 0, \quad \eta = \mathcal{O}(F^{-1}). \quad (8.25)$$

By perturbation theory,

$$E = E_0^{(N)} - \mu_{0z}^{(N)} F + \mathcal{O}(F^2) \quad (8.26a)$$

$$E_n = E_n^{(N-1)} - \mu_{nz}^{(N-1)} F + \mathcal{O}(F^2) \quad (8.26b)$$

$$\beta_\nu = \beta_\nu^{(0)} + \mathcal{O}(F) \quad (8.26c)$$

with the dipole moments

$$\boldsymbol{\mu}_0^{(N)} = - \sum_{i=1}^N \int \Psi_0^{(N)T} \mathbf{r}_i \Psi_0^{(N)} dV_N \quad (8.27a)$$

$$\boldsymbol{\mu}_n^{(N-1)} = - \sum_{i=1}^{N-1} \int \Psi_{nM'_S}^{(N-1)T} \mathbf{r}_i \Psi_{nM'_S}^{(N-1)} dV_{N-1}. \quad (8.27b)$$

Substituting Eq. (8.26) into $p^2(\eta)$ of Eq. (8.17b) and taking into account Eq. (8.25), $p^2(\eta)$ is expanded up to order $\mathcal{O}(F)$. The outgoing wave solution to Eq. (8.17) is given by a semiclassical approximation,

$$f_\nu(\eta) = \frac{C \exp[iS(\eta)]}{\sqrt{p(\eta)}}, \quad S(\eta) = \int_{\eta_t}^{\eta} p(\eta') d\eta' \quad (8.28)$$

applicable in the region $(d/d\eta)[1/p(\eta)] \ll 1$ corresponding to

$$F^{1/3} |\eta - \eta_t| \gg 1. \quad (8.29)$$

Solution matching

In the range $\eta \gg \eta_t$, matching the solution of Eq. (8.28) with Eq. (8.18) gives $C = f_{\nu M'_S} \exp(-i\pi\beta_\nu/\kappa_n)$. The matching region used to obtain $f_{\nu M'_S}$ is now discussed. In Eq. (8.17), the term involving F can be neglected for $\eta \ll \kappa_n^2/F = \eta_t$, leading to the field-free solutions (8.19). Meanwhile, the term in Eq. (8.17) involving $\beta_\nu^{(0)}$ can be neglected for $\eta \gg 4|\beta_\nu^{(0)}|/\kappa_n^2$, yielding the asymptotics in Eq. (8.18) independent of $\beta_\nu^{(0)}$. Thus the matching region is taken as

$$4|\beta_\nu^{(0)}|/\kappa_n^2 \ll \eta \ll \eta_t, \quad (8.30)$$

corresponding to the WFAT field requirement

$$F \ll F_c, \quad F_c = \frac{\kappa^4}{4|\beta_\nu^{(0)}|}. \quad (8.31)$$

The semiclassical solution in the matching region (8.30) can be obtained by analytically continuing (8.28) from $\eta > \eta_t$ to $\eta < \eta_t$ through the upper half of the complex η plane, all the while satisfying condition Eq. (8.29). After matching this solution to the $F = 0$ solution (8.20) in the matching region, one obtains the channel-amplitudes

$$f_{\nu, M'_S} = \frac{\sqrt{\kappa_n} g_{\nu M'_S}}{\sqrt{2N}} \left(\frac{4\kappa_n^2}{F} \right)^{\beta_\nu^{(0)}/\kappa_n} \exp \left[\frac{i\pi}{4} + \frac{i\pi\beta_\nu^{(0)}}{\kappa_n} - \kappa_n \mu_n - \frac{\kappa_n^3}{3F} \right] \times [1 + \mathcal{O}(F \ln F)], \quad (8.32)$$

with

$$\mu_n = \mu_{0z}^{(N)} - \mu_{nz}^{(N-1)}. \quad (8.33)$$

Ionization rate

The ionization rate in the weak-field limit can be shown to take on the form

$$\Gamma = \sum_{\nu M'_S} \Gamma_{\nu M'_S}, \quad \Gamma_{\nu M'_S} = N |f_{\nu M'_S}|^2. \quad (8.34)$$

We will assume in this thesis that the initial N -electron state is the ground state with $M_S = 0$, so that the $(N - 1)$ -electron state has spin projections $M'_S = \pm 1/2$. By realizing

$$g_\nu \equiv g_{\nu(\frac{1}{2})} = g_{\nu(-\frac{1}{2})}, \quad (8.35)$$

the sum over M'_S in Eq. (8.34) can be readily performed, yielding

$$\Gamma = 2 \sum_{n=0}^{\infty} \Gamma_n, \quad \Gamma_n = \sum_{n_\xi=0}^{\infty} \sum_{m=-\infty}^{\infty} \Gamma_\nu, \quad (8.36)$$

with Γ_n the ionization rate into a given final state n of the $(N - 1)$ -electron subsystem, and Γ_ν the ionization rate into a given ionization channel ν

$$\Gamma_\nu = |G_\nu|^2 W_\nu(F) [1 + \mathcal{O}(F \ln F)]. \quad (8.37)$$

In Eq. (8.37), G_ν is the structure factor

$$G_\nu = e^{-\kappa_n \mu_n} g_\nu, \quad (8.38)$$

and $W_\nu(F)$ is the field factor

$$W_\nu(F) = \frac{\kappa_n}{2} \left(\frac{4\kappa_n^2}{F} \right)^{2Z/\kappa_n - 2n_\xi - |m| - 1} \exp\left(-\frac{2\kappa_n^3}{3F}\right). \quad (8.39)$$

Terms in square brackets in Eq. (8.37) of orders $\mathcal{O}(F \ln F)$ or higher are neglected in the current ME-WFAT. The exponential factor in Eq. (8.39) is dominant for the smallest ionization potential, corresponding to the $(N - 1)$ -electron ground state with $n = 0$. In addition, for a given n , the dominant contribution to Γ_n is determined by the power factor with the largest exponent, corresponding to $n_\xi = m = 0$. So in this thesis we approximate the rate by its dominant term,

$$\Gamma \approx 2 |G_{000}|^2 W_{000}(F). \quad (8.40)$$

Note that our expression differs slightly compared to that used in Ref. [60], where the factor 2 is absorbed into $|G_{000}|^2$.

The range of applicability is determined by Eq. (8.31). For the example of atomic hydrogen with $Z \sim 1$ and $\kappa_0 = 1$, $F_c \sim 0.5$ corresponds to the intensity $I \sim 8.8 \times 10^{15}$ W/cm². Previously, it was shown that $\Gamma_{\text{exact}}/\Gamma_{\text{WFAT}} \approx 0.6$ at $F = 0.05$ ($I \sim 8.8 \times 10^{13}$ W/cm²). Thus, despite the terminology “weak-field”, WFAT is applicable to moderate field strengths in the current strong-field physics.

8.3 Dyson orbital in TD-GASCI

Although the formulation of the lowest-order ME-WFAT is completed, its application on complex systems still provides a challenge. As the field-dependent factor is analytically known (assuming the knowledge of the IP), the challenge is in the calculation of the structure factor, which for molecules includes the orientation-dependence of the molecule with respect to the field direction. As already demonstrated for the OE-WFAT, usage of standard quantum chemistry Gaussian basis sets to obtain the structure factor is difficult and convergence is slow [20, 144]. This is because the inaccurate long-range behaviors obtained from these basis sets are unimportant for the calculation of the ground state energy, which is the main objective in quantum chemistry. For diatomics in the HF approximation, an existing grid-based method in a prolate spheroidal basis, X2DHF [153], was shown to produce accurate long-range behavior [20, 142]. For polyatomic molecules, the usage of a polarization-consistent basis was able to obtain structure factors in the HF approximation [20]. In the multi-electron case beyond the HF approximation, the structure factor was extracted for the simplest atoms H⁻ and He [60, 154], and the simplest multielectron molecule H₂ [60]. For H₂, the asymptotic tail of the Dyson orbital was only correct up to around $r \approx 6$. All in all, the multi-electron correlation effects in static tunneling ionization of molecules have not been properly discussed. As we will show now, the TD-GASCI method for solving the TISE and TDSE for a multielectron system [See Section 2.4], combined with the ME-WFAT, provides an avenue for observation of multi-electron effects in tunneling ionization.

8.3.1 Orbital representation

Using the TD-GASCI method, we can for an N -electron (N even) system obtain the ground state energy $E_0^{(N)}$ and the ground state wave function by ITP

$$|\Psi_0^{(N)}\rangle = \sum_{I_N} C_{I_N} |I_N\rangle. \quad (8.41)$$

The multi-indices $I_N = (i_1, \dots, i_N)$ are ordered as $i_1 \leq \dots \leq i_N$, and depend on the particular GAS scheme used $I_N \in \mathcal{V}_{\text{GAS}}^{(N)}$, with i_k running up to the number of spin-orbitals $2N_b$. For notational simplicity, we have changed notation here compared to Section 2.4, and use index i for the spin-orbitals and index \tilde{i} for the spatial orbitals. The determinants $|I_N\rangle$ can be written

$$|I_N\rangle = \hat{a}_{i_1}^\dagger \cdots \hat{a}_{i_N}^\dagger |0\rangle. \quad (8.42)$$

Using the same orbital basis for the $(N-1)$ -electron system as for the N -electron system (corresponding to the same set of creation operators $\{\hat{a}_i^\dagger\}_{i=1, \dots, 2N_b}$), the $(N-1)$ -electron ground state $|\Psi_{0M'_S}^{(N-1)}\rangle$ can be calculated in the TD-GASCI,

$$|\Psi_{0M'_S}^{(N-1)}\rangle = \sum_{J_{N-1}} B_{J_{N-1}} |J_{N-1}\rangle, \quad (8.43)$$

with the multi-indices $J_N = (j_1, \dots, j_{N-1})$ ordered as $j_1 \leq \dots \leq j_{N-1}$ and depending on the particular GAS scheme used $J_{N-1} \in \mathcal{V}_{\text{GAS}}^{(N-1)}$, j_k running up to $2N_b$, and

$$|J_{N-1}\rangle = \hat{a}_{j_1}^\dagger \cdots \hat{a}_{j_{N-1}}^\dagger |0\rangle. \quad (8.44)$$

The Dyson orbital (8.23) in second quantization can now be written as

$$\begin{aligned} |\mathcal{Y}_{0M'_S}\rangle &= \langle \Psi_{0M'_S}^{(N-1)} | \Psi_0^{(N)} \rangle \\ &= \sum_{J_{N-1}} \sum_{I_N} B_{J_{N-1}}^* C_{I_N} \langle J_{N-1} | I_N \rangle \\ &= \sum_{J_{N-1}} \sum_{I_N} B_{J_{N-1}}^* C_{I_N} \hat{a}_{j_{N-1}} \cdots \hat{a}_{j_1} \hat{a}_{i_1}^\dagger \cdots \hat{a}_{i_N}^\dagger |0\rangle \\ &= \sum_{J_{N-1}} \sum_{I_N} B_{J_{N-1}}^* C_{I_N} \sum_{k=1}^N (-1)^k \delta_{j_1 i_1} \cdots \delta_{j_{k-1} i_{k-1}} \hat{a}_{i_k}^\dagger \delta_{j_k, i_{k+1}} \cdots \delta_{j_{N-1} i_N} |0\rangle \\ &= \sum_{k=1}^N (-1)^k \sum_{\substack{j_1 < \cdots < j_{k-1} < i_k \\ < j_k < \cdots < j_{N-1}}} B_{j_1 \dots j_{N-1}}^* C_{j_1 \dots j_{k-1} i_k j_k \dots j_{N-1}} \hat{a}_{i_k}^\dagger |0\rangle \\ &= \sum_{i=1}^{2N_b} \langle i | \mathcal{Y}_{0M'_S} \rangle |i\rangle, \end{aligned} \quad (8.45)$$

where we in the fourth equality used Wick's theorem to rewrite the operator string. The explicit form of the Dyson orbital in the spin-orbital representation is obtained by projection

$$\langle i | \mathcal{Y}_{0M'_S} \rangle = \sum_{k=1}^N (-1)^k \sum_{\substack{j_1 < \cdots < j_{k-1} < i \\ < j_k < \cdots < j_{N-1}}} B_{j_1 \dots j_{N-1}}^* C_{j_1 \dots j_{k-1} i j_k \dots j_{N-1}}. \quad (8.46)$$

Compared to the expression for the Dyson orbital in first quantization in Eq. (8.23), the factor \sqrt{N} is absent in Eq. (8.46). The equivalence between the first and second quantized Dyson orbitals can be demonstrated by realizing $\langle \mathbf{x} | \mathcal{Y}_{0M'_S} \rangle = (-1)^{N-1} \langle \Psi_{0M'_S}^{(N-1)} | \hat{\psi}(x) | \Psi_0^{(N)} \rangle$, and using the expression for the annihilation field operator $\hat{\psi}(x)$ given by¹

$$\hat{\psi}(x) = \sum_{n=1}^{\infty} \sqrt{n} \int d\mathbf{x}_2 \cdots \mathbf{x}_n | \mathbf{x}_2, \dots, \mathbf{x}_n \rangle \langle \mathbf{x}_2, \dots, \mathbf{x}_n |. \quad (8.47)$$

In the TD-GASCI, we assume $M_S = 0$. For a given M'_S (equal to either 1/2 or $-1/2$), $\langle i | \mathcal{Y}_{0M'_S} \rangle$ is nonzero only for spin-orbitals $|i\rangle$ with the spin projection $m_S = -M'_S$. The spin-independent Dyson orbitals in orbital representation can thus be written as

$$|\psi_D\rangle \equiv \chi_{-M'_S}^T | \mathcal{Y}_{0M'_S} \rangle = \sum_{\tilde{i}=1}^{N_b} \langle \tilde{i} | \psi_D \rangle | \tilde{i} \rangle \quad (8.48)$$

where the notation for spin projection $\chi_{-M'_S}^T$ from the previous section is used, and $| \tilde{i} \rangle = \hat{a}_{\tilde{i}}^\dagger | 0 \rangle$ are orbitals with spin projected out. In the case of HF calculations, $| \Psi_{0M'_S}^{(N-1)} \rangle = \hat{a}_1^\dagger \cdots \hat{a}_{N-1}^\dagger | 0 \rangle$, $| \Psi_0^{(N)} \rangle = \hat{a}_1^\dagger \cdots \hat{a}_N^\dagger | 0 \rangle$, and the above reduces to

$$|\psi_D\rangle = |N\rangle, \quad (8.49)$$

with $|N\rangle$ the highest occupied molecular orbital (HOMO).

The numerical implementation follows Eqs. (8.45) and (8.48). In practice, for all J_{N-1} and I_N , the overlap $\langle J_{N-1} | I_N \rangle$ is calculated in the Slater representation, yielding only a nonzero result when all indices in J_{N-1} are contained in I_N . If the remaining index in I_N is k , the term $B_{J_{N-1}}^* C_{I_N}$ (with a phase factor ± 1) is added to the coefficient d_k . For the HF case in Eq. (8.49), the HOMO orbital $|N\rangle$ from the HF calculation is used.

It should be noted that after choosing a particular GAS partition for the calculation of the N -electron wave function $| \Psi_0^{(N)} \rangle$, the same GAS partition must be made for the calculation of $| \Psi_{0M'_S}^{(N-1)} \rangle$. For example, when the GAS-scheme CAS*(2, K) is used for the N -electron system, the GAS-scheme CIS-v must be used for the $(N-1)$ -electron system to ensure a consistent GAS partition.

¹DOI:10.1021/acs.jpca.5b09444

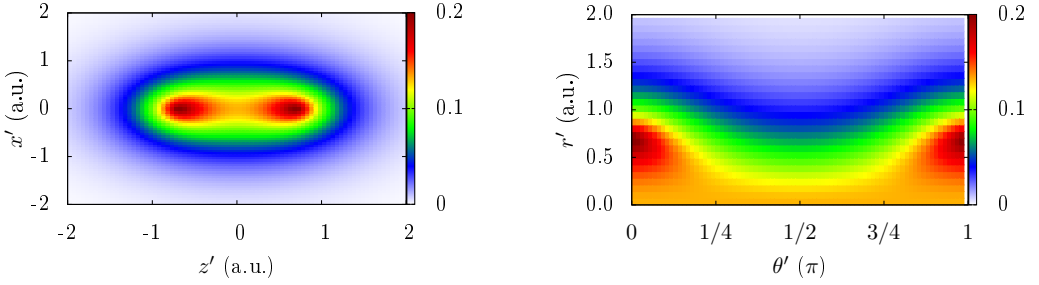


Figure 8.1: Dyson orbital probability density for H_2 , calculated using TD-GASCI in the CIS partition scheme, with $R = 1.4011$. Left: $|\psi_D(x', y' = 0, z')|^2$ in Cartesian coordinates. Right: $|\psi_D(r', \theta', \varphi' = 0)|^2$ in spherical coordinates. The primes in the coordinate labels refer to the molecular frame coordinate system.

8.3.2 Spatial representations

In spatial representation, the Dyson orbital is given by

$$\psi_D(\mathbf{r}) = \langle \mathbf{r} | \psi_D \rangle = \sum_{\tilde{i}=1}^{N_b} \langle \tilde{i} | \psi_D \rangle \langle \mathbf{r} | \tilde{i} \rangle. \quad (8.50)$$

For diatomic molecules, we use the FEDVR basis in prolate spheroidal coordinates as the primitive basis set in the TD-GASCI calculations. The Dyson orbital in these coordinates is

$$\psi_D(\zeta, \mu, \phi) = \langle \zeta, \mu, \phi | \psi_D \rangle = \sum_{\tilde{i}=1}^{N_b} \langle \tilde{i} | \psi_D \rangle \langle \zeta, \mu, \phi | \tilde{i} \rangle. \quad (8.51)$$

Representation of the the Dyson orbitals in another coordinate system $(\lambda_1, \lambda_2, \lambda_3)$ can be obtained by a coordinate transformation

$$\begin{aligned} \psi_D(\lambda_1, \lambda_2, \lambda_3) &= \langle \zeta, \mu, \phi | \psi_D \rangle \\ &= \psi_D[\zeta(\lambda_1, \lambda_2, \lambda_3), \mu(\lambda_1, \lambda_2, \lambda_3), \phi(\lambda_1, \lambda_2, \lambda_3)]. \end{aligned} \quad (8.52)$$

Some useful coordinate transformations between spherical, prolate spheroidal, and parabolic coordinates are given in Appendix D. As an example, the Dyson orbital for H_2 with the molecular axis oriented along z is shown in Figs. 8.1 in Cartesian and spherical coordinates.

8.4 Structure factor

The ionization rate depends on the orientation of the linear molecule w.r.t. the polarization direction of the static electric field \mathbf{F} only through the structure

factor in Eq. (8.38). We introduce the molecular-frame position vector $\mathbf{r}' = \hat{R}\mathbf{r}$, with \hat{R} the Euler rotation from the laboratory frame to the molecular frame. We use the convention that the z axis is directed along the linear polarized electric field, the z' axis along the internuclear axis lies in the xz plane, and the y and y' axis coincide. Now the orientation of the linear molecule can be described by the single angle $\beta \in [0, \pi]$, defining the rotation from z to z' about the y -axis,

$$\begin{aligned} x' &= x \cos \beta - z \sin \beta \\ z' &= x \sin \beta + z \cos \beta. \end{aligned} \quad (8.53)$$

All equations in the previous sections are given in the laboratory frame, with the β -dependency being implicit in $\psi_D(\mathbf{r})$ (8.50) and μ_n (8.33).

We now sketch the procedure used to calculate the structure factor. The desired structure factor is

$$G_{000}(\beta) = \lim_{\eta \rightarrow \infty} G_{000}(\beta; \eta) = e^{-\kappa_0 \mu_0} \lim_{\eta \rightarrow \infty} g_{000}(\beta; \eta), \quad (8.54)$$

where the structure coefficient is given by the projection in Eqs. (8.21) and (8.22) such that

$$g_{000}(\beta; \eta) = \frac{1}{\sqrt{2\pi}} \eta^{1/2 - \beta_\nu^{(0)}/\kappa_0} e^{\kappa_0 \eta/2} \int_0^\infty \phi_\nu^{(0)}(\xi) \int_0^{2\pi} \psi_D(\mathbf{r}) d\varphi d\xi. \quad (8.55)$$

To perform the integral in Eq. (8.55), we need the Dyson orbital in parabolic coordinates in the laboratory frame. Numerically, parabolic spatial quadrature grid $(\xi_i, \eta_j, \varphi_k)$ is first chosen such that the integration can be conveniently performed. We use Laguerre quadrature [see Appendix A] for the ξ coordinate and a equidistant grid points for φ . The parabolic grid is transformed into Cartesian coordinates using Eq. (D.9), which afterwards is transformed into the molecular frame Cartesian coordinates by Eq. (8.53). Lastly, this molecular Cartesian grid is transformed into the corresponding prolate spheroidal grid, were the Dyson orbital can be evaluated using the rotated basis in the TD-GASCI [see Subsection 3.4.2]. Using this procedure, we obtain the Dyson orbital in the parabolic quadrature grid $\psi_D(\xi_i, \eta_j, \varphi_k)$, which is integrated according to Eq. (8.55) to obtain the structure coefficient $g_{000}(\beta; \eta)$. The calculation of the orientation-dependent Dyson orbitals, which numerically is the most time-consuming part, only needs to be performed once. The z component of the dipole moment on the μ_n is given in terms of the z' component μ'_n by the relation

$$\mu_n = \mu'_n \cos \beta. \quad (8.56)$$

The $G_{000}(\beta; \eta)$ can hereby calculated. We will henceforth denote all relevant quantities given in the molecular frame with a prime.

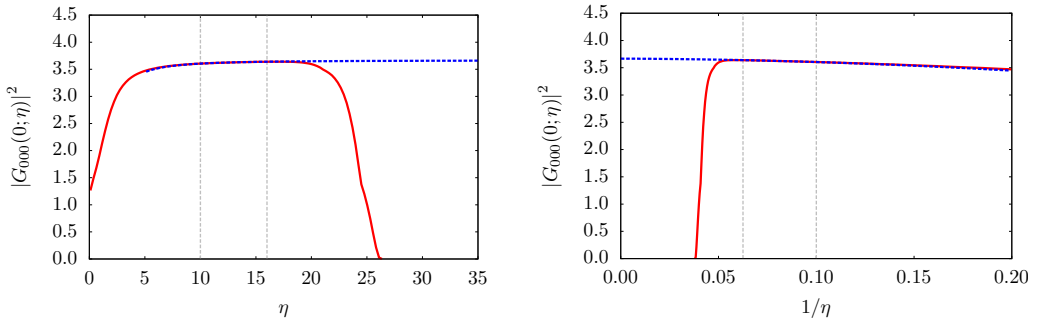


Figure 8.2: Red solid curves: $|G_{000}(\beta; \eta)|^2$ for H_2 with $R = 1.4011$ calculated using TD-GASCI in HF approximation. Blue dashed curves: fits according to Eq. (8.57), with $N_{\text{fit}} = 80$ and $N_{\text{deg}} = 2$. The vertical dotted lines indicate the fitting interval $\eta_{\text{min}} = 10$ and $\eta_{\text{max}} = 16$. We extract at $1/\eta = 0$ the structure factor $|G_{000}(\beta = 0)|^2 = 3.67$.

Our numerical η -grid is finite, so obtaining the structure factor $G_{000}(\beta)$ in Eq. (8.54) by taking the limit $\eta \rightarrow \infty$ needs a mention. We consider $G_{000}(\beta; \eta)$ as a function $1/\eta$ with N_{fit} points in the interval $[1/\eta_{\text{max}}, 1/\eta_{\text{min}}]$, and fit it with a polynomial of degree N_{deg} ,

$$G_{000}(\beta; \eta) = \sum_{n=0}^{N_{\text{deg}}} c_n(\beta) \left(\frac{1}{\eta}\right)^n. \quad (8.57)$$

The structure factor is then the coefficient $G_{000}(\beta) = \lim_{\eta \rightarrow \infty} G_{000}(\beta; \eta) = c_0(\beta)$. We choose $N_{\text{fit}} = 80$ and $N_{\text{deg}} = 2$ in our calculations. The choice of η_{max} and η_{min} will vary, as $G_{000}(\beta; \eta)$ can show unphysical non-monotonic behavior at large η due to the choice of the primitive basis and different CAS partition schemes. We must choose η_{max} smaller than the distance corresponding the onset of such behaviors.

In Fig. 8.2 we show an example of this fitting procedure for H_2 in the HF approximation. The prolate spheroidal basis parameters used in the TD-GASCI calculations are given in Table 8.1. We extract $|G_{000}(\beta = 0)|^2 = 3.67$.

8.4.1 Structure factor for H_2

In Fig. 8.3 we present the η -dependent structure factors for H_2 in different CAS-partitions using the rotated pseudo-orbital basis [see Subsection 3.4.2]. The prolate basis parameters used and the η interval used for fitting the structure factor are given in Table 8.1. For $m'_{\text{max}} = 0$ in the upper figure, it is seen that for CAS*(2, 20)-0, the smallest CAS space considered, unphysical oscillations are seen at $\eta \approx 12$ due to the too small CAS space used. For CAS*(2, 40)-0, the unphysical oscillations has died out on the scale of the figure. The extension -0 (-1)

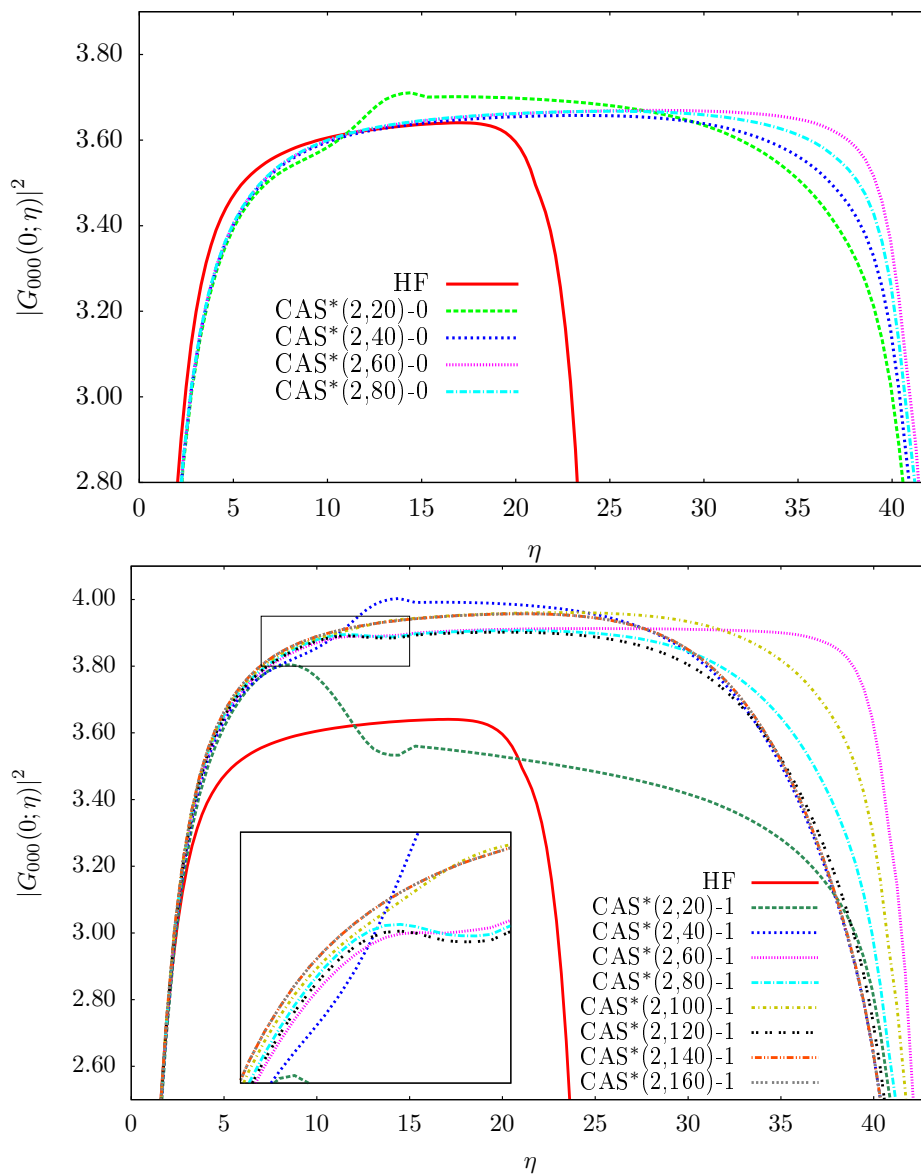


Figure 8.3: Structure factor squared $|G_{000}(0; \eta)|^2$ calculated for H_2 with $R = 1.4011$ calculated in different CAS-partitions. Upper figure $m'_{\max} = 0$; lower figure $m'_{\max} = 1$. The inset is a zoom of the rectangular area.

Table 8.1: TD-GASCI Prolate spheroidal basis parameters used for H_2 with $R = 1.4011$. The extension -0 (-1) in a method denotes $m'_{\text{max}} = 0$ ($m'_{\text{max}} = 1$) used in the prolate basis. N_μ is the number of μ -coordinate DVR functions. ζ_{FE} gives the FE boundaries with the vertical line separating the inner and outer regions, and the dots indicating equidistant FE in the outer region. N_ζ is the number of ζ -coordinate DVR functions in each FE, and we use same number of DVR functions in each FE in the outer region. The energies are converged to the fifth decimal w.r.t. to the prolate spheroidal basis parameters. The total number of spatial orbitals in the inner region is 168 for $m'_{\text{max}} = 0$ and 504 for $m'_{\text{max}} = 1$.

Method	N_μ	ζ_{FE}	N_ζ	$[\eta_{\text{min}}, \eta_{\text{max}}]$
HF	8	(1 2 4 7 11 15 19)	(4 6 7 8 8 8)	[10,16]
CAS*(2,-)0	8	(1 2 4 7 11 15.2 ... 32)	(4 6 7 8 8 ...)	[10,20]
CAS*(2,-)1	8	(1 2 4 7 11 15.2 ... 32)	(4 6 7 8 8 ...)	[10,20]

in a CAS method denotes $m'_{\text{max}} = 0$ ($m'_{\text{max}} = 1$) used in the prolate basis. For CAS*(2,80)-0, a sufficiently high number of diffuse orbitals are included in the calculation, and the result is fully converged w.r.t. the CAS space. To correctly include correlations TD-GASCI, orbitals with higher azimuthal quantum number must be taken into account. The case m'_{max} is shown in the lower subfigure of Fig. 8.3. Again unphysical oscillations are present, with convergence observed for CAS*(2,140)-0 and CAS*(2,160)-0. Note that for both $m'_{\text{max}} = 0$ and $m'_{\text{max}} = 1$, the converged CAS space is much smaller than the largest possible CAS spaces (CAS*(2,168)-0 and CAS*(2,504)-0, respectively).

For the HF and the converged CAS-partitions, we calculate for each angle β the structure factors $G_{000}(\beta)$ by the fitting procedure described in the previous subsection. The results are shown in Fig. 8.4. First we notice that our current HF result agrees very well with previous result by Saito et al. [142], with the largest rate at $\beta = 0$ and $\beta = \pi$ when the molecule is aligned along the polarization direction of the electric field. This can be understood physically by remembering that in the molecular frame, the Dyson orbital (HOMO in this case) density is largest near the two nuclei at $z' = \pm R/2$ [see e.g. Fig. 8.5]. At the orientation $\beta = \pi/2$, tunneling ionization mostly occurs along the z -axis where the Dyson density is low, which leads to a lower structure factor.

For the CAS*(2,80)-0 case, the structure factors are similar to the HF case near $\beta = 0$ and $\beta = \pi$, while the value is reduced at $\beta = \pi/2$. The smaller structure factor can be explained by the population of σ^* orbitals with $m' = 0$ and a nodal xy -plane at $z' = 0$, which will contribute to the rate at $\beta = 0$, but not at $\beta = \pi/2$. This explanation is in agreement with the lower subfigure of Fig. 8.5, where the Dyson orbital for the CAS*(2,80)-0 calculation is plotted. We indeed observe less density in the $\theta' = \pi/2$ direction, consistent with the population of

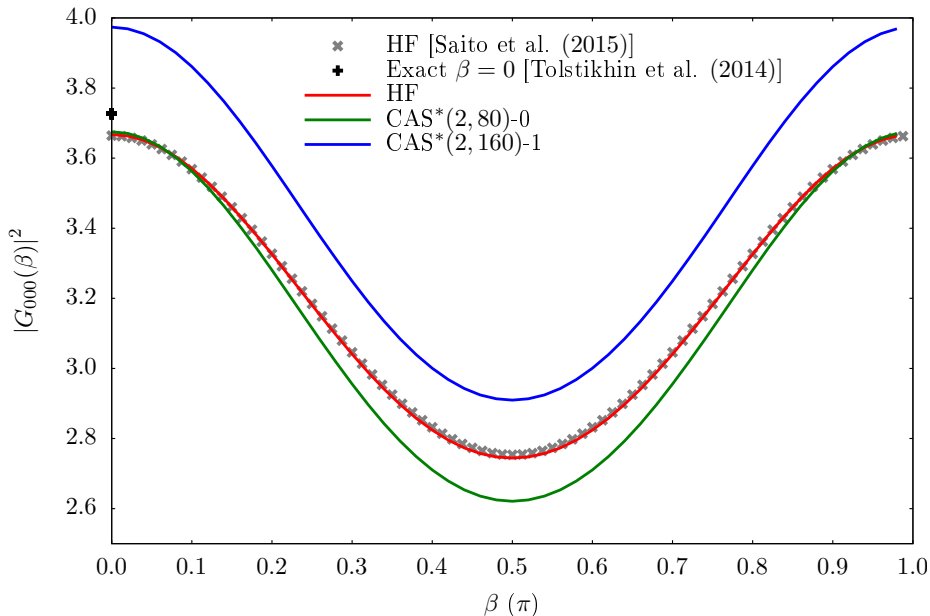


Figure 8.4: Orientation-dependent structure factor calculated for H_2 with $R = 1.4011$ and different CAS-partitions.

σ^* orbitals.

In Fig. 8.4, the structure factor for the CAS*(2, 160)-1 scheme is consistently larger than the CAS*(2, 80)-0 result for all β . At first glance, this result is quite counterintuitive since the included π -orbitals with $m' = 1$ have a nodal plane containing the z' -axis, and should not contribute to the ionization rate at $\beta = 0$. However, this naive argument does not apply in the correlated multi-electron case. Indeed, the inclusion of the π -orbitals allows in the CI-expansion of the two-electron initial state the Slater-determinant $|\sigma, \pi\rangle$, describing one electron in a σ -orbital and another electron in a π -orbital, with the corresponding CI coefficient $C_{\sigma, \pi}$. When projected onto the one-electron ion in the π -state $|\pi\rangle$ with CI-coefficient B_π , an extra term $-B_\pi C_{\sigma, \pi}$ is added to the σ -orbital amplitude of the Dyson orbital $\langle \sigma | \psi_D \rangle$ [see Eq.(8.48)], which is not present in the case of CAS*(2, 80)-0. This simple argument is not a proof of the larger structure factor in CAS*(2, 160)-1, but hints at the possibility of having a greater population of σ -states when the π orbitals are taken into account, as well as demonstrating that multi-electron correlation effects are hard to interpret. As seen in Fig. 8.4, at $\beta = 0$, our result does not coincide with that in Ref. [60]. The reason for the discrepancy could be due to the small interval used ($1 \leq r \leq 5$) in their fitting procedure.

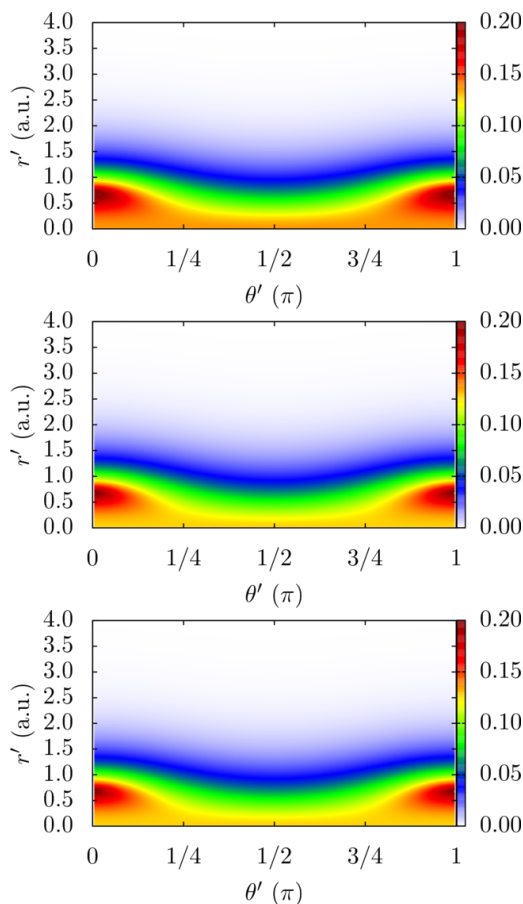


Figure 8.5: Dyson orbital probability density for H_2 in spherical coordinates $|\psi_{\text{D}}(r', \theta', \varphi' = 0)|^2$, calculated using TD-GASCI in the HF approximation (upper figure), CAS*(2,120)-0 (middle figure), and CAS*(2,160)-1 (bottom figure), with $R = 1.4011$. The primes in r' and θ' refer to the molecular frame coordinate system.

8.4.2 Structure factor for LiH

In Fig. 8.6 we present the η -dependent structure factor for LiH in different CAS-partitions using the pseudo-orbital basis, assuming two electrons are frozen in the two lowest bound spin-orbitals [see Fig. 2.3]. The prolate basis parameters used and the η interval used for fitting the structure factor are given in Table 8.2. For $m'_{\text{max}} = 0$ in the upper subfigure of Fig. 8.6, with increasing CAS space, the unphysical oscillations decrease in amplitude and eventually disappears for CAS*(2,120). For the $m'_{\text{max}} = 1$ case in the lower subfigure, the convergence is achieved at least up to $\eta = 17$ for CAS*(2,180). A calculation for a larger CAS-space with the presently used version of the TD-GASCI code is not possible due

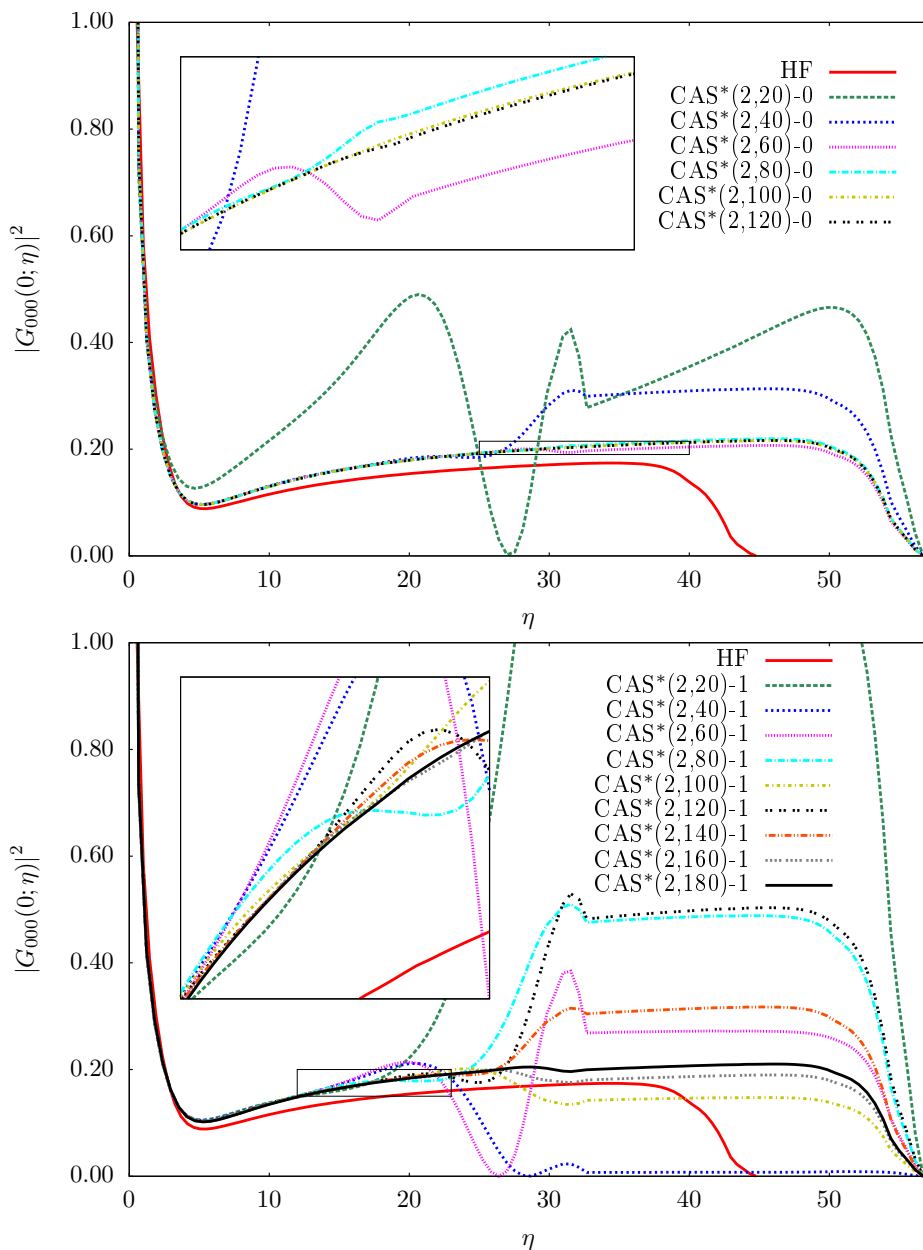


Figure 8.6: Structure factor squared $|G_{000}(0; \eta)|^2$ calculated for LiH with $R = 3.0139$ and in different CAS-partitions. Upper figure $m'_{\max} = 0$; lower figure $m'_{\max} = 1$. The insets are zooms of the rectangular areas.

Table 8.2: TD-GASCI Prolate spheroidal basis parameters used for LiH with $R = 3.0139$. The notation is the same as Table. 8.1. The HF energy is converged to the third decimal w.r.t. to the prolate spheroidal basis parameters. The total number of spatial orbitals in the inner region is 192 for $m'_{\max} = 0$ and 552 for $m'_{\max} = 1$.

Method	N_μ	ζ_{FE}	N_ζ	$[\eta_{\min}, \eta_{\max}]$
HF	8	(1 2 4 7 11 15)	(6 7 7 8 8)	[10,20]
CAS*(2,·)-0	8	(1 2 4 7 11 15 19)	(6 7 7 8 8 ...)	[20,40]
CAS*(2,·)-1	8	(1 2 4 7 11 15 19)	(6 7 7 8 8 ...)	[10,17]

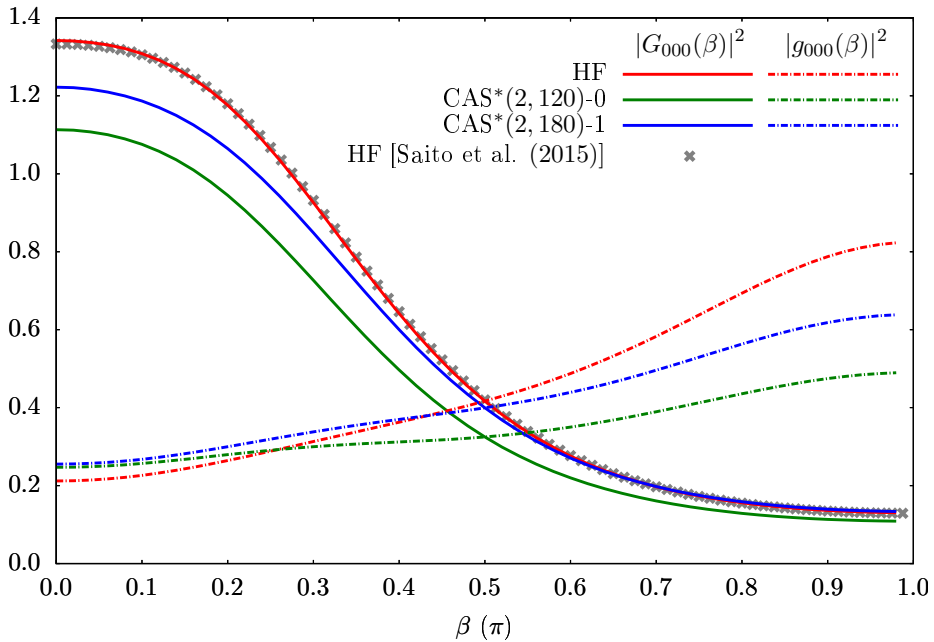


Figure 8.7: Orientation-dependent Structure factor calculated for LiH at $R = 3.0139$ with different CAS-partitions. Solid lines: $|G_{000}(\beta)|^2$. Dashed dotted lines: $|g_{000}(\beta)|^2$ in Eq. (8.55) excluding the dipole factor.

to memory problems in storing the sparse CI matrix. However, an implementation of the CI-matrix and CI-vector multiplication wherein the CI-matrix is not explicitly stored is already implemented by L. K. Sørensen et. al. The current implementation of the Dyson-orbital and ME-WFAT can straight-forwardly be combined with such a TD-GASCI implementation, and is planned for the future. Nevertheless, the structure factor can still be extracted by fitting the η -interval [10, 17] [Table 8.2], albeit with slightly less accuracy compared to previous fits.

The orientation-dependent structure factors in Eq. (8.55), with $|G_{000}(\beta)|^2$ including the dipole factor $e^{-\kappa_0 \mu_0}$ and $|g_{000}(\beta)|^2$ excluding the dipole factor, are

presented in Fig. 8.7. We note that for the LiH calculation, the Li atom is placed at $z' = -R/2$ and H atom at $z' = R/2$. In the HF case, $|g_{000}(\beta)|^2$ is largest at $\beta = \pi$, meaning that if the permanent dipole is neglected, the molecule is most likely to ionize when the internuclear vector \mathbf{R} from Li to H is aligned antiparallel with the electric field \mathbf{F} . The reason for this can be simply understood by considering the Dyson orbital density plotted in Fig. (8.8), where the charge density is observed to be greatest at the H-end of the molecule. When $\beta = \pi$, the tunnel exit is at the H-end, and greater charge density leads to greater ionization probability. However, when the dipole factor is taken into account, the situation is seen to be reversed in Fig. 8.7, with $|G_{000}(\beta)|^2$ attaining maximum at $\beta = 0$. Indeed, for $\beta = 0$ the dipole moment $\mu_0 = \mu'_0 = -1.1876$ is negative (pointing in the negative z direction), with the exponential factor $e^{-\kappa_0\mu_0}$ attaining its maximum. With increasing β , the dipole changes according to Eq. (8.56), until the dipole factor attains its minimum at $\beta = \pi$. Our HF result for LiH again agrees with Ref. [142].

For the correlated CAS*(2,120)-0 results in Fig. 8.7, the overall behavior is similar to the HF results. The structure coefficient $|g_{000}(\beta)|^2$ is slightly larger than the HF result at $\beta = 0$, while being quite smaller at $\beta = \pi$. By considering the Dyson orbital for CAS*(2,120)-0 in Fig. 8.8 we see that the density near the H atom is reduced compared to HF, leading to the large decrease of $|g_{000}(\beta)|^2$ at orientation angle $\beta = \pi$. The decrease of density near the H atom, however, also decreases the magnitude of the dipole moment $|\mu'_0|$ ($\mu'_0 = -1.004$), leading to a decrease of $|G_{000}(\beta)|^2$ at $\beta = 0$ for the correlated CAS*(2,120)-0 case.

With the inclusion of π -orbitals in CAS*(2,180)-1, it is seen in Fig. 8.7 that $|g_{000}(0)|^2$ is unchanged compared to CAS*(2,120)-0, while $|g_{000}(\pi)|^2$ is increased. The increased density at the H-end also increases the magnitude of the dipole moment $\mu_0 = -1.0187$ compared to CAS*(2,120)-0, leading to an increase of the structure factor $G_{000}(\beta)$ at $\beta = 0$.

8.5 Conclusion

We have presented a new scheme to obtain the orientation-dependent structure factors and ionization rates for diatomic molecules. This is done by first calculating the relevant energies, dipole moments, and Dyson orbitals in the TD-GASCI method by ITP and then applying the ME-WFAT. This allowed us to calculate, for the first time, correlation effects in the orientation-dependent structure factors $|G_{000}(\beta)|^2$ for H₂ and LiH, where correlation effects are shown to be non-negligible.

The current implementation has several advantages. First, correlation effects

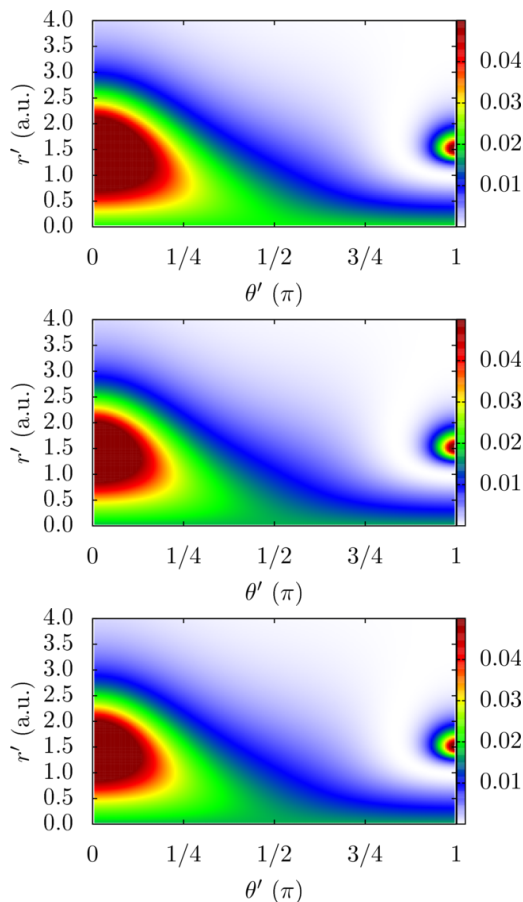


Figure 8.8: Dyson orbital probability density for LiH in spherical coordinates $|\psi_D(r', \theta', \varphi' = 0)|^2$, calculated using TD-GASCI in the HF approximation (upper figure), CAS*(2,120)-0 (middle figure), and CAS*(2,180)-1 (bottom figure) with $R = 3.0139$. The primes in r' and θ' refer to the molecular frame coordinate system.

can be included systematically in the TD-GASCI, e.g. by freezing the two core electrons in LiH, and without the need to include the total CAS-space for convergence. Second, the TD-GASCI is a grid-basis based method, and can readily obtain the asymptotic part of Dyson orbital which is required in the ME-WFAT. This is in contrast to quantum chemistry methods that focuses on the ground state energies for which the asymptotic part of the wave function is unessential. Also, the ME-WFAT, being a static field theory, can truly capture the tunneling ionization effect without the host of phenomena in time-dependent calculations such as core-polarization and electron-rescattering that are difficult to analyse.

One notable drawback of this scheme is the fact that TD-GASCI, being a grid-based method, needs a extremely dense grid to describe the core orbitals for

a many-electron system (think of $e^{-Zr/n}$ scaling for a hydrogen-like atom). However, experience has shown us that the structure factor is somewhat insensitive to the converged ionization energy. As long as the energy is somewhat converged, the structure factor remains the same. It is our wish to apply the current scheme to more complex diatomics where unresolved outstanding questions remain.

CHAPTER 9

SUMMARY AND OUTLOOK

This work was primarily concerned with the strong-field-induced breakup of diatomic molecules. The studied processes include ionization, dissociation, and dissociative ionization (DI).

For the study of dissociation and DI, the time-dependent Schrödinger equation (TDSE) for a reduced-dimensionality model of H_2^+ was numerically solved, with the electronic and a nuclear degrees of freedom treated fully quantum mechanically without the use of the Born-Oppenheimer approximation. The time-dependent surface flux method, a method for the efficient extraction of differential atomic spectra from the TDSE calculations, was formulated and implemented to treat molecular breakup of H_2^+ . Using this, the channel-resolved nuclear kinetic energy release (NKER) spectra for dissociation, as well as the joint-energy spectra (JES) for DI showing the electron-nuclei continuum-energy sharing, could be obtained.

When H_2^+ was irradiated by intense extreme ultraviolet (XUV) laser pulses, distinct interference patterns in the JES appeared. An essential state expansion of the wave function consisting of the ground state and the continuum states allowed for the interpretation of the main features in the JESs in terms of the dynamic interference effect. The dynamic interference effect, which previously has been predicted in atoms, is a process where ionized electronic wave packets with equal continuum energies created during the rising and falling edges of a laser pulse interfere in the continuum.

An investigation of H_2^+ in the very intense, XUV laser pulse regime revealed that the molecule stabilized w.r.t. ionization, i.e. that the ionization rate decreased with increasing laser intensities. However, in a certain laser parameter regime, highly non-resonant dissociation channels were shown to completely dominate over ionization, leading to unity probability for molecular breakup. This novel mechanism was understood by considering the field-dressed Born-Oppenheimer potential energy curves in the reference frame following a free elec-

tron in the field, and a model was proposed that characterizes the dissociation mechanism, as well as predicting the control of the NKER spectra and the total vibrational excitation of the population.

Based on recent discoveries, in the JES of DI the electron and nuclei either shared the photon energies between them, which emerged as diagonal structures in the JES, or the electron took all the photon energy, which were imprinted as vertical structures in the JES. It was shown in this thesis that in addition to the mentioned structures, unintuitive cross-diagonal structures in the JES could emerge. Using a strong-field approximation model wherein the nuclear energy was included, we were able to relate the cross-diagonal structures to interferences between DI wave packets released during the same subcycle of the pulse. Furthermore, the diagonal structures in the JES could be related to the interferences between wave packets released in different optical cycles. For a flat-top laser pulse, analytic expressions for these intra- and intercycle interference effects were obtained that should be applicable to a general diatomic molecule.

Tunneling ionization constitutes the first step in a range of strong-field phenomena, and an accurate description of the process is of great importance. The multi-electron weak-field asymptotic theory (ME-WFAT) was employed for this purpose to study the orientation-dependent static tunneling ionization rate in H_2 and LiH . The asymptotic tail of the Dyson orbital required in the ME-WFAT was extracted from the time-dependent generalized-active-space (TD-GASCI) method, which could include electron correlations consistently. The inclusion of correlations in H_2 and LiH was shown to have a sizable effect on the orientation-dependent ionization rate.

The TD-GASCI method was originally designed to treat time-dependent multi-electron problems. A efficient flux method to obtain the photoelectron angular distributions and the photoelectron momentum spectra was derived, and implemented in the TD-GASCI for a 1D He model for testing.

With the rapid development in laser technology, and pan-european projects such as the Extreme Light Infrastructure¹ and the European x-ray free electron laser² (both operational next year), the peak laser intensities are expected to grow. Experimental verifications of the above-predicted breakup dynamics in the very intense XUV regime thus lies within the realm of possibility. For the theoretically predicted intra- and intercycle interference in DI with infrared pulses, all components for a possible experimental verification are available even today, and it is hoped that the work in this thesis can stimulate such experiments. In the case of the orientation-dependent static field tunneling ionization for multi-

¹<https://eli-laser.eu/>

²<http://www.xfel.eu/>

electron diatomics, the plan is to apply the used scheme to more complicated systems like CO, where discrepancies between theories and experiments exist. By including the electron correlations, it is hoped that some discrepancies can be clarified.

On the theoretical front, one could consider a model of H_2^+ in the axial-recoil approximation, with the electron allowed to move in a plane containing the internuclear axis. Such a model would allow the study of molecular breakup processes with parallel and perpendicular linearly polarized laser fields, as well as circularly polarized, and orthogonal-polarized two-color laser pulses. Combined with the tSURFF method and a complex absorber, differential spectra could be extracted in a relatively small simulation volume, making the propagation of the TDSE somewhat feasible. For linearly polarized pulses along the internuclear axis, cylindrical coordinates could be used to solve the full-dimensionality TDSE for H_2^+ in the axial-recoil approximation [155, 156]. Aside from obtaining verifications of the predicted strong-field effects in this thesis, the flexibility of these models allows the study of other observables such as the emission-angle-dependent JES.

The observed strong-field phenomena were obtained for a one-electron molecule. It would be interesting to study how the multi-electron effects will change the findings presented in this thesis. For the inter- and intracycle interference, a small change is expected, since strong-field physics in the infrared frequency regime is the physics of the valence electrons. For the intense XUV pulses, ionization from inner shells could possibly dominate, leading to different dynamics. However, in Chapter 6, it was argued that our findings might still hold. To solve the TDSE including nuclear motion and multiple electrons, one can resolve to reduced-dimensionality models, or multi-electron methods such as the multi-configurational time-dependent Hartree Fock [69].

APPENDIX A

GAUSSIAN QUADRATURES AND THE FINITE-ELEMENT DISCRETE VARIABLE REPRESENTATION

In this appendix Gaussian quadratures, discrete variable representation (DVR) [84] and finite-element DVR (FE-DVR) [85] are presented.

A.1 Gaussian quadrature

An integral of a function $f(x)$ over an interval $x \in [a, b]$ can be approximated by a Gaussian quadrature [89]

$$\int_a^b W(x)f(x)dx \approx \sum_{j=0}^{N_b-1} \omega_j f(x_j), \quad (\text{A.1})$$

with $\{x_j\}_{j=0}^{N_b-1}$ the quadrature points and $\{\omega_j\}_{j=0}^{N_b-1}$ the quadrature weights. The integral in Eq. (A.1) is exact if $f(x)$ is a polynomial of degree $2N_b - 1$ or less. To obtain the quadrature points and weights, a set of orthogonal polynomials $\{p_m(x)\}_{m=0}^N$ is constructed, with m denoting the polynomial order. The quadrature points are then defined as the roots of $p_N(x)$, and the weights are given by

$$\omega_i = \frac{\int_a^b W(x)p_{N-1}^2(x)dx}{p_{N-1}(x_i)p'_N(x_i)}. \quad (\text{A.2})$$

A.1.1 Gauss-Legendre quadrature

For Gauss-Legendre quadratures, $W(x) = 1$ and the polynomials $\{p_j(x)\}_{j=0}^{N-1}$ are chosen as Legendre polynomials defined in the interval $x \in [-1, 1]$. The

quadrature points \tilde{x}_i and weights $\tilde{\omega}_i$ can be scaled to an arbitrary integration interval $[a, b]$ by the relations

$$\begin{aligned}\omega_i &= \frac{b-a}{2} \tilde{\omega}_i \\ x_i &= \frac{1}{2} [(b+a)\tilde{x}_i + (b-a)].\end{aligned}\tag{A.3}$$

A similar quadrature, the Gauss-Radau quadrature, where one of the end points of the integration interval is chosen as a quadrature point, is given by

$$\int_{-1}^1 f(x) dx \approx \frac{2}{N_b^2} f(-1) + \sum_{i=1}^{N_b-1} \omega_i f(x_i).\tag{A.4}$$

In this quadrature, the quadrature points are roots of

$$[p_{N-1}(x) + p_N(x)]/(1+x),\tag{A.5}$$

and the weights are

$$\omega_i = \frac{1}{(1-x_i)[p'_{N-1}(x_i)]^2}.\tag{A.6}$$

If $f(x)$ is a polynomial of order $2N_b - 2$ or less, Gauss-Radau quadrature is exact.

If both end points of the integration interval are included,

$$\int_{-1}^1 f(x) dx \approx \frac{2}{N_b(N_b-1)} [f(-1) + f(1)] + \sum_{i=1}^{N_b-2} \omega_i f(x_i).\tag{A.7}$$

the resulting quadrature is the Gauss-Lobatto quadrature. The quadrature points are roots of $p_{N-1}(x)$ and the weights are

$$\omega_i = \frac{2}{N_b(N_b-1)[p'_{N-1}(x_i)]^2}.\tag{A.8}$$

Gauss-Lobatto integration is exact for polynomials of order $2N_b - 3$ or less.

A.1.2 Other Gaussian quadratures

Other Gaussian quadratures constructed using classical polynomials include

$$\text{(Gauss-Chebyshev)} \quad W(x) = (1-x^2)^{-1/2}, \quad x \in [-1, 1],\tag{A.9}$$

$$\text{(Gauss-Laguerre)} \quad W(x) = x^\alpha e^{-x}, \quad x \in [0, \infty],\tag{A.10}$$

$$\text{(Gauss-Hermite)} \quad W(x) = e^{-x^2}, \quad x \in [-\infty, \infty],\tag{A.11}$$

$$\text{(Gauss-Jacobi)} \quad W(x) = (1-x)^\alpha(1+x)^\beta, \quad x \in [0, \infty].\tag{A.12}$$

A.2 Discrete variable representation

A DVR basis can be constructed from a Gaussian quadrature rule. For a given set of normalized orthogonal polynomials $\{p_m(x)\}_{m=0}^{N_b-1}$, the related functions

$$\phi_m(x) = \sqrt{W(x)}p_m(x) \quad (\text{A.13})$$

are defined. In this basis, for $0 \leq m, n \leq N_b - 1$, the orthonormality condition and the matrix elements of x given by

$$\delta_{mn} = \int_a^b \phi_m(x)\phi_n(x)dx = \sum_{i=1}^{N_b} \frac{\omega_i}{W(x_i)} \phi_m(x_i)\phi_n(x_i), \quad (\text{A.14a})$$

$$X_{mn} = \int_a^b \phi_m(x)x\phi_n(x)dx = \sum_{i=1}^{N_b} \frac{\omega_i}{W(x_i)} x_i \phi_m(x_i)\phi_n(x_i), \quad (\text{A.14b})$$

are exact within the quadrature rule, due to $p_m(x)p_n(x)$ and $xp_m(x)p_n(x)$ being polynomials of order $2N_b - 1$ or less. Denoting now the $N_b \times N_b$ transformation matrix elements as

$$T_{im} = \sqrt{\frac{\omega_i}{W(x_i)}} \phi_m(x_i), \quad (\text{A.15})$$

the relations in Eq. (A.14) are equivalent to

$$\mathbf{I} = \mathbf{T}^\dagger \mathbf{T}, \quad (\text{A.16a})$$

$$\mathbf{X} = \mathbf{T}^\dagger \mathbf{X}^{\text{DVR}} \mathbf{T}, \quad (\text{A.16b})$$

where \mathbf{X}^{DVR} is a diagonal matrix with the quadrature points in the diagonal. The transformation matrix \mathbf{T} in Eq. (A.16a) is seen to be unitary, and the quadrature points can be obtained by a diagonalization of the tridiagonal matrix \mathbf{X} . The basis wherein x is diagonal is denoted as the DVR basis, with the basis functions given by

$$\theta_i(x) = \sum_{m=0}^{N_b-1} T_{im}^* \phi_m(x). \quad (\text{A.17})$$

Using Eqs. (A.14)-(A.16), the DVR functions at the quadrature points can be evaluated, yielding

$$\theta_i(x_j) = \sqrt{\frac{W(x_j)}{\omega_j}} \delta_{ij}. \quad (\text{A.18})$$

Hence the i th DVR function is localized near x_i , in the sense that it is nonzero at x_i and zero at all other quadrature points. With this, the DVR functions can

be shown to be orthonormal:

$$\begin{aligned} \int_a^b \theta_i(x)\theta_j(x)dx &= \sum_{k=0}^{N_b-1} \frac{\omega_k}{W(x_k)} \theta_i(x_k)\theta_j(x_k) \\ &= \sum_{k=0}^{N_b-1} \delta_{ik}\delta_{jk} = \delta_{ij}. \end{aligned} \tag{A.19}$$

In the DVR, the potential energy matrix elements are evaluated using the quadrature rules,

$$\begin{aligned} V_{ij} &= \int_a^b \theta_i(x)V(x)\theta_j(x)dx \\ &\approx \sum_{k=0}^{N_b-1} \frac{\omega_k}{W(x_k)} \theta_i(x_k)V(x_k)\theta_j(x_k) \\ &= V(x_i)\delta_{ij}, \end{aligned} \tag{A.20}$$

which is seen to be just the potential energy values at the quadrature points. This is especially important for the evaluation of two-electron integrals, where the memory requirement is reduced from $\mathcal{O}(N_b^4)$ to $\mathcal{O}(N_b^2)$. The kinetic energy matrix elements can be evaluated analytically. These properties, combined with the Gaussian quadrature accuracies, illustrates the attractiveness of the DVR.

An important relation [157] between the DVR and the Lagrange interpolation polynomials $L_j(x)$ is,

$$L_j(x) = \sqrt{\frac{\omega_j}{W(x)}} \theta_j(x), \tag{A.21}$$

where

$$L_j(x) \equiv \prod_{\substack{i=0 \\ (j \neq i)}}^{N_b-1} \frac{x - x_i}{x_j - x_i}. \tag{A.22}$$

This general relation can be proved by realizing that both sides of Eq. (A.21) are polynomials of order $N_b - 1$ with the same roots x_j and the same normalization.

In the case of Gauss-Lobatto DVR, one uses the Gauss-Lotatto quadrature rule in Eq. (A.8) with the end points included. The DVR functions are usually expressed in terms of the Lagrange interpolation polynomials,

$$\theta_j(x) = \frac{L_j(x)}{\sqrt{\omega_j}}. \tag{A.23}$$

A.3 Finite-element discrete variable representation

The FE-DVR approach combines a finite element method with a DVR basis. The total spatial region is divided into N_e elements, each element with its own set of DVR functions. Gauss-Lobatto DVR is used to connect the end points between two adjacent elements. The Lobatto shape functions, which are Lagrange interpolation polynomials on a given finite element e , is given by

$$L_j^e(x) = \prod_{\substack{i=0 \\ (i \neq j)}}^{N_b^e-1} \frac{x - x_i^e}{x_j^e - x_i^e} \times \begin{cases} 1, & \text{for } x \in [x_0^e, x_{N_b^e-1}^e], \\ 0, & \text{else,} \end{cases} \quad (\text{A.24})$$

with N_b^e the number of quadrature points x_i^e in element e . The basis functions are then defined as

$$\theta_j^e(x) = \begin{cases} \frac{L_j^e(x)}{\sqrt{\omega_j^e}}, & \text{for } j = 1, \dots, N_b^e - 2, \\ \frac{L_{N_b^e-1}^e(x) + L_0^{e+1}(x)}{\sqrt{\omega_{N_b^e-1}^e + \omega_0^{e+1}}}, & \text{for } j = N_b^e - 1, \end{cases} \quad (\text{A.25a})$$

$$(\text{A.25b})$$

where ω_j^e are the weights in element e . In Eq. (A.25b), the bridge functions between element boundaries are introduced to connect the FE boundaries, with the last quadrature point in element e overlapping with the first quadrature point in element $e + 1$, $x_{N_b^e-1}^e = x_0^{e+1}$. The FE-DVR functions satisfy the properties of the DVR, and the kinetic energy matrix attains a banded structure [85],

$$\begin{aligned} V_{ij}^{ef} &= \int \theta_i^e(x) V(x) \theta_j^f(x) dx \approx \delta_{ef} \delta_{ij} V(x_i^e), \\ T_{ij}^{ef} &= \frac{\delta_{ef} + \delta_e}{2} \int \frac{d}{dx} \theta_i^e(x) \frac{d}{dx} \theta_j^f(x) dx \approx \delta_{ef} \delta_{ij} V(x_i^e), \end{aligned} \quad (\text{A.26})$$

where the derivative of the DVR functions at the quadrature points are known analytically [85].

The FE-DVR, in contrast to standard DVR, allows for an good adaption of the basis to a physical problem, as one can specify the position of the elements and the number of the DVR functions in each element. For example in the problem of ionization, a FE element containing a large number of DVR functions can be used near the nucleus to accurately represent the bound part of the wave function, while FE's with less dense quadrature points far from the bound region can be used to describe the outgoing WPs.

APPENDIX B

FIELD-FREE CONTINUUM EIGENSTATES

In this Appendix, we describe the method used for obtaining the field-free continuum states of H_2^+ in the BO approximation. The time-independent Schrödinger equation reads

$$[T_e + T_N + V_{eN}(x, R) + V_N(R)]u(x, R) = Eu(x, R). \quad (\text{B.1})$$

The continuum states $u(x, R)$ of Eq. (B.1) depend on the electronic energies E_e , the nuclear energies E_N , and the parity P . We make in Eq. (B.1) the ansatz

$$u_{E_e E_N}^P(x, R) = \xi_{E_e}^P(x; R) \chi_{E_N}(R), \quad (\text{B.2})$$

and by neglecting the action of T_N on $\xi_{E_e}^P(x, R)$ (BO approximation), the electronic and nuclear degrees of freedom decouple, resulting in the equations

$$[T_e + V_{eN}(x, R)]\xi_{E_e}^P(x; R) = E_e \xi_{E_e}^P(x; R) \quad (\text{B.3})$$

$$[T_N + V_N(R)]\chi_{E_N}(R) = E_N \chi_{E_N}(R), \quad (\text{B.4})$$

with $E = E_e + E_N$. For a given E_e , Eq. (B.3) is solved for each internuclear distance R to obtain $\xi_{E_e}^P(x; R)$. These approximate continuum solutions were used successfully in Ref. [75].

We find the solutions to Eq. (B.3) numerically as follows. Starting near the origin, we impose the parity conditions $\xi_{E_e}^P(-\delta x; R) = (-1)^P \xi_{E_e}^P(\delta x; R)$, with δx being the integration step size. We then apply the Numerov algorithm to numerically integrate Eq. (B.3) outwards. The potential satisfies

$$V_{eN}(x, R) \rightarrow -\frac{2}{|x|}, \quad \text{for } |x| \gg R/2, \quad (\text{B.5})$$

which implies that the energy-normalized continuum solution has the asymptotic behaviour

$$\xi_{E_e}^P(x; R) \rightarrow \sqrt{\frac{\mu}{\pi p}} [F_{E_e}(x; R, \alpha_0) \cos(\delta P) + G_{E_e}(x; R, \alpha_0) \sin(\delta P)], \quad (\text{B.6})$$

where $p = \sqrt{2\mu E_e}$, δ_P is the phaseshift, $F_{E_e}(x; R, \alpha_0)$ and $G_{E_e}(x; R, \alpha_0)$ are the regular and irregular Coulomb functions, respectively. The latter functions were obtained using the GNU Scientific Library. By matching our numerical solutions to the asymptotic form in Eq. (B.6), we can obtain the energy delta-normalized states satisfying $\langle \xi_{E_e}^P(R) | \xi_{E_{e'}}^P(R) \rangle = \delta(E_e - E_{e'})$.

APPENDIX C

DRESSED BO CURVE OF A DIATOMIC MOLECULE FOR SMALL α_0

In this appendix we argue that for a general diatomic molecule subjected to linearly polarized laser pulses with small α_0 , the ground state BO potential behaves similarly to the case of H_2^+ , i.e. the surface energy, equilibrium internuclear distance, and vibrational time-scale increases with quiver amplitude.

Starting from the N -body electronic Hamiltonian, assuming infinite nuclear masses $M_1 = M_2 = \infty$, the dipole approximation, and velocity gauge,

$$H_e^{VG}(t) = T_e + V_{eN} + V_{ee} + V_N + V_I(t), \quad (\text{C.1})$$

with

$$\begin{aligned} T_e &= \sum_i \mathbf{p}_i^2/2, & V_{eN} &= \sum_i^N \left(-\frac{Z_A}{r_{iA}} - \frac{Z_B}{r_{iB}} \right), \\ V_{ee} &= \frac{1}{2} \sum_j^N \sum_{i \neq j}^N \frac{1}{|\mathbf{r}_i - \mathbf{r}_j|}, & V_N &= \frac{1}{R}, \\ V_I(t) &= \mathbf{A}(t) \cdot \sum_i^N \mathbf{p}_i, \end{aligned} \quad (\text{C.2})$$

where \mathbf{p}_i is the momentum operator of the i 'th electron, $\mathbf{A}(t) = F_0/\omega \cos(\omega t)\mathbf{e}$ the vector potential, $R = |\mathbf{R}|$ the internuclear distance, $r_{iA} = |\mathbf{r}_{iA}| = |\mathbf{r}_i + \mathbf{R}/2|$ and $r_{iB} = |\mathbf{r}_{iB}| = |\mathbf{r}_i - \mathbf{R}/2|$ the electronic distances to the nuclei, and Z_1 and Z_2 the nuclear charges. By applying the unitary transformation $U(t) = \exp\left(i\alpha(t) \cdot \sum_i^N \mathbf{p}_i\right)$, we obtain the KH electronic Hamiltonian:

$$H_e^{KH}(t) = T_e + V_{eN}^{KH}(t) + V_{ee} + V_N, \quad (\text{C.3})$$

with the electron-laser interaction contained in $V_{eN}^{KH}(t)$

$$V_{eN}^{KH}(t) = \sum_i^N \left(\frac{-Z_1}{|r_{iA} + \boldsymbol{\alpha}(t)|} + \frac{-Z_2}{|r_{iB} + \boldsymbol{\alpha}(t)|} \right), \quad (\text{C.4})$$

with $\boldsymbol{\alpha}(t) = \alpha_0 \sin(\omega t) \mathbf{e}$, and \mathbf{e} the linear polarization.

For small α_0 , the dressed potential $V_0(\alpha_0) = (\omega/2\pi) \int_0^{2\pi/\omega} V_{eN}^{KH}(t) dt$ only changes slightly compared to the field-free potential V_{eN} , and we can consider $V_0(\alpha_0) - V_{eN}$ a perturbation. The R -dependent electronic energy shift ΔE_{el} can then be evaluated as

$$\Delta E_{el}(R, \alpha_0) = \langle \Psi_0 | V_0(\alpha_0) - V_{eN} | \Psi_0 \rangle, \quad (\text{C.5})$$

with $|\Psi_0\rangle$ the unperturbed ground state. We proceed now as on p. 472 of Ref. [118] for hydrogen, but generalize to the multielectron, molecular case. Using the Fourier expansion of the Coulomb potential $1/|\mathbf{r}| = -(2\pi^2)^{-1} \int k^{-2} \exp(i\mathbf{k} \cdot \mathbf{r}) d\mathbf{k}$, and an expansion of $\exp(i\alpha_0 \cos(\omega t) \mathbf{k} \cdot \mathbf{e})$ to second order in α_0 , one arrives at

$$\begin{aligned} \Delta E_{el}(R, \alpha_0) &= \int d\mathbf{k} \sum_i^N \langle \Psi_0 | \frac{(\mathbf{k} \cdot \mathbf{e})^2}{k^2} e^{i\mathbf{k} \cdot \mathbf{r}_{iA}} \\ &\quad + \frac{(\mathbf{k} \cdot \mathbf{e})^2}{k^2} e^{i\mathbf{k} \cdot \mathbf{r}_{iB}} | \Psi_0 \rangle \\ &= \frac{\alpha_0^2}{4} \int d\mathbf{k} \sum_i^N \langle \Psi_0 | \frac{4\pi}{3} \delta(\mathbf{r}_{iA}) - \left[\frac{2P_2(\mathbf{e} \cdot \mathbf{r}_{iA})}{r_{iA}^3} \right] \\ &\quad + \frac{4\pi}{3} \delta(\mathbf{r}_{iB}) - \left[\frac{2P_2(\mathbf{e} \cdot \mathbf{r}_{iB})}{r_{iB}^3} \right] | \Psi_0 \rangle, \end{aligned} \quad (\text{C.6})$$

with $P_2(x) = (3x^2 - 1)/2$ the second-order Legendre polynomial. Approximating the ground state as a single determinant $|\Psi_0\rangle = |\phi_1 \dots \phi_N\rangle$, with ϕ_i the i 'th spin-orbital, and expanding the spatial orbitals in terms of Gaussian primitive basis functions centered at the two nuclei, as in conventional quantum chemistry, we can show that the second terms involving P_2 in Eq. (C.6) are small compared to the terms involving δ , and can thus be safely neglected. This will be presented at the end of the appendix. The remaining terms are proportional to the ground state electronic density $\rho(\mathbf{r}) = \sum_i^N \langle \Psi_0 | \delta(\mathbf{r}) | \Psi_0 \rangle$ at $\mathbf{r} = \pm \mathbf{R}/2$. We approximate the ground state density as $\rho(\mathbf{r}) = g_A(r_A) + g_B(r_B)$, with g_A and g_B two positive, monotonically decreasing functions defined on the interval $[0, \infty]$ with maximal values $g_A(0) = N_A$ and $g_B(0) = N_B$. The g_A and g_B can be quite general, as long as they satisfy the nuclear cusp conditions $0 = 2Z_A \rho(\mathbf{r}_A) + \partial \rho(\mathbf{r}) / \partial r_A |_{r_A=0} =$

$2Z_B\rho(\mathbf{r}_B) + \partial\rho(\mathbf{r})/\partial r_B|_{r_B=0}$, and the asymptotic behavior $\rho(\mathbf{r}) \sim \exp(-2\sqrt{2I_p}r)$ at large r , with I_p the ionization potential. Now the energy shift is given by

$$\Delta E_{el}(R, \alpha_0) = \frac{\alpha_0^2\pi}{3} [N_A + g_A(R) + N_B + g_B(R)], \quad (\text{C.7})$$

which is seen to show that: ***the ground state BO surface energy shifts upwards with quiver amplitude.*** Most ground state BO-curves $E_{el,1}(R, \alpha_0 = 0)$ are well approximated by the Morse potential

$$E_{el,1}(R, \alpha_0 = 0) \simeq D_e \left(e^{-2a(R-R_0)} - 2e^{-a(R-R_0)} \right), \quad (\text{C.8})$$

where R_0 is the field-free equilibrium internuclear distance, $D_e > 0$ the well depth, and $a > 0$ a molecular-specific parameter to fit the well-width. The ground state BO curve in the presence of a field with small α_0 is then

$$E_{el,1}(R, \alpha_0) \simeq E_{el,1}(R, 0) + \Delta E_{el}(R, \alpha_0). \quad (\text{C.9})$$

Setting $\partial E_{el,1}(R, \alpha_0)/\partial R = 0$, we obtain the new equilibrium internuclear distance $R_0(\alpha_0) = R_0 + \delta R$ in the presence of the field, with

$$\delta R = K_1/K_2, \quad (\text{C.10})$$

where

$$\begin{aligned} K_1 &= -(\alpha_0^2\pi/3) [g'_A(R_0) + g'_B(R_0)] \\ K_2 &= 2a^2D_e + (\alpha_0^2\pi/3) [g''_A(R_0) + g''_B(R_0)]. \end{aligned} \quad (\text{C.11})$$

As g_A and g_B are monotonically decreasing, $K_1 \geq 0$, and $K_2 > 0$ can always be satisfied for small enough α_0 . This shows that in the presence of a field with small α_0 , $\delta R \geq 0$, and ***the equilibrium internuclear distance is shifted towards larger values***, just as in the case of H_2^+ .

The vibrational period is approximated as $T_v(\alpha_0) = 2\pi/\omega_H(\alpha_0)$, with $\omega_H(\alpha_0) = \sqrt{k(\alpha_0)/M_N}$ the energy spacing between first two vibrational states in the harmonic approximation, $k(\alpha_0) = \partial^2 E_{el,1}(R, \alpha_0)/\partial R^2|_{R_0(\alpha_0)}$ the α_0 -dependent force constant, and $M_N = M_A M_B / (M_A + M_B)$ the reduced mass of the nuclei. Thus $k(0) - k(\alpha_0) > 0$ would imply a decrease in the vibrational period. From Eqs. (C.7)-(C.9) we obtain:

$$k(0) - k(\alpha_0) \simeq 6a^3 D_e \delta R - \left. \frac{\partial^2 \Delta E_{el,1}}{\partial R^2} \right|_{R_0 + \delta R}. \quad (\text{C.12})$$

As the second term on the right hand side of Eq. (C.12) is proportional to α_0^2 , it can always be made smaller than the first term for sufficiently small α_0 . This implies $k(0) - k(\alpha_0) > 0$, which proves that ***the vibrational time-scale increases with quiver amplitude.***

C.1 Neglect of the term involving P_2

Here we argue the neglect of the term involving P_2 in Eq. (C.6). We consider a multi-electron atom. In first quantization, a single particle operator (without action on spin) can be written

$$O_1 = \sum_{i=1}^N o(i), \quad (\text{C.13})$$

with N the number of electrons and $o(i)$ acting on the i 'th electron. The ground state determinant can be approximated as a closed-shell determinant,

$$\Psi = |\psi_{1\uparrow}\psi_{1\downarrow}\cdots\psi_{\frac{N}{2}\uparrow}\psi_{\frac{N}{2}\downarrow}\rangle, \quad (\text{C.14})$$

with $\psi_p(\mathbf{r}) = \psi_{n_p l_p m_p}(r, \theta, \phi)$ the p 'th spatial orbital, and \uparrow (\downarrow) denoting spin up (down). The expectation value of the operator O_1 can be written

$$\begin{aligned} M &\equiv \langle \Psi_0 | O_1 | \Psi_0 \rangle \\ &= 2 \sum_{p=1}^{N/2} M_p, \quad M_p = \langle \psi_p | o | \psi_p \rangle. \end{aligned} \quad (\text{C.15})$$

The spatial orbitals can be expanded in terms of the a primitive basis,

$$\begin{aligned} \psi_p(\mathbf{r}) &\equiv \psi_{n_p l_p m_p}(r, \theta, \phi) \\ &= \sum_i c_{n_p l_p}^i \phi_{l_p m_p}^i(r, \theta, \phi) \\ &= Y_{l_p m_p}(\theta, \phi) \sum_i c_{n_p l_p}^i R_{l_p}^i(r), \end{aligned} \quad (\text{C.16})$$

where R are the radial functions, Y the spherical harmonics, and the superscripts i are indices. Note that a given spatial orbital has no l and m mixing (no sum over l and m). The matrix elements can now be written

$$M_p = \sum_{ij} \left(c_{n_p l_p}^j \right)^* c_{n_p l_p}^i \langle \phi_{l_p m_p}^j | o | \phi_{l_p m_p}^i \rangle. \quad (\text{C.17})$$

In quantum chemistry structure calculations, the expansion coefficients c_{nl}^i are chosen real, and the primitive radial basis is usually taking as Slater- or Gaussian-type orbitals:

$$R_l^i(r) = \begin{cases} N_l^i r^l e^{-\zeta_l^i r}, & N_l^i = \frac{(2\zeta_l^i)^{l+\frac{3}{2}}}{\sqrt{(2l+2)!}} \quad (\text{STO}) \\ N_l^i r^l e^{-\alpha_l^i r^2}, & N_l^i = \frac{2^{l+\frac{7}{4}} (\alpha_l^i)^{\frac{l}{2}+\frac{3}{4}}}{\pi^{\frac{1}{4}} (2l+1)!!} \quad (\text{GTO}) \end{cases} \quad (\text{C.18})$$

In the present case,

$$\begin{aligned} o(\mathbf{r}) &= \frac{\alpha_0^2}{4} (o_1 + o_2), \\ o_1 &= \frac{4\pi}{3} \delta(\mathbf{r}), \quad o_2 = - \left[\frac{2P_2(\cos \theta)}{r^3} \right]', \end{aligned} \quad (\text{C.19})$$

we can calculate for the GTO,

$$\begin{aligned} \langle \phi_{lm}^j | o_1 | \phi_{lm}^i \rangle &= \frac{4\pi}{3} R_l^j(0) R_l^i(0) \\ &= \frac{4\pi}{3} \frac{2^{\frac{14}{4}} \left(\alpha_l^j \alpha_l^i \right)^{\frac{3}{4}}}{\sqrt{\pi}} \delta_{l0} \\ &= \frac{2^{\frac{11}{2}} \sqrt{\pi}}{3} \left(\alpha_0^j \alpha_0^i \right)^{\frac{3}{4}} \delta_{l0}, \end{aligned} \quad (\text{C.20})$$

which is seen to only give something when $l = 0$, which is the well-known result that *only s-orbitals contribute to the total density at a nucleus*. Now,

$$\langle \phi_{lm}^j | o_2 | \phi_{lm}^i \rangle = -2 \left\langle R_l^j \left| \frac{1}{r^3} \right| R_l^i \right\rangle \langle Y_{lm} | P_2(\cos \theta) | Y_{lm} \rangle \quad (\text{C.21})$$

The angular integral can be evaluated analytically using Gaunt's formula,

$$\langle Y_{lm} | P_2(\cos \theta) | Y_{lm} \rangle = \frac{l(l+1) - 3m^2}{(2l-1)(2l+3)}, \quad (\text{C.22})$$

and the radial integral can be performed using $\int_0^\infty x^n e^{-ax^2} dx = k!/(2a)^{k+1}$ for $a > 0$ and $n = 2k + 1$ odd,

$$\begin{aligned} \left\langle R_l^j \left| \frac{1}{r^3} \right| R_l^i \right\rangle &= \int_0^\infty N_l^j N_l^i r^{2l-1} e^{-(\alpha_l^j + \alpha_l^i)r^2} \\ &= \begin{cases} N_l^j N_l^i \frac{(l-1)!}{2(\alpha_l^j + \alpha_l^i)^l}, & \text{for } l > 0 \\ \text{divergent}, & \text{for } l = 0. \end{cases} \end{aligned} \quad (\text{C.23})$$

For $l = 0$, it is seen that the angular integral is 0, so we have

$$\begin{aligned} &\langle \phi_{lm}^j | o_2 | \phi_{lm}^i \rangle \\ &= -2N_l^j N_l^i \frac{(l-1)!}{2(\alpha_l^j + \alpha_l^i)^l} \frac{l(l+1) - 3m^2}{(2l-1)(2l+3)} (1 - \delta_{l0}) \\ &= -\frac{2^{2l+\frac{7}{2}} \left(\alpha_l^j \alpha_l^i \right)^{\frac{l}{2} + \frac{3}{4}}}{\sqrt{\pi} ((2l+1)!!)^2} \frac{(l-1)!}{(\alpha_l^j + \alpha_l^i)^l} \frac{l(l+1) - 3m^2}{(2l-1)(2l+3)} (1 - \delta_{l0}). \end{aligned} \quad (\text{C.24})$$

Table C.1: Table corresponding to the minimal Gaussian basis for C introduced in page 235 of [76], consisting of the atomic orbitals $1s$, $2s$, and $2p$.

(l, i)	α_l^i	c_{1l}^i	c_{2l}^i	c_{2l}^i
(0,1)	8.800	0.982	-0.266	
(0,2)	0.252	0.077	1.016	
(1,1)	0.385			1.000

The matrix element can be written as $M = \frac{\alpha_0^2}{4} (M_{o_1} + M_{o_2})$, with M_{o_1} stemming from the o_1 and M_{o_2} from o_2 ,

$$\begin{aligned}
M_{o_1} &= 2 \sum_n \langle \psi_{n00} | o_1 | \psi_{n00} \rangle \\
&= 2 \sum_n \sum_{ij} c_{n0}^j c_{n0}^i \langle \phi_{00}^j | o_1 | \phi_{00}^i \rangle \\
&= 2 \sum_{ij} \langle \phi_{00}^j | o_1 | \phi_{00}^i \rangle \sum_n c_{n0}^j c_{n0}^i,
\end{aligned} \tag{C.25}$$

and

$$\begin{aligned}
M_{o_2} &= 2 \sum_{n,l>1,m} \langle \psi_{nlm} | o_2 | \psi_{nlm} \rangle \\
&= 2 \sum_{n,l>0,m} \sum_{ij} c_{nl}^j c_{nl}^i \langle \phi_{lm}^j | o_2 | \phi_{lm}^i \rangle \\
&= 2 \sum_{l>0} \sum_{ij} \left(\sum_m \langle \phi_{lm}^j | o_2 | \phi_{lm}^i \rangle \right) \left(\sum_n c_{nl}^j c_{nl}^i \right),
\end{aligned} \tag{C.26}$$

For the minimal basis set (same number of GTO as number of orbitals) for Carbon given on page 235 of [76], [see Table C.1], we obtain from Eq. C.20: $\langle \phi_{00}^1 | o_1 | \phi_{00}^1 \rangle = 698.0$, $\langle \phi_{00}^2 | o_1 | \phi_{00}^2 \rangle = 3.382$, and $\langle \phi_{00}^1 | o_1 | \phi_{00}^2 \rangle = 48.59$.

$$\begin{aligned}
M_{o_1} &= 2 \left[(|c_{10}^1|^2 + |c_{20}^1|^2) \langle \phi_{00}^1 | o_1 | \phi_{00}^1 \rangle \right. \\
&\quad + (|c_{10}^2|^2 + |c_{20}^2|^2) \langle \phi_{00}^2 | o_1 | \phi_{00}^2 \rangle \\
&\quad \left. + 2 (c_{10}^1 c_{10}^2 + c_{20}^1 c_{20}^2) \langle \phi_{00}^1 | o_1 | \phi_{00}^2 \rangle \right] \\
&= 1414.
\end{aligned} \tag{C.27}$$

We have (assuming $m = 0$), $\langle \phi_{1m}^1 | o_2 | \phi_{1m}^1 \rangle = 0.4469$, so that

$$M_{o_2} = |c_{21}^1|^2 \langle \phi_{10}^1 | o_2 | \phi_{10}^1 \rangle = 0.4469. \tag{C.28}$$

As $M_{o_1} \gg M_{o_2}$ (more than 3 order of magnitude's difference), the operator o_2 can be safely neglected for C, at least in the present minimal basis. For more

complex basis sets, e.g. the Gaussian (9s5p) basis set for C given in Table 8.2 on page 291 of [76], the primitive Gaussian orbitals with the largest weights (orbitals ϕ_{lm}^i with the largest c_{nl}^i) for a given l , the exponents are similar in magnitude as the treated minimal basis set, and the operator o_2 can again safely be neglected.

As the HF ground state of C only has one p spatial orbital, only $(l, m) = (1, 0)$ needs to be considered, and there are no sums over l and m in Eq. (C.26). For more complex systems, more terms needs to be considered. We argue here that such contributions are still negligible compared to contributions from o_1 . First, the general rule is that the higher l , the more diffuse the orbitals (intuitive in a shell picture), and the smaller the α_l^i coefficients (for simple estimates, i can be chosen as the primitive GTO with the highest weight). This means that the α -dependent factor in Eq. (C.24) is a decreasing function with l , e.g. for the diagonal case with $i = j$:

$$\frac{\left(\alpha_l^j \alpha_l^i\right)^{\frac{l}{2} + \frac{3}{4}}}{\left(\alpha_l^j + \alpha_l^i\right)^l} \delta_{ij} = \frac{\left(\alpha_l^i\right)^{\frac{3}{2}}}{2^l} \delta_{ij}. \quad (\text{C.29})$$

The factor $[l(l+1) - 3m^2]/[(2l-1)(2l+3)]$ is positive and a decreasing function of l , and for $l \rightarrow \infty$ it goes to 1/4 for $m = 0$. The large- l behavior of Eq. (C.24) is then approximately

$$\begin{aligned} & \langle \phi_{lm}^j | o_2 | \phi_{lm}^i \rangle \\ & \sim \frac{(2\alpha_l^i)^{\frac{3}{2}}}{\sqrt{\pi}} \frac{2^l}{(2l+1)(2l) \cdots (l+1)l} \\ & \sim \frac{(2\alpha_l^i)^{\frac{3}{2}}}{\sqrt{\pi}} \frac{2^l}{\left[\left(\frac{3l+1}{2}\right)^{l+1}\right]}, \end{aligned} \quad (\text{C.30})$$

which is obviously rapidly decreasing with l . Also note that the expansion coefficients in s spatial orbitals are all positive, while some of the non- s spatial orbitals must have negative expansion coefficients to describe the radial nodes. This means that in Eq. (C.26) not all terms are positive, and cancelations will occur, further reducing the contribution from o_2 . With this we conclude that the most important non- s spatial orbitals contributing to M_{o_2} are the p -orbitals, and these were seen to be negligible compared to M_{o_1} .

APPENDIX D

COORDINATE TRANSFORMATIONS

In this appendix the definitions and coordinate transformations between three non-Cartesian coordinate systems are given.

D.1 Coordinate systems

Spherical coordinates

Spherical coordinates are defined by

$$r = \sqrt{x^2 + y^2 + z^2}, \quad r \in [0, \infty), \quad (\text{D.1a})$$

$$\theta = \arccos\left(\frac{z}{r}\right), \quad \theta \in [0, \pi], \quad (\text{D.1b})$$

$$\varphi = \arctan\left(\frac{y}{x}\right), \quad \varphi \in [0, 2\pi]. \quad (\text{D.1c})$$

Prolate spheroidal (confocal elliptic) coordinates

Consider two focal points placed at $\mathbf{R}_A = -\mathbf{R}/2$ and $\mathbf{R}_B = \mathbf{R}/2$, with $R = |\mathbf{R}|$ the distance between the focal points, and $r_A = |\mathbf{r} - \mathbf{R}_A|$ and $r_B = |\mathbf{r} - \mathbf{R}_B|$ the distances to the focal points. The prolate spheroidal coordinates are defined by [89]

$$\zeta = \frac{r_A + r_B}{R}, \quad \zeta \in [1, \infty), \quad (\text{D.2a})$$

$$\mu = \frac{r_A - r_B}{R}, \quad \mu \in [-1, 1], \quad (\text{D.2b})$$

$$\varphi = \arctan\left(\frac{y}{x}\right), \quad \varphi \in [0, 2\pi]. \quad (\text{D.2c})$$

Parabolic coordinates

Parabolic coordinates are defined by [131]

$$\xi = r + z, \quad \xi \in [0, \infty), \quad (\text{D.3a})$$

$$\eta = r - z, \quad \eta \in [0, \infty), \quad (\text{D.3b})$$

$$\varphi = \arctan\left(\frac{y}{x}\right), \quad \varphi \in [0, 2\pi]. \quad (\text{D.3c})$$

D.2 Coordinate transformations

Cartesian \leftrightarrow Prolate spheroidal

Transformation from Cartesian to prolate spheroidal coordinates is given by Eq. (D.2), with

$$r_A = \sqrt{x^2 + y^2 + z^2 + (R/2)^2 + zR} \quad (\text{D.4a})$$

$$r_B = \sqrt{x^2 + y^2 + z^2 + (R/2)^2 - zR}. \quad (\text{D.4b})$$

Transformation from prolate spheroidal to Cartesian coordinates:

$$x = \frac{R}{2} \sqrt{(\zeta^2 - 1)(1 - \mu^2)} \cos \varphi \quad (\text{D.5a})$$

$$y = \frac{R}{2} \sqrt{(\zeta^2 - 1)(1 - \mu^2)} \sin \varphi \quad (\text{D.5b})$$

$$z = \frac{R}{2} \zeta \mu. \quad (\text{D.5c})$$

Spherical \leftrightarrow Prolate spheroidal

Transformation from spherical to prolate spheroidal coordinates is given by Eq. (D.2), with

$$r_A = \sqrt{r^2 + (R/2)^2 + rR \cos \theta} \quad (\text{D.6a})$$

$$r_B = \sqrt{r^2 + (R/2)^2 - rR \cos \theta}. \quad (\text{D.6b})$$

Transformation from prolate spheroidal to spherical coordinates:

$$r = \frac{R}{2} \sqrt{\zeta^2 + \mu^2 - 1}, \quad (\text{D.7a})$$

$$\theta = \arccos\left(\frac{\zeta \mu}{\sqrt{\zeta^2 + \mu^2 - 1}}\right). \quad (\text{D.7b})$$

Parabolic \leftrightarrow Cartesian

Transformation from Cartesian to parabolic coordinates is given by Eq. (D.2), with

$$r = \sqrt{x^2 + y^2 + z^2} \quad (\text{D.8})$$

Transformation from parabolic to Cartesian coordinates:

$$x = \sqrt{\xi\eta} \cos \varphi \quad (\text{D.9a})$$

$$y = \sqrt{\xi\eta} \sin \varphi \quad (\text{D.9b})$$

$$z = \frac{\xi - \eta}{2}. \quad (\text{D.9c})$$

Parabolic \leftrightarrow Prolate spheroidal

Transformation from parabolic to prolate spheroidal coordinates is given by Eq. (D.2), with

$$r_A = \sqrt{\left(\frac{\xi + \eta}{2}\right)^2 + \left(\frac{R}{2}\right)^2 + R\left(\frac{\xi - \eta}{2}\right)} \quad (\text{D.10a})$$

$$r_B = \sqrt{\left(\frac{\xi + \eta}{2}\right)^2 + \left(\frac{R}{2}\right)^2 - R\left(\frac{\xi - \eta}{2}\right)}. \quad (\text{D.10b})$$

Transformation from prolate spheroidal to parabolic coordinates:

$$\xi = \frac{R}{2} \left(\sqrt{\zeta^2 + \mu^2 - 1} + \zeta\mu \right) \quad (\text{D.11a})$$

$$\eta = \frac{R}{2} \left(\sqrt{\zeta^2 + \mu^2 - 1} - \zeta\mu \right). \quad (\text{D.11b})$$

Parabolic \leftrightarrow Spherical

Transformation from spherical to parabolic coordinates:

$$\xi = r(1 + \cos \theta) \quad (\text{D.12a})$$

$$\eta = r(1 - \cos \theta). \quad (\text{D.12b})$$

$$(\text{D.12c})$$

Transformation from parabolic to spherical coordinates:

$$r = \frac{\xi + \eta}{2} \quad (\text{D.13a})$$

$$\theta = \arccos \left(\frac{\xi - \eta}{\xi + \eta} \right). \quad (\text{D.13b})$$

REFERENCES

- [1] L. Yue and L. B. Madsen, *Dissociation and dissociative ionization of H_2^+ using the time-dependent surface flux method*. Phys. Rev. A, **88**, 063420 (2013).
- [2] L. Yue and L. B. Madsen, *Dissociative ionization of H_2^+ using intense femtosecond xuv laser pulses*. Phys. Rev. A, **90**, 063408 (2014).
- [3] J. E. Bækhoj, L. Yue, and L. B. Madsen, *Nuclear-motion effects in attosecond transient-absorption spectroscopy of molecules*. Phys. Rev. A, **91**, 043408 (2015).
- [4] L. Yue and L. B. Madsen, *Characterization of molecular breakup by very intense femtosecond xuv laser pulses*. Phys. Rev. Lett., **115**, 033001 (2015).
- [5] L. Yue and L. B. Madsen, *Interference effects in strong-field dissociative ionization*. arXiv:1512.01428 (2015).
- [6] L. Yue, S. Bauch, and L. B. Madsen, *Electron correlation effects in orientation-dependent tunneling ionization of molecules* (in preparation).
- [7] A. H. Zewail, *Femtochemistry: atomic-scale dynamics of the chemical bond†*. J. Phys. Chem. A, **104**, 5660 (2000).
- [8] R. G. Meyerand and A. F. Haught, *Gas breakdown at optical frequencies*. Phys. Rev. Lett., **11**, 401 (1963).
- [9] P. Agostini *et al.*, *Free-free transitions following six-photon ionization of xenon atoms*. Phys. Rev. Lett., **42**, 1127 (1979).
- [10] A. McPherson *et al.*, *Studies of multiphoton production of vacuum-ultraviolet radiation in the rare gases*. J. Opt. Soc. Am. B, **4**, 595 (1987).
- [11] F. Lindner *et al.*, *Attosecond double-slit experiment*. Phys. Rev. Lett., **95**, 040401 (2005).

- [12] R. Gopal *et al.*, *Three-dimensional momentum imaging of electron wave packet interference in few-cycle laser pulses*. Phys. Rev. Lett., **103**, 053001 (2009).
- [13] T. Zuo and A. D. Bandrauk, *Charge-resonance-enhanced ionization of diatomic molecular ions by intense lasers*. Phys. Rev. A, **52**, R2511 (1995).
- [14] D. Pavičić *et al.*, *Intense-laser-field ionization of the hydrogen molecular ions H_2^+ and D_2^+ at critical internuclear distances*. Phys. Rev. Lett., **94**, 163002 (2005).
- [15] A. D. Bandrauk and M. L. Sink, *Photodissociation in intense laser fields: Predissociation analogy*. J. Chem. Phys., **74**, 1110 (1981).
- [16] P. H. Bucksbaum *et al.*, *Softening of the H_2^+ molecular bond in intense laser fields*. Phys. Rev. Lett., **64**, 1883 (1990).
- [17] A. Zavriyev *et al.*, *Light-induced vibrational structure in H_2^+ and D_2^+ in intense laser fields*. Phys. Rev. Lett., **70**, 1077 (1993).
- [18] G. Yao and S.-I. Chu, *Complex-scaling fourier-grid hamiltonian method. iii. oscillatory behavior of complex quasienergies and the stability of negative ions in very intense laser fields*. Phys. Rev. A, **45**, 6735 (1992).
- [19] B. D. Esry *et al.*, *Above threshold Coulomb explosion of molecules in intense laser pulses*. Phys. Rev. Lett., **97**, 013003 (2006).
- [20] L. B. Madsen *et al.*, *Structure factors for tunneling ionization rates of molecules*. Phys. Rev. A, **87**, 013406 (2013).
- [21] R. E. F. Silva *et al.*, *Correlated electron and nuclear dynamics in strong field photoionization of H_2^+* . Phys. Rev. Lett., **110**, 113001 (2013).
- [22] J. Wu *et al.*, *Electron-nuclear energy sharing in above-threshold multiphoton dissociative ionization of H_2* . Phys. Rev. Lett., **111**, 023002 (2013).
- [23] N. A. Papadogiannis *et al.*, *Observation of attosecond light localization in higher order harmonic generation*. Phys. Rev. Lett., **83**, 4289 (1999).
- [24] P. M. Paul *et al.*, *Observation of a train of attosecond pulses from high harmonic generation*. Science, **292**, 1689 (2001).
- [25] M. Hentschel *et al.*, *Attosecond metrology*. Nature (London), **414**, 509 (2001).

- [26] F. Krausz and M. Ivanov, *Attosecond physics*. Rev. Mod. Phys., **81**, 163 (2009).
- [27] R. Kienberger *et al.*, *Steering attosecond electron wave packets with light*. Science, **297**, 1144 (2002).
- [28] J. Itatani *et al.*, *Attosecond streak camera*. Phys. Rev. Lett., **88**, 173903 (2002).
- [29] M. Schultze *et al.*, *Delay in photoemission*. Science, **328**, 1658 (2010).
- [30] T. Remetter *et al.*, *Attosecond electron wave packet interferometry*. Nat. Phys., **2**, 323 (2006).
- [31] K. Klünder *et al.*, *Probing single-photon ionization on the attosecond time scale*. Phys. Rev. Lett., **106**, 143002 (2011).
- [32] E. Goulielmakis *et al.*, *Real-time observation of valence electron motion*. Nature (London), **466**, 739 (2010).
- [33] H. Wang *et al.*, *Attosecond time-resolved autoionization of argon*. Phys. Rev. Lett., **105**, 143002 (2010).
- [34] T. Popmintchev *et al.*, *Bright coherent ultrahigh harmonics in the keV x-ray regime from mid-infrared femtosecond lasers*. Science, **336**, 1287 (2012).
- [35] F. Silva *et al.*, *Spatiotemporal isolation of attosecond soft x-ray pulses in the water window*. Nat. Commun., **6**, 6611 (2015).
- [36] B. Wolter *et al.*, *Strong-field physics with mid-IR fields*. Phys. Rev. X, **5**, 021034 (2015).
- [37] J. Tate *et al.*, *Scaling of wave-packet dynamics in an intense midinfrared field*. Phys. Rev. Lett., **98**, 013901 (2007).
- [38] C. Hernández-García *et al.*, *Zeptosecond high harmonic keV x-ray waveforms driven by midinfrared laser pulses*. Phys. Rev. Lett., **111**, 033002 (2013).
- [39] Y. Huismans *et al.*, *Time-resolved holography with photoelectrons*. Science, **331**, 61 (2011).
- [40] X.-B. Bian *et al.*, *Subcycle interference dynamics of time-resolved photoelectron holography with midinfrared laser pulses*. Phys. Rev. A, **84**, 043420 (2011).

- [41] C. I. Blaga *et al.*, *Imaging ultrafast molecular dynamics with laser-induced electron diffraction*. *Nature*, **483**, 194 (2012).
- [42] V. Yanovsky *et al.*, *Ultra-high intensity- 300-TW laser at 0.1 Hz repetition rate*. *Opt. Express*, **16**, 2109 (2008).
- [43] J. Andreasson *et al.*, *Saturated ablation in metal hydrides and acceleration of protons and deuterons to keV energies with a soft-x-ray laser*. *Phys. Rev. E*, **83**, 016403 (2011).
- [44] R. Moshhammer *et al.*, *Few-photon multiple ionization of Ne and Ar by strong free-electron-laser pulses*. *Phys. Rev. Lett.*, **98**, 203001 (2007).
- [45] A. Rudenko *et al.*, *Recoil-ion momentum distributions for two-photon double ionization of He and Ne by 44 eV free-electron laser radiation*. *Phys. Rev. Lett.*, **101**, 073003 (2008).
- [46] A. A. Sorokin *et al.*, *Photoelectric effect at ultrahigh intensities*. *Phys. Rev. Lett.*, **99**, 213002 (2007).
- [47] K. Toyota *et al.*, *Siegert-state expansion in the kramers-henneberger frame: Interference substructure of above-threshold ionization peaks in the stabilization regime*. *Phys. Rev. A*, **76**, 043418 (2007).
- [48] P. V. Demekhin and L. S. Cederbaum, *Dynamic interference of photoelectrons produced by high-frequency laser pulses*. *Phys. Rev. Lett.*, **108**, 253001 (2012).
- [49] M. Gavrila, *Atomic stabilization in superintense laser fields*. *J. Phys. B*, **35**, R147 (2002).
- [50] A. M. Popov, O. V. Tikhonova, and E. A. Volkova, *Strong-field atomic stabilization: numerical simulation and analytical modelling*. *J. Phys. B*, **36**, R125 (2003).
- [51] J. Ullrich *et al.*, *Recoil-ion and electron momentum spectroscopy: reaction-microscopes*. *Rep. Prog. Phys.*, **66**, 1463 (2003).
- [52] L. V. Keldysh, *Ionization in the field of a strong electromagnetic wave*. *Zh. Eksp. Teor. Fiz.*, **47**, 1945 (1964). [*Sov. Phys. JETP* **20**, 1307 (1965)].
- [53] P. B. Corkum, *Plasma perspective on strong field multiphoton ionization*. *Phys. Rev. Lett.*, **71**, 1994 (1993).

- [54] F. H. M. Faisal, *Multiple absorption of laser photons by atoms*. J. Phys. B, **6**, L89 (1973).
- [55] H. R. Reiss, *Effect of an intense electromagnetic field on a weakly bound system*. Phys. Rev. A, **22**, 1786 (1980).
- [56] M. Lewenstein *et al.*, *Theory of high-harmonic generation by low-frequency laser fields*. Phys. Rev. A, **49**, 2117 (1994).
- [57] M. V. Ammosov, N. B. Delone, and V. P. Krainov, *Tunnel ionization of complex atoms and of atomic ions in an alternating electromagnetic field*. Zh. Eksp. Teor. Fiz., **91**, 2008 (1986). [Sov. Phys. JETP **64**, 1191 (1986)].
- [58] X. M. Tong, Z. X. Zhao, and C. D. Lin, *Theory of molecular tunneling ionization*. Phys. Rev. A, **66**, 033402 (2002).
- [59] O. I. Tolstikhin, T. Morishita, and L. B. Madsen, *Theory of tunneling ionization of molecules: Weak-field asymptotics including dipole effects*. Phys. Rev. A, **84**, 053423 (2011).
- [60] O. I. Tolstikhin, L. B. Madsen, and T. Morishita, *Weak-field asymptotic theory of tunneling ionization in many-electron atomic and molecular systems*. Phys. Rev. A, **89**, 013421 (2014).
- [61] S. X. Hu, *Optimizing the fedvr-tdcc code for exploring the quantum dynamics of two-electron systems in intense laser pulses*. Phys. Rev. E, **81**, 056705 (2010).
- [62] K. C. Kulander, *Time-dependent hartree-fock theory of multiphoton ionization: Helium*. Phys. Rev. A, **36**, 2726 (1987).
- [63] E. Runge and E. K. U. Gross, *Density-functional theory for time-dependent systems*. Phys. Rev. Lett., **52**, 997 (1984).
- [64] N. Rohringer, A. Gordon, and R. Santra, *Configuration-interaction-based time-dependent orbital approach for ab initio treatment of electronic dynamics in a strong optical laser field*. Phys. Rev. A, **74**, 043420 (2006).
- [65] J. Caillat *et al.*, *Correlated multielectron systems in strong laser fields: A multiconfiguration time-dependent hartree-fock approach*. Phys. Rev. A, **71**, 012712 (2005).
- [66] H. Miyagi and L. B. Madsen, *Time-dependent restricted-active-space self-consistent-field theory for laser-driven many-electron dynamics*. Phys. Rev. A, **87**, 062511 (2013).

- [67] D. Hochstuhl and M. Bonitz, *Time-dependent restricted-active-space configuration-interaction method for the photoionization of many-electron atoms*. Phys. Rev. A, **86**, 053424 (2012).
- [68] S. Bauch, L. K. Sørensen, and L. B. Madsen, *Time-dependent generalized-active-space configuration-interaction approach to photoionization dynamics of atoms and molecules*. Phys. Rev. A, **90**, 062508 (2014).
- [69] D. J. Haxton, K. V. Lawler, and C. W. McCurdy, *Multiconfiguration time-dependent hartree-fock treatment of electronic and nuclear dynamics in diatomic molecules*. Phys. Rev. A, **83**, 063416 (2011).
- [70] A. Hamido *et al.*, *Time scaling with efficient time-propagation techniques for atoms and molecules in pulsed radiation fields*. Phys. Rev. A, **84**, 013422 (2011).
- [71] S. Chelkowski, C. Foisy, and A. D. Bandrauk, *Electron-nuclear dynamics of multiphoton h_2^+ dissociative ionization in intense laser fields*. Phys. Rev. A, **57**, 1176 (1998).
- [72] B. Feuerstein and U. Thumm, *On the computation of momentum distributions within wavepacket propagation calculations*. J. Phys. B, **36**, 707 (2003).
- [73] L. Tao and A. Scrinzi, *Photo-electron momentum spectra from minimal volumes: the time-dependent surface flux method*. New J. Phys., **14**, 013021 (2012).
- [74] B. H. Bransden and C. J. Joachain, *Physics of atoms and molecules* (Pearson Education, Harlow, 2003).
- [75] C. B. Madsen *et al.*, *Multiphoton above threshold effects in strong-field fragmentation*. Phys. Rev. Lett., **109**, 163003 (2012).
- [76] T. Helgaker, P. Jørgensen, and J. Olsen, *Molecular Electronic-Structure Theory* (Wiley, Chichester, 2000).
- [77] J. G. Muga *et al.*, *Complex absorbing potentials*. Phys. Rep., **395**, 357 (2004).
- [78] E. S. Smyth, J. S. Parker, and K. Taylor, *Numerical integration of the time-dependent schrödinger equation for laser-driven helium*. Comput. Phys. Commun., **114**, 1 (1998).

- [79] C. W. McCurdy, M. Baertschy, and T. N. Rescigno, *Solving the three-body coulomb breakup problem using exterior complex scaling*. J. Phys. B, **37**, R137 (2004).
- [80] A. Scrinzi, *Infinite-range exterior complex scaling as a perfect absorber in time-dependent problems*. Phys. Rev. A, **81**, 053845 (2010).
- [81] M. D. Feit, J. A. Fleck Jr., and A. Steiger, *Solution of the schrödinger equation by a spectral method*. J. Comput. Phys., **47**, 412 (1982).
- [82] T. J. Park and J. C. Light, *Unitary quantum time evolution by iterative lanczos reduction*. J. Chem. Phys., **85** (1986).
- [83] H. R. Larsson, S. Bauch, and M. Bonitz, *Correlation effects in strong-field ionization of heteronuclear diatomic molecules*. arXiv:1507.04107 (2015).
- [84] J. C. Light, I. P. Hamilton, and J. V. Lill, *Generalized discrete variable approximation in quantum mechanics*. J. Chem. Phys., **82** (1985).
- [85] T. N. Rescigno and C. W. McCurdy, *Numerical grid methods for quantum-mechanical scattering problems*. Phys. Rev. A, **62**, 032706 (2000).
- [86] L. Tao, C. W. McCurdy, and T. N. Rescigno, *Grid-based methods for diatomic quantum scattering problems: A finite-element discrete-variable representation in prolate spheroidal coordinates*. Phys. Rev. A, **79**, 012719 (2009).
- [87] L. Tao, C. W. McCurdy, and T. N. Rescigno, *Grid-based methods for diatomic quantum scattering problems. iii. double photoionization of molecular hydrogen in prolate spheroidal coordinates*. Phys. Rev. A, **82**, 023423 (2010).
- [88] X. Guan, K. Bartschat, and B. I. Schneider, *Breakup of the aligned h₂ molecule by xuv laser pulses: A time-dependent treatment in prolate spheroidal coordinates*. Phys. Rev. A, **83**, 043403 (2011).
- [89] M. Abramowitz and I. A. Stegun, *Handbook of Mathematical Functions with Formulas, Graphs, and Mathematical Tables* (Dover, 1972), 9 edition.
- [90] L. B. Madsen *et al.*, *Extracting continuum information from $\psi(t)$ in time-dependent wave-packet calculations*. Phys. Rev. A, **76**, 063407 (2007).
- [91] P. V. Demekhin, D. Hochstuhl, and L. S. Cederbaum, *Photoionization of hydrogen atoms by coherent intense high-frequency short laser pulses: Direct propagation of electron wave packets on large spatial grids*. Phys. Rev. A, **88**, 023422 (2013).

- [92] J. Fernández and L. B. Madsen, *Alignment dependence in above-threshold ionization of h_2^+ : role of intermediate resonances*. J. Phys. B, **42**, 085602 (2009).
- [93] A. Keller, *Asymptotic analysis in time-dependent calculations with divergent coupling*. Phys. Rev. A, **52**, 1450 (1995).
- [94] A. Scrinzi, *t-surff: fully differential two-electron photo-emission spectra*. New J. Phys., **14**, 085008 (2012).
- [95] G. Jolicard and O. Atabek, *Above-threshold-dissociation dynamics of h_2^+ with short intense laser pulses*. Phys. Rev. A, **46**, 5845 (1992).
- [96] A. Giusti-Suzor *et al.*, *Dynamics of H_2^+ in intense laser fields*. J. Phys. B, **28**, 309 (1995).
- [97] J. H. Posthumus, *The dynamics of small molecules in intense laser fields*. Rep. Prog. Phys., **67**, 623 (2004).
- [98] L. Y. Peng, I. D. Williams, and J. F. McCann, *Dissociation of $h + 2$ from a short, intense, infrared laser pulse: proton emission spectra and pulse calibration*. J. Phys. B, **38**, 1727 (2005).
- [99] H. A. Leth, L. B. Madsen, and K. Mølmer, *Monte carlo wave packet theory of dissociative double ionization*. Phys. Rev. Lett., **103**, 183601 (2009).
- [100] U. Thumm, T. Niederhausen, and B. Feuerstein, *Time-series analysis of vibrational nuclear wave-packet dynamics in D_2^+* . Phys. Rev. A, **77**, 063401 (2008).
- [101] T. Niederhausen and U. Thumm, *Controlled vibrational quenching of nuclear wave packets in D_2^+* . Phys. Rev. A, **77**, 013407 (2008).
- [102] T. Niederhausen, U. Thumm, and F. Martin, *Laser-controlled vibrational heating and cooling of oriented $h + 2$ molecules*. J. Phys. B, **45**, 105602 (2012).
- [103] V. P. Majety, A. Zielinski, and A. Scrinzi, *Photoionization of few electron systems: a hybrid coupled channels approach*. New J. Phys., **17**, 063002 (2015).
- [104] K. Toyota *et al.*, *Interference substructure of above-threshold ionization peaks in the stabilization regime*. Phys. Rev. A, **78**, 033432 (2008).

- [105] P. V. Demekhin and L. S. Cederbaum, *ac stark effect in the electronic continuum and its impact on the photoionization of atoms by coherent intense short high-frequency laser pulses*. Phys. Rev. A, **88**, 043414 (2013).
- [106] C. Yu *et al.*, *Dynamic stark effect on xuv-laser-generated photoelectron spectra: Numerical experiment on atomic hydrogen*. Phys. Rev. A, **87**, 043405 (2013).
- [107] E. S. Sarachik and G. T. Schappert, *Classical theory of the scattering of intense laser radiation by free electrons*. Phys. Rev. D, **1**, 2738 (1970).
- [108] G. Mourou, T. Tajima, and S. Bulanov, *Optics in the relativistic regime*. Rev. Mod. Phys., **78**, 309 (2006).
- [109] R. W. Boyd, *Nonlinear Optics* (Academic, New York, 2008).
- [110] S. Chelkowski, P. B. Corkum, and A. D. Bandrauk, *Femtosecond coulomb explosion imaging of vibrational wave functions*. Phys. Rev. Lett., **82**, 3416 (1999).
- [111] S. Barmaki and H. Bachau, *Coulomb explosion of $h^2 +$ wave packet in ultrashort xuv laser fields*. J. Phys. B, **40**, 463 (2007).
- [112] L. Ph. H. Schmidt *et al.*, *Spatial imaging of the \mathbf{H}_2^+ vibrational wave function at the quantum limit*. Phys. Rev. Lett., **108**, 073202 (2012).
- [113] M. Førre *et al.*, *Nondipole ionization dynamics of atoms in superintense high-frequency attosecond pulses*. Phys. Rev. Lett., **97**, 043601 (2006).
- [114] T. Birkeland, R. Nepstad, and M. Førre, *Stabilization of helium in intense xuv laser fields*. Phys. Rev. Lett., **104**, 163002 (2010).
- [115] F. Morales *et al.*, *Imaging the kramers–henneberger atom*. Proc. Natl. Acad. Sci. U.S.A., **108**, 16906 (2011).
- [116] A. Ludwig *et al.*, *Breakdown of the dipole approximation in strong-field ionization*. Phys. Rev. Lett., **113**, 243001 (2014).
- [117] H. Reiss, *Limits on tunneling theories of strong-field ionization*. Phys. Rev. Lett., **101**, 043002 (2008).
- [118] M. Gavrilu, editor, *Atoms in Intense Laser Fields* (Academic, New York, 1992).

- [119] Q. Su, B. P. Irving, and J. H. Eberly, *Ionization modulation in dynamic stabilization*. Laser Phys., **7**, 568 (1997).
- [120] M. Dörr and R. M. Potvliege, *Adiabatic stabilization in photodetachment by ultrashort pulses*. J. Phys. B, **33**, L233 (2000).
- [121] W. C. Henneberger, *Perturbation method for atoms in intense light beams*. Phys. Rev. Lett., **21**, 838 (1968).
- [122] M. Gavrilu and J. Shertzer, *Two-electron atoms in superintense radiation fields: Dichotomy and stabilization*. Phys. Rev. A, **53**, 3431 (1996).
- [123] N. A. Nguyen and T.-T. Nguyen-Dang, *Molecular dichotomy within an intense high-frequency laser field*. J. Chem. Phys., **112**, 1229 (2000).
- [124] C. Pérez Del Valle, R. Lefebvre, and O. Atabek, *Dressed potential energy surface of the hydrogen molecule in high-frequency floquet theory*. Int. J. Quantum Chem., **70**, 199 (1998).
- [125] C. P. del Valle, R. Lefebvre, and O. Atabek, *Dressed states of the high-frequency floquet theory for atoms and molecules with standard computational quantum chemistry programs*. J. Phys. B, **30**, 5157 (1997).
- [126] J. Shertzer, A. Chandler, and M. Gavrilu, H_2^+ *in superintense laser fields: Alignment and spectral restructuring*. Phys. Rev. Lett., **73**, 2039 (1994).
- [127] D. G. Arbó, E. Persson, and J. Burgdörfer, *Time double-slit interferences in strong-field tunneling ionization*. Phys. Rev. A, **74**, 063407 (2006).
- [128] M. Richter *et al.*, *Streaking temporal double-slit interference by an orthogonal two-color laser field*. Phys. Rev. Lett., **114**, 143001 (2015).
- [129] G. B. Arfken and H. J. Weber, *Mathematical Methods for Physicists (International Edition)* (Academic Press, Burlington, MA, 2005), 6 edition.
- [130] D. G. Arbó *et al.*, *Intracycle and intercycle interferences in above-threshold ionization: The time grating*. Phys. Rev. A, **81**, 021403 (2010).
- [131] L. D. Landau and E. M. Lifshitz, *Quantum Mechanics (Non-Relativistic Theory)* (Pergamon, Oxford, 1977).
- [132] V. Mosert and D. Bauer, *Dissociative ionization of H_2^+ : Few-cycle effect in the joint electron-ion energy spectrum*. Phys. Rev. A, **92**, 043414 (2015).

- [133] J. R. Oppenheimer, *Three notes on the quantum theory of aperiodic effects*. Phys. Rev., **31**, 66 (1928).
- [134] Y. N. Demkov and G. G. Drukarev, . Zh. Eksp. Teor. Fiz., **47**, 918 (1964). [Sov. Phys. JETP **20**, 614 (1964)].
- [135] S. Y. Slavyanov, . Probl. Mat. Fiz., **4**, 125 (1970). English translation in *Topics in Mathematical Physics*, Vol. 4 (Consultants Bureau, New York, 1971).
- [136] T. Yamabe, A. Tachibana, and H. J. Silverstone, *Theory of the ionization of the hydrogen atom by an external electrostatic field*. Phys. Rev. A, **16**, 877 (1977).
- [137] Y. N. Demkov and G. G. Drukarev, *The breaking up of atomic particles by an electric field and by electron collisions*. Zh. Eksp. Teor. Fiz., **49**, 841 (1965). [Sov. Phys. JETP **22**, 585 (1966)].
- [138] A. M. Perelomov, V. S. Popov, and M. V. Terent'ev, *Ionization of atoms in an alternating electric field*. Zh. Eksp. Teor. Fiz., **50**, 1393 (1966). [Sov. Phys. JETP **23**, 924 (1966)].
- [139] H. Akagi *et al.*, *Laser tunnel ionization from multiple orbitals in hcl*. Science, **325**, 1364 (2009).
- [140] L. Holmegaard *et al.*, *Photoelectron angular distributions from strong-field ionization of oriented molecules*. Nat. Phys., **6**, 428 (2010).
- [141] L. B. Madsen, O. I. Tolstikhin, and T. Morishita, *Application of the weak-field asymptotic theory to the analysis of tunneling ionization of linear molecules*. Phys. Rev. A, **85**, 053404 (2012).
- [142] R. Saito *et al.*, *Structure factors for tunneling ionization rates of diatomic molecules*. Atomic Data and Nuclear Data Tables, **103–104**, 4 (2015).
- [143] C. Wang *et al.*, *Extraction of electron–ion differential scattering cross sections for $c 2 h 4$ by laser-induced rescattering photoelectron spectroscopy*. J. Phys. B, **45**, 131001 (2012).
- [144] L. B. Madsen *et al.*, *Application of the weak-field asymptotic theory to tunneling ionization of h_2O* . Phys. Rev. A, **89**, 033412 (2014).
- [145] P. M. Kraus *et al.*, *Observation of laser-induced electronic structure in oriented polyatomic molecules*. Nat. Commun., **6**, 7039 (2015).

- [146] P. M. Kraus *et al.*, *Measurement and laser control of attosecond charge migration in ionized iodoacetylene*. *Science*, **350**, 790 (2015).
- [147] T. Brabec *et al.*, *Theory of tunnel ionization in complex systems*. *Phys. Rev. Lett.*, **95**, 073001 (2005).
- [148] O. I. Tolstikhin, H. J. Wörner, and T. Morishita, *Effect of nuclear motion on tunneling ionization rates of molecules*. *Phys. Rev. A*, **87**, 041401 (2013).
- [149] O. I. Tolstikhin and L. B. Madsen, *Retardation effects and the born-oppenheimer approximation: Theory of tunneling ionization of molecules revisited*. *Phys. Rev. Lett.*, **111**, 153003 (2013).
- [150] J. Svensmark, O. I. Tolstikhin, and L. B. Madsen, *Coulomb and dipole effects in tunneling ionization of molecules including nuclear motion*. *Phys. Rev. A*, **91**, 013408 (2015).
- [151] V. H. Trinh *et al.*, *First-order correction terms in the weak-field asymptotic theory of tunneling ionization*. *Phys. Rev. A*, **87**, 043426 (2013).
- [152] P. A. Batishchev, O. I. Tolstikhin, and T. Morishita, *Atomic siegert states in an electric field: Transverse momentum distribution of the ionized electrons*. *Phys. Rev. A*, **82**, 023416 (2010).
- [153] J. Kobus, L. Laaksonen, and D. Sundholm, *A numerical Hartree-Fock program for diatomic molecules*. *Comput. Phys. Commun.*, **98**, 346 (1996). <http://www.leiflaaksonen.eu/num2d.html>.
- [154] I. Y. Tolstikhina, T. Morishita, and O. I. Tolstikhin, *Application of the many-electron weak-field asymptotic theory of tunneling ionization to atoms*. *Phys. Rev. A*, **90**, 053413 (2014).
- [155] I. Kawata, H. Kono, and Y. Fujimura, *Adiabatic and diabatic responses of $h2+$ to an intense femtosecond laser pulse: Dynamics of the electronic and nuclear wave packet*. *J. Chem. Phys.*, **110** (1999).
- [156] D. Dundas *et al.*, *Ionization dynamics of laser-driven $h2+$* . *J. Phys. B*, **33**, 3261 (2000).
- [157] D. J. Tannor, *Introduction to Quantum Mechanics: A Time-Dependent Perspective* (University Science Books, Sausalito, CA, 2007).